Appendix 4
Pielikums 4

National Research Programme

Cyber-physical systems, ontologies and biophotonics for safe&smart city and society

(SOPHIS)

Project No.4

Development of technologies for secure and reliable smart city"

(GudPils)

FINAL REPORT

2017

Contents

Glossary and abbreviations **v**

4.1Introduction **1**

4.2EDI BIGDATA group: Development of methods and software for video and other sensor data processing to target urban security problems **2**

4.2.1 Development of object descriptor for face identification in images 3
- 4.2.1.1 Face image descriptor 3
- 4.2.1.2 Artificial neural network architecture and training 4
- 4.2.1.3 Experimental results 6
- 4.2.1.4 Conclusions 6

4.2.2 Recurrent neural network based virtual detection line 7
- 4.2.2.1 Related work 7
- 4.2.2.2 Method for detection of moving objects 8
- 4.2.2.3 Tests 13
- 4.2.2.4 Approbation: Car counting system 16
- 4.2.2.5 Conclusions 17

4.2.3 Summary 17

4.2.4 Conclusions 19

4.3EDI REMSENS group: Investigation of possibilities to use remote sensing data for solving city monitoring tasks **20**

4.3.1 Remote sensing data processing methods for urban land use mapping 21
- 4.3.1.1 Classification of land use categories from multisensor data 21
- 4.3.1.2 Selection of informative bands for classification of hyperspectral images 23
- 4.3.1.3 Classification of multispectral remote sensing images using fuzzy logic 24

4.3.2 Development of tools for vegetation mapping and its change detection 27

4.3.3 Development of land surface elevation model from LiDAR data and software for simulation of flooding 31

4.3.4 Summary 35

4.4 EDI RADAR group: Development of the ultra-wideband (UWB) radar technology and UWB-based systems for security monitoring 38
4.4.1 Introduction of ultra-wideband technology 38
4.4.1.1 Theoretical UWB radar object resolution 39
4.4.2 UWB security applications 40
4.4.2.1 Ice thickness measurement 40
4.4.2.2 Building material structure inspection 42
4.4.2.3 Remote life-sign detection 44
4.4.2.4 Object detection, counting and tracking 45
4.4.3 Short range UWB radar development 55
4.4.3.1 Miniature UWB radar sensor development 55
4.4.3.2 Universal UWB radar prototype design 57
4.4.4 Approbation: advanced traffic density measurements using UWB radar 59
4.4.5 Conclusions 60

4.5 RTU TI group: Development of fiber optics transmission technologies 61
4.5.1 General description of the research area 61
4.5.2 Analysis of different optical access network topologies 63
4.5.2.1 Development of spectrum sliced transceiver 64
4.5.3 Investigation on the minimum channel spacing in the WDM-PON system taking into account channel bitrate, laser parameters and overall spectral and energy efficiency 70
4.5.4 Studies of optical fiber nonlinearity coefficient 74
4.5.5 Conclusions 74
4.5.6 Summary 76

4.6 RTU WRL group: Development of the bacteriological quality monitoring system for city water supply system 79
4.6.1 Introduction 80
4.6.2 Literature studies and background 81
4.6.3 Testing of different drinking water quality monitoring methods in batch scale and pilot-scale experiments 81
4.6.3.1 Testing of different drinking water quality monitoring methods in batch scale experiments 81
4.6.3.2 Testing of different drinking water quality monitoring methods in pilot-scale experiments 82
4.6.4 Design and installation of the lab-scale experimental drinking water supply system 84
4.6.5 Development of a hydraulic model for lab-scale DWDS 85
4.6.5.1 Results for a short term scenario validation 86
4.6.5.2 Results for a long term scenario validation 87
4.6.6 Development of a drinking water quality modeling tool 88

4.6.7 Long-term monitoring of drinking water quality in lab-scale and real scale drinking water supply systems to establish the baseline quality 88
4.6.7.1 Long-term monitoring of drinking water quality in a lab-scale and real-scale water supply systems with biological method 88
4.6.7.2 Long-term monitoring of physiochemical drinking water quality parameters in a pilot-scale and real scale drinking water supply systems 93
4.6.8 Development of algorithm for drinking water contamination event detection and alarm triggering 95
4.6.9 Experiments within pilot scale drinking water supply system by simulation of contamination events to evaluate the efficiency of drinking water on-line monitoring system 96
4.6.9.1 Simulation experiments of contamination events (primary) 97
4.6.9.2 Simulation of contamination events and classification of the most possible drinking water supply system contaminants 98
4.6.10 Verification of event detection and alarm triggering algorithm by the measurements in pilot scale drinking water supply system . . 101
4.6.11 Implementation of event detection and alarm triggering algorithm in on-line drinking water quality monitoring system 102
4.6.12 Approbation of drinking water bacteriological quality monitoring system in real scale network 104
4.6.13 Conclusions and future work 105

4.7 Summary of project results **107**
4.7.1 Scientific performance indicators 107
4.7.1.1 Original scientific articles (SNIP≥ 1) 107
4.7.1.2 Original scientific articles (SCOPUS/Web of Science/IEEExplore) 107
4.7.1.3 Reviewed scientific monographs 111
4.7.1.4 Other scientific articles 111
4.7.1.5 Doctoral thesis 111
4.7.1.6 Master thesis 112
4.7.1.7 Bachelor thesis 114
4.7.1.8 Exploitation of results in study courses 114
4.7.2 Performance indicators of the promotion of the project 114
4.7.2.1 Presentations in conferences 114
4.7.2.2 Posters in conferences 117
4.7.2.3 Organized public seminars 117
4.7.2.4 Participation in exhibitions 118
4.7.2.5 Popular-science publications 118
4.7.2.6 Long-term technological prognosis 119
4.7.3 Economic performance indicators 119
4.7.3.1 Income from new projects 119

4.7.3.2 Patents 119
4.7.3.3 Approbated technologies 120
4.7.3.4 Approbated software 120

Bibliography **121**

Glossary and abbreviations

ANN - artificial neural network;

API - application program interface;

ASDM - Asynchronous Sigma-Delta modulator;

ATP - adenosine triphosphate;

AWG - arbitrary waveform signal generator;

B2B - band to band;

BER - bit error rate;

CNN - convolution neural network;

CUDA - NVIDIA parallel computing platform on GPU;

DFB - distributed feedback laser;

DL - deep learning;

DMSO - dimethyl sulfoxide;

DSF - dispersion shifted fiber;

DSO - digital storage oscilloscope;

DSP - digital signal processing;

DWDS - drinking water distribution system;

DWSS drinking water supply system;

DW drinking water;

EC electrical conductivity;

EDI - Institute of Electronics and Computer Science, Riga, Latvia;

EDS - event detection system;

EDTA - ethylenediaminetetraacetic acid;

EPA - United States Environmental Protection Agency;

ERDF - European Regional Development Fund;

ETSI - European Telecommunications Standards Institute;

EWS Early warning system;

FCM - flow cytometry;

FFT - fast Fourier transform;

FMCW - frequency-modulated continuous-wave;

FP False positive;

FPR False positive rate;

GbE - Gigabit Ethernet;

GPR - ground probing radar;

GPS - Global Positioning System;

GPU - graphics processing unit;

GudPils - Development of technologies for secure and reliable smart city (Project No. 4);

GUI - graphical user interface;

HPC - High Performance Computing;

HtPC heterotrophic plate count;

IC inorganic carbon;

ICC - intact cell count;

IECS - Institute of Electronics and Computer Science, Riga, Latvia;

IFFT - inverse fast Fourier transform;

KL - Karhunen-Loeve;

OS - computer Operating System;

LabVIEW - Laboratory Virtual Instrument Engineering Workbench (National Instruments software environment);

LCD - Liquid Crystal Display;

LSTM - Long Short-Term Memory network;

NDVI - Normalized Difference Vegetation Index;

NGN - Next Generation Networks

NPOC non-purgeable organic carbon;

NRZ - non-return-to-zero;

NVIDIA - NVIDIA Corporation;

NZDSF - non-zero dispersion-shifted fiber;

ODN - Optical Distribution Network;

OF - optical fiber;

OLT - optical line terminal;

ONT - Optical Network Terminal;

ORP oxidation-reduction potential;

OS - computer Operating System;

PC - personal computer;

PCB - printed circuit board;

RGB - red-green-blue;

PI propidium iodide;

RMS - root mean square;

RNN - recurrent neural network;

RTU - Riga Technical University;

RTU TI - Riga Technical University Telecommunications Institute;

RTU WRL - Riga Technical University Faculty of Civil Engineering Water Research Laboratory;

RTU BF - Riga Technical University Faculty of Civil Engineering;

SG SYBR Green I;

SGPI SYBR Green I propidium iodide stain;

SNR - Signal-to-noise ratio;

SMF - single-mode optical fiber;

SOPHIS - programme ”Cyber-physical systems, ontologies, and bio-photonics for safe&smart city and society”;

SRD - Short Range Devices;

SVM - Support Vector Machine;

TCC - total cell count;

TDM-PON - time division multiplexed passive optical network;

TI image - thermal infrared image;

TC total carbon;

TOC - total organic carbon;

TPR True positive rate;

TP True positive;

TWI - Through-Wall Imaging;

USB - Universal Serial Bus;

UWB - Ultra-wideband;

VPP - State Research Programme;

VOA - variable optic attenuator;

WDM-PON - wavelength division multiplexed passive optical network;

WTP drinking water treatment plant;

Chapter 4.1

Introduction

This appendix contains the final scientific report of the project GudPils of the SOPHIS program. The project was dedicated to research and development of information and communication technologies that can be used to solve city management problems in an advanced way. Research was focused on tasks defined in the project proposal, matching the goals of the state research program.

The report consists of chapters prepared by individual scientific groups formed within the project. These are as follows:

1. EDI BIGDATA group developed methods and software for video and other sensor data processing to target urban security problems. The results of this group is presented in chapter 4.2;
2. EDI REMSENS group developed remote sensing data processing techniques for monitoring of the urban environment. The results of this group is presented in chapter 4.3;
3. EDI RADAR group developed ultra-wideband radar technology-based solutions for urban security systems needs. The results of this group is presented in chapter 4.4;
4. RTU TI group of researchers developed optical networking solutions for smart cities data transmission. The results of this group is presented in chapter 4.5;
5. RTU WRL team (previously referred as RTU BF) of researchers developed solutions for controlling the urban water supply systems. The results of this group is presented in chapter 4.6.

Chapter 4.7 contains summarized results of the project.

Chapter 4.2

EDI BIGDATA group: Development of methods and software for video and other sensor data processing to target urban security problems

Research goal: Analysis of video and another signal content gathered from many signal sources distributed over smart cities for safety purposes.

This Chapter summarizes and describes final results of BIGDATA group obtained in this project. EDI BIGDATA group develops methods and software for video and other sensor data processing to target urban security problems. Project started in 2014 and after the analysis of remarkable results obtained by other scientists (Yaniv Taigman, Ming Yang, MarcAurelio Ranzato, Lior Wolf, DeepFace: Closing the Gap to Human-Level Performance in Face Verification; the developed system achieves remarkable 97.35 % accuracy on Faces in the Wild data set) it was clear that a right approach is to use artificial neural networks (deep learning) for building data analysis solutions in smart cities. It led to the following activities in project periods 1 – 3:

1. Investigation and understanding of the current state in deep learning;
2. Preparation of scientific environment and High-Performance Computing (HPC) servers for signal content analysis and experimentation using deep learning;
3. Exploration of deep learning tools, training examples on HPC servers and potential applications for increasing safety and security in smart cities.

List of tasks for the project period 4:

1. Develop a method for detection of moving objects using a recurrent neural network (RNN) processing data from the virtual detection line;

2. Develop a method for face identification in images;

3. Test the counting system of moving objects in real conditions.

The project has resulted in 2 main solutions related to smart city safety and security. Now it is clear the the main limitation for solution development using deep learning is availability of labeled data. This labeled data problem might be targeted in further BIGDATA team projects. The main solutions developed in this project are the following:

1. Development of face identification system in images;

2. Development of a video-based counter of moving objects.

Besides the main activities related to deep learning, efforts in research for data acquisition and sensor systems were spent for solving a large-scale signal gathering and acquisition problem. It was done in collaboration with other EDI scientists. The list of scientific publications and other collaboration results can be found further in the list of BIGDATA team results. This Section is mainly focused on describing the signal content analysis using deep learning, which is directly making impact on the security and safety problems in smart cities.

Further in this Chapter we will describe research performed by the BIGDATA team and trained neural networks useful for smart city applications: 1) Development of object descriptor for face identification in images, 2) Recurrent neural network operating with a virtual detection line, and 3) Summary of all project results obtained by the BIGDATA team.

4.2.1 Development of object descriptor for face identification in images

The progress achieved in development of a technique of image descriptors is shown in the paper: K. Sudars, Face Recognition Face2vec Based on Deep Learning: Small Database Case. This paper is published in the journal Automatic Control and Computer Science (indexed in SCOPUS) in the beginning of 2017. On the basis of this publication, the main developments and contributions are described further in this Section.

4.2.1.1 Face image descriptor

Construction of a facial image descriptor based on deep learning is the best approach for the given task. Calculation of vectors embedding visual face features in image automatically extracted by artificial neural network (ANN) is considered. In such a way, the comparison of two facial images can be done by calculation of vector distances or correlation coefficients. Related work in some variations can be found in these papers representing the top achievements in facial image recognition [1, 2, 3]. The considered approach is universal and can be applied to many tasks. Here it is done on facial images for person identification problem. The approach used to obtain feature vectors for description of facial images (or any other object in images) consists of two stages: (1) in the first stage, the ANN is trained for classification of persons using training data set, (2) in the second stage, the ANN gets cropped by removing the linear classification layer (in other words, the last layer) and the output of this modified ANN is used as a feature vector or so called facial image descriptor. The whole process is illustrated in Figure 4.2.1.

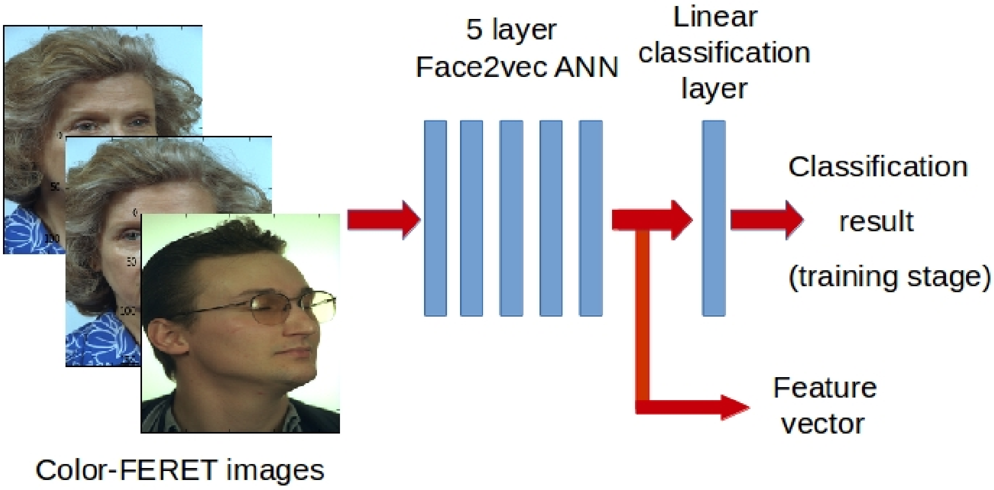

Figure 4.2.1: Feature vector calculation with ANN.

In the project, ANN was trained and tested using the Color-FERET facial image data set [4]. These tasks were accomplished employing High Performance Computing (HPC) server with Nvidia K40 GPU cards running Ubuntu 14.04 operating system and TensorFlow machine learning software library [5].

4.2.1.2 Artificial neural network architecture and training

The Color-FERET facial image database consists of approximately 10 000 images (Approximately 1000 different people with approximately 10 images per person taken from different views). For the study purposes, the classes (representing particular persons in the set) of the Color-FERET database were divided into training set and validation set in proportion 90:10. Images of the training set were used only for construction of the descriptor and the validation set of images was used only for validation of the constructed descriptor (for each member of the validation set, the most similar image from the rest of the validation set was found using the correlation coefficient; it is most likely that the closest image in the validation set belongs to the same class, namely, the same person). Correlation coefficient shows similarity between objects and their features. It allows to find class members or specific objects in many images. Before training of the ANN, the images are converted to 224x224 pixel resolution. The considered artificial neural network architecture is shown in Figure 4.2.2. The ANN architecture used is close to AlexNet [6]. It consists of five convolutional neural network (CNN) layers with a ReLU (Rectified Linear Unit) standing at the end of each CNN layer. Three Maximum Pooling layers are put between CNN layers, picking out maximum values from the data. These layers allow to reduce data dimensions and to decrease required computational power.

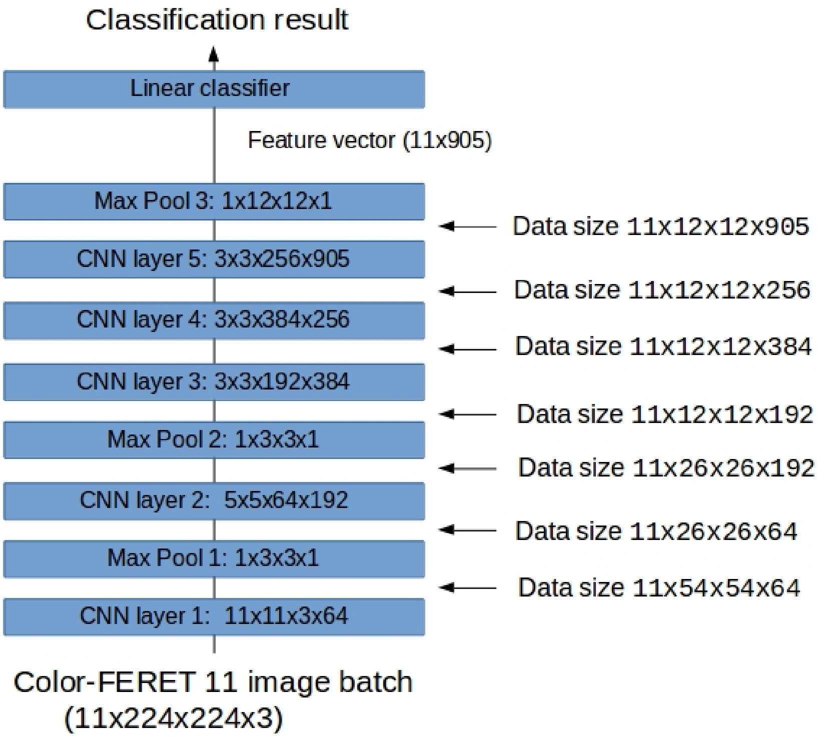

Figure 4.2.2: Artificial neural network for calculation of facial descriptor.

During the training, ANN coefficients are found using the Stochastic Gradient Descent (SGD) optimization method that is implemented in the TensorFlow machine learning library. The Mean Square Error is used as a cost minimization function, forcing ANN model to converge and making it able to classify images from the training set.

After training, the representative feature vectors of unknown facial images can be obtained from the trained ANN model. Then these vectors are normalized and compared to recognize the same person in images by calculating and comparing correlation coefficients or Euclidean distances.

4.2.1.3 Experimental results

Two ANN models were trained and validated using the Color-FERET data set: ANN-1 and ANN-2. Convergence of the ANN model during training set is not always easily achieved. Related problems are described in the paper: K. Sudars, Face Recognition Face2vec Based on Deep Learning: Small Database Case. After approximately 6 epochs, the ANN-1 model reached 98 % accuracy on the training set and did not converge to maximum 100 % value (learning rate LR was 0.01). It could be acceptable if a training set contains mistakenly labeled data. However, in the case of the Color-FERET database, the 100 % accuracy should be reached. In order to force an artificial neural network to reach 100 % accuracy, a fine-tuning with much smaller learning rates (LR is 0.0001) was performed, thus obtaining the ANN-2 model. As a drawback, it increases the training time. After the training stage, the accuracy was estimated using the Color-FERET validation set. Percentages were calculated by counting successfully recognized images and dividing the obtained value by the number of all images in the validation set. The experimental results are shown in Table 4.2.1. In addition, the ANN models were tested with frontal face images taken from Color-FERET validation database (named Color-FERET-fa-fb). As it can be seen in Table 4.2.1, better accuracy is obtained in this case.

Table 4.2.1: Experimental results.

	ANN-1 model, Color-FERET database	ANN-2 model, Color-FERET database	ANN-2 model, Color-FERET-fa-fb database
Accuracy of class (person name) recognition at the first attempt, [accuracy, %]	52.27	87.54	93.94
Accuracy of class recognition within 2 attempts, [%]	68.51	94.87	95.96
Accuracy of class recognition within 3 attempts, [%]	77.02	96.97	**97.98**

4.2.1.4 Conclusions

For object visual recognition in images, the universal approach based on deep learning is used and tested, which is applicable in recognition of all kind of objects and situations. It is tested on facial images. As it is shown, the obtained results lead to the following conclusions: (1) ANN fine-tuning from 98 % to 100 % accuracy on training set using extremely low learning rates (lower than 0.0001) can significantly improve the accuracy of the face recognition system (however, it increases the training time); (2) the proposed ANN architecture under described training conditions is capable to represent necessary features for face recognition. During experiments the best trained ANN model achieves 94 % accuracy on Color-FERET frontal face image database. Further development: it is expected that better results could be obtained if ANN would be trained on much more larger data set like [7].

4.2.2 Recurrent neural network based virtual detection line

During the project, another work on video analysis was done and is represented in the following publication: R.Kadikis ”Recurrent neural network based virtual detection line (the 10th International Conference on Machine Vision ICMV 2017, Vienna, Austria). The main contributions of the paper are described further in this Section.

The paper proposes an efficient method for detection of moving objects in the video. The objects are detected when they cross a virtual detection line. Only the pixels of the detection line are processed, which makes the method computationally efficient. A Recurrent Neural Network processes these pixels. The machine learning approach allows one to train a model that works in different and changing outdoor conditions. Also, the same network can be trained for various detection tasks, which is demonstrated by the tests on vehicle and people counting. In addition, the paper proposes a method for semi-automatic acquisition of labeled training data. The labeling method is used to create training and testing datasets, which in turn are used to train and evaluate the accuracy and efficiency of the detection method. The method shows similar accuracy as the alternative efficient methods but provides greater adaptability and usability for different tasks.

4.2.2.1 Related work

The video processing has been used in vehicle detection for more than thirty years. The paper [8] is a comprehensive guide to the methods developed before 2003, while the [9] discusses some more recent approaches.

Background subtraction is a standard approach for detection tasks with a static camera. The objects of interest may be distinguished from the background by some parameter, such as intensity or color of the pixels [10, 11, 12, 13] or the edges in the image [14].

More robust approaches have used extraction of more complicated features to detect and match objects keypoints. Versatile and widely used feature descriptors include SIFT [15], SURF [16] and ORB [17].

For a few years, the state-of-the-art object detection has been accomplished by the convolutional neural network (CNN) based approaches, such as R-CNN

[18], Faster R-CNN [19], SSD [20] and YOLO9000 [21]. These machine learning based approaches learn to extract and classify task-specific features. The fastest of these methods (YOLO9000) can process 90 small (288x288) images per second on a Geforce GTX Titan X hardware. Thus, CNN based methods are not yet cheaply applicable in video-based applications. Furthermore, the video includes temporal information that is lost by analyzing frames separately.

The recurrent neural networks (RNNs) have also experienced recent revival. Such networks have been successfully applied to the tasks with temporal data, for example, the speech recognition [22]. The internal state of the RNN is updated based not only on the current values of its inputs but also on the previous states of the network, so the network uses previously seen data in the calculation of its current output.

RNNs are an appealing approach for video analysis, but the processing of a whole frame by RNN is computationally demanding. This obstacle can be overcome in such applications as traffic monitoring since vehicles move in a predictable pattern. In such cases, one can use the virtual detector approach where only some part of the frame is processed to detect the moving objects. In this way, the number of processed pixels is significantly reduced. The detection region approach (without the RNN) has been used in several previous works [23, 24, 25, 26]. In these works, one or more detection lines (also called virtual-lines, virtual loop detectors) are defined in the frame, and the objects that cross these lines are detected.

Based on the review of existing approaches, the goal was to develop an adaptable method for moving object detection. This method should be applicable for detection of different objects in different environments while remaining computationally efficient. This goal was achieved by combining the recurrent network approach (specifically, the long short-term memory (LSTM) proposed in [27]) with the idea of efficient virtual detectors in the frame.

4.2.2.2 Method for detection of moving objects

LSTM cell

A simple recurrent neural network computes its current output $\hat{\mathrm{y}}^{(t)}$ by considering not only the current input vector $x^{(t)}$, but also the previous state of the network itself:

$$h^{(t)} = \sigma_h(W_{hx}x^{(t)} + W_{hh}x^{(t-1)} + b_h) \tag{4.2.1}$$

$$\hat{y}^{(t)} = \sigma_y(W_{yh}x^{(t)} + b_y) \tag{4.2.2}$$

, where W and b are weight matrices and vectors, $h^{(t)}$ is a hidden layer vector and σ_h, σ_y are activation functions. To learn the weights of the network, the gradient of error between the predicted output $\hat{y}$ and the correct result y can be backpropagated through time as described in [28]. However, because the weights of the recurrent edge W_{hh} are equal at each time step, the gradients may quickly vanish or explode. A frequently used solution is the Long Short-Term Memory architecture.

A hidden layer of RNN is replaced with an LSTM memory cell shown in Figure 4.2.3. This LSTM consists of internal state nod s_c and several additional nodes g_c, i_c, f_i, o_i. All the later nodes receive the signals $x^{(t)}$ and $h^{(t-1)}$ as inputs. The input node node g_c sums all its inputs and uses nonlinear function to form an activation value.This value is multiplied with the activation from the input gate i_c, which may be 1 or 0, so the i_c decides if the input nodes output is propagated to s_c. This internal state node has a recurrent edge to itself with weight value 1, which allows the unimpeded propagation of error trough time. The forget gate f_c can trigger the deletion of the internal state s_c. The output gate o_c decides if the output of LSTM is propagated further. Mathematically, the LSTM is described in equations (4.2.3 – 4.2.8), where $\odot$ is a pointwise multiplication. Different activation functions might be used instead of $\sigma()$.

$$g^{(t)} = \sigma_g(W_{gx}x^{(t)} + W_{gh}x^{(t-1)} + b_g) \tag{4.2.3}$$

$$i^{(t)} = \sigma_i(W_{ix}x^{(t)} + W_{ih}x^{(t-1)} + b_i) \tag{4.2.4}$$

$$f^{(t)} = \sigma_f(W_{fx}x^{(t)} + W_{fh}x^{(t-1)} + b_f) \tag{4.2.5}$$

$$o^{(t)} = \sigma_o(W_{ox}x^{(t)} + W_{oh}x^{(t-1)} + b_o) \tag{4.2.6}$$

$$s^{(t)} = g^{(t)} \odot i^{(t)} + s^{(t-1)} \odot f^{(t)} \tag{4.2.7}$$

$$h^{(t)} = \sigma_h(s^{(t)}) \odot o^{(t)} \tag{4.2.8}$$

Proposed detection architecture

The first step of the proposed method is for a user to define a detection line in a frame. The Figure 4.2.4 depicts the example virtual detection line. The detector is l pixels long and 1 pixel high line which is perpendicular to the movement of the vehicles. The aim of such line is to detect moving objects that cross it. In the proposed method, only pixels of this line are processed, while the rest of the frame is ignored. Different lengths l can be used, since the defined line of pixels (vector x) is resized to a fixed shape of f_1 x 1 prior entering the neural network. The f_1 is the number of the input neurons of the neural network. The reduced architecture of the proposed artificial neural network is depicted in Figure 4.2.4.

In the concrete proposed implementation, the first layer of the network is a fully connected layer with $f_1 = 100$ neurons. At the frame t, the output vector of fully connected layer is $h^{(t)} = relu(W_{hx}x^{(t)} + b_h)$. The vector $h^{(t)}$ is then forwarded to a recurrent LSTM layer with $r_1 = 100$ neurons. The concrete recurrent layer considers $k = 40$ previous frames to compute its output. This property is the reason why RNN is used in the proposed detector. Such internal memory allows the network not only to recognize if there are some objects on

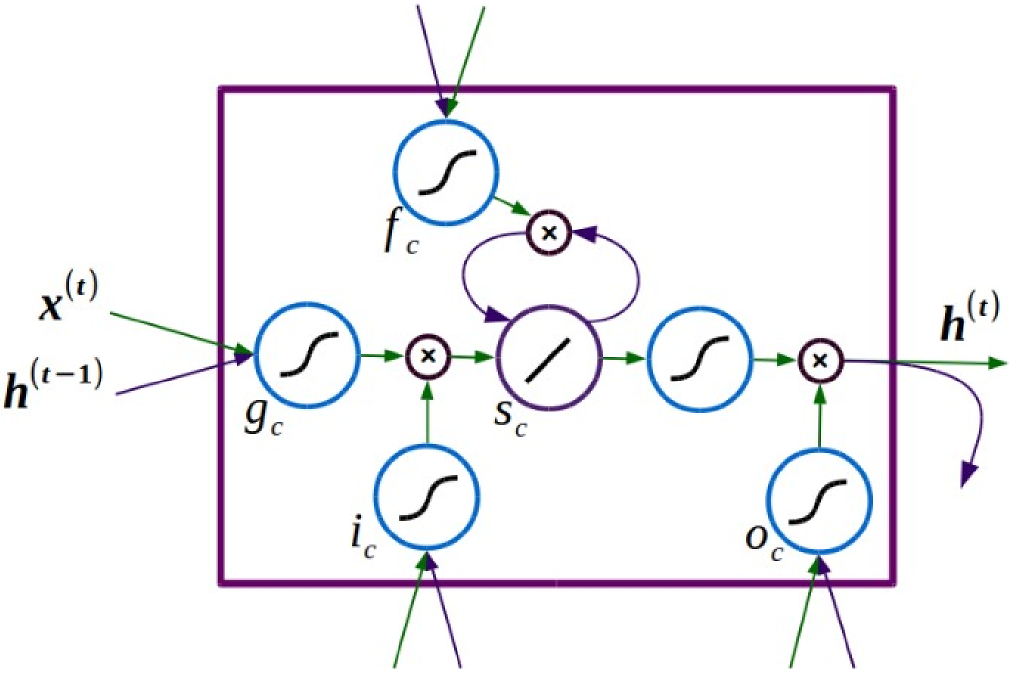

Figure 4.2.3: Long Short-Term Memory cell.

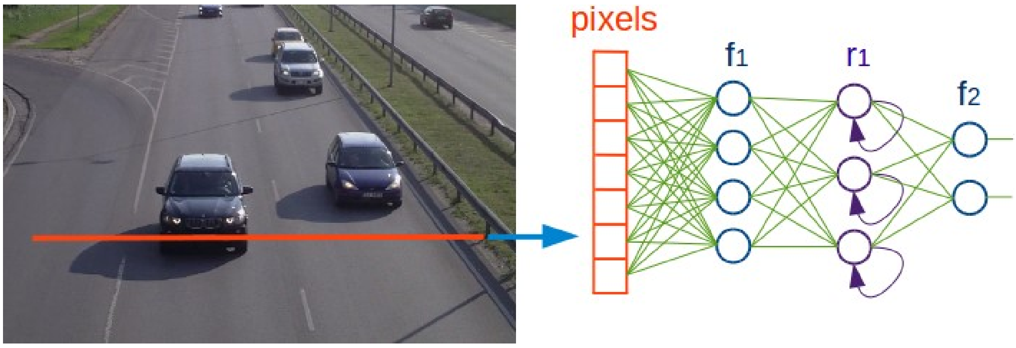

Figure 4.2.4: RNN based virtual detection line.

the detection line, but also devise if some objects have recently left the line and in what direction the line was crossed. The computations of LSTM layer were already discussed in the previous section. The final layer of proposed network is another fully connected layer with $f_2 = 10$ neurons that correspond to the 10 possible output classes. The following subsection describes in detail what those classes represent.

All activation functions in the network are linear rectifiers $relu(x) = max(0,x)$. The goal of training such model is to learn all the weights, so that the network returns a preferred class for each input vector $x^{(t)}$. There are different ways how to choose the expected class for each frame; therefore, the next section is dedicated to finding appropriate type of labeling for object detection task.

Data labeling modes

There are several possible events on the detection line that the output class labels may represent. The current paper considers three labeling modes. In the first mode, the output label corresponds to the current number of objects on the detection line. The drawback of this mode is that two closely following objects might create a sequence of labels (1,1,1,1,1). Two objects have crossed the line, but the correctly predicted sequence does not allow to determine that at the third frame one object has left the line, and another object has entered the detection line.

The second considered labeling mode codes how many objects had left the line at the current frame. This mode allows unambiguous counting of objects that have fully crossed the detection line. If several objects exit the line simultaneously, their count is also the label of this frame. This mode also eases the task of manually labeling the training data since the labeler only needs to add one label per object, not per every frame. However, the labeled dataset of this kind will be unbalanced since in many practical applications most of the labels will be zeros.

The final proposed labeling mode is a combination of two previous modes and is depicted in Figure 4.2.5.a. The human labeler still only needs to mark the frames where the objects have left the detection line; however, the actual label of any sequence in the video is determined by counting how many objects have left the line in the last $k/2$ frames. In the example of Figure 4.2.5.a, five objects have passed detection line in the time of 28 frames. Each row represents pixels of the detection line at consecutive frames. A number inside each row shows how many objects have left the line at this frame. Regardless of the direction of objects movement, in the Figure 4.2.5, the bottom part of the object is its latest presence on the detector. In the example, the length of sequence $k = 22$. The latest half of the sequence is colored. The number of departed objects in this colored part is the final label of the sequence. So, the label of current and the following sequence is 3; next after that is 2.

While the trained network predicts the label of each frame (analyzing the sequence of k last frames), the actual detection of the moving object takes in to account several separate predictions. The global counter increases only if the currently predicted count is greater than current global count for at least $k/4$ consecutive frames. In this way, the influence of prediction errors at each individual frame is reduced; however, object is counted with a small delay.

Software for data labeling

The supervised machine learning depends on the availability of labeled data. The proposed object detection algorithm significantly differs from the ILSVRC winning algorithms, and it cannot be trained with such labeled datasets as the ImageNet. Therefore, a custom training dataset must be created. This section proposes a specific GUI based approach for data labeling. Its goal is to significantly accelerate the creation of needed datasets.

At the start of labeling program, the user must define the position and length of the detection line in the first frame of the video (two mouse clicks set the

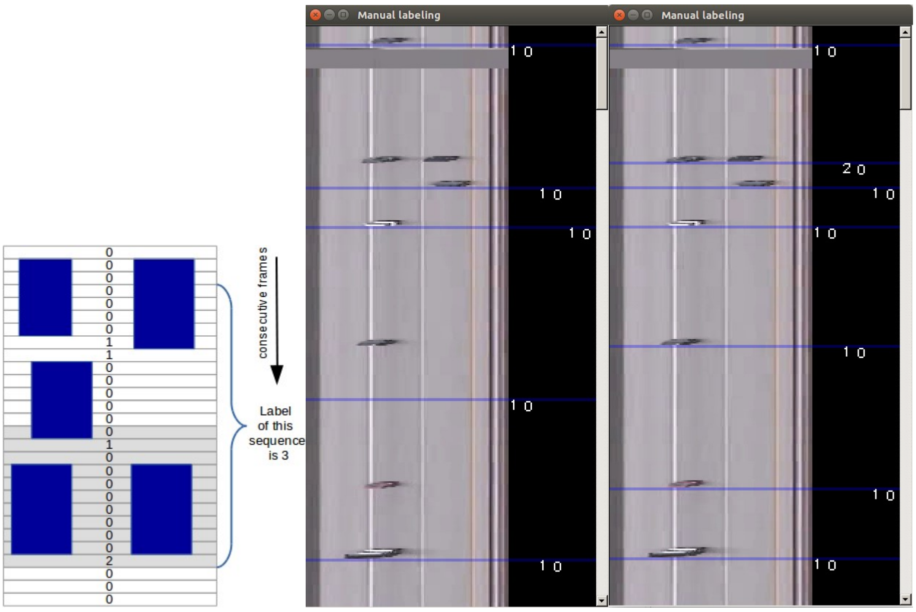

(a) (b) (c)

Figure 4.2.5: Labeling of data a) a type of labeling where the label is equal to the number of vehicles that have left the line in several last frames; b) The GUI for data labeling before and c) after the user has manually corrected the mistakes of automatic labeling.

endpoints of the line). Then an automatic labeling stage begins, which uses classic background subtraction approach. In the first frame, the background line is equal to the current line of the frame, so it is crucial to choose detection line at the location and time when it is empty.

The video frames are processed in their original order. The detection line of the current frame L_c is subtracted from the background line L_b. The absolute value of this difference is thresholder with a manually chosen threshold. At those frames when less than 20 % of the pixels on the threshold line are white, the background line is updated:

$$L_b = L_b \cdot 0.95 + L_c \cdot 0.05 \tag{4.2.9}$$

Each threshold line becomes a row in a new spatio-temporal image. After processing of all separate frames, the acquired spatio-temporal threshold image undergoes further processing to reduce the impact of noise. The morphological closing with a square kernel of size 3x3 is followed by morphological opening with a 5x5 kernel. Further, values of all zero pixels surrounded by pixels with value 1 also become 1.

The processed spatio-temporal image is then automatically labeled. Continuous white regions are detected at each row of the image. The number of the white segments longer than 10 % of the length of the whole row becomes the temporal label of each row (first label mode). Then these labels are converted to the preferred label mode. Starting from the first row and moving down, when the temporal label of the row i is bigger than the label of $i + 1$, the final label of row i+1 becomes equal to the difference of labels i and $i + 1$. The final labels of all other rows become 0.

The automatic stage of labeling method does not consume human time, but it is also less accurate than humans. The next labeling stage consists of GUI (Figures 4.2.5 b and c) which allows fast manual detection and correction of the errors made in the automatic stage. Each vertical line in the figure depicts a frame when the label of the detection line changes. The number on the right of each dividing line is the corresponding label of the rows under this line. In the Figure 4.2.5.b, five lines indicate five frames with label 1. Those frames are immediately followed by many frames with label 0.

The proposed GUI allows the user to scroll through the whole labeled spatio-temporal image and change the errors with mouse clicks. The left click above the dividing line moves this line one row upwards. A left click below the line deletes it. The rows under the deleted line get the label that was above this line.

The right mouse click creates a new dividing line. The precise position of this line is determined automatically. A small region of the row at the cursor position is compared to same regions on the rows upward the current one. Where the difference between the current row and some upward row is larger than a set threshold, the algorithm places the new dividing line. In this way, the user needs to only approximately point out the position of the object, which makes the manual labeling even faster. If the user indicated position already have a dividing line with label m, then this label becomes $m + 1$. So, in the example of Figure 4.2.5.c, the dividing line with the label 2 was created by clicking once somewhere under each of two objects that this label corresponds to.

When the user has inspected and corrected the whole spatio-temporal image, the GUI is closed, the labels are encoded as one-hot vectors and saved to the hard drive along with the spatio-temporal image.

4.2.2.3 Tests

The proposed object detection and data labeling methods were implemented in Python 3. The TensorFlow framework was used for implementation and training of RNN network, while OpenCV library was used for other image processing tasks. The PyQt4 library was used for the GUI based labeling method.

Accuracy

The unlabeled videos of road traffic were acquired from open streaming cameras at [29] and [30]. Figure 4.2.6 shows example frames. Both traffic cameras acquire 25 FPS with resolutions 650x480 and 352x240. Videos are of poor quality with many compression artifacts. For more convenient labeling, the video stream is downloaded and stored in 1.5-2 minute long videos. The detection line for each short video is set manually and differs in length. It varies between 200 to 400 pixels for the videos from the first camera and 70 to 150 pixels for the second camera. Altogether 427 short videos were labeled. 100 of those videos were separated as the test set and used only to get the final results in Table 4.2.2.a. The rest videos were further divided into training (70 %) and validation (30 %) data.

After 6 hours of training accelerated by NVIDIA Tesla K20 GPU, the network learns to correctly classify 99.4 % of training sequences and 95.6 % of validation sequences.

Figure 4.2.6: Two frames from open traffic cameras and a frame from a different camera that was not used in the training of the network.

While training, the network tries to correctly classify each frame. In the practical application, it is not crucial for the moving object to be counted at the same frame as was marked in the labeled data since the labeling also includes subjectivity of the labeler. If the model detects the object two frames later than human and no additional false objects are detected, the result is still valid for practical applications. Therefore, the following testing procedure was implemented.

The labels of the test set are acquired in the same way as the labels for training data. These labels are stored as a FxM matrix, where F is the number of frames and M is the number of possible classes. All the frames with the label greater than 0 correspond to the detection of at least one vehicle. When the test video is forwarded trough the trained network, the test algorithm chooses the same position of detection line that was used for labeling. The predicted classes are also saved as a matrix with size FxM. Corresponding pairs of detections (frames with a label other than 0) are found in the predicted and labeled matrices. The pairs are not allowed to be more than 25 frames apart (a second in the used videos). All pairless detections of object in the prediction matrix are false positive detections, while all unpaired detections in the label matrix correspond to false negative detections.

The described tests were performed on the videos from the same traffic cameras from which the training videos were acquired. Additional tests (Table 4.2.2.b) were conducted to see if the trained network can be used on videos from previously unseen cameras without additional finetuning of the network. This camera had a different resolution (70x480) and framerate of 25 FPS. The length of detection line was longer than in training videos - 456 pixels.

The same neural network was also trained and tested for people counting. The videos were acquired from [31]. They had a resolution of 800x450 pixels and 15 FPS. Figure 4.2.7 shows the example frames. The counting task was modified so that only people going in one direction are counted. Figure 4.2.7.c

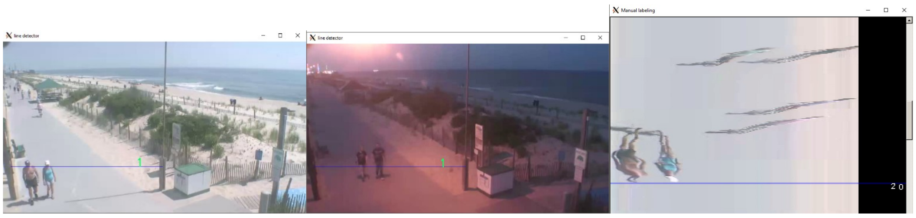

(a) (b) (c)

Figure 4.2.7: Two frames from open camera and a labeling of this data.

shows the labeling GUI with an appropriate labeling. Although six people have crossed the line in the depicted time, only two crossed it in the direction from top to bottom. They crossed the detector simultaneously; therefore, the labeler has labeled only one frame with the label 2. The movement intensity of people in the used videos is similar in both directions, therefore, if the detection line would not be able to differentiate between the directions, there would be a lot of false positive detection instances, which is not the case (Table 4.2.2.c).

Table 4.2.2 shows the actual number of object in the test videos and a number returned by the method. The main test results (column a) show the precision 0.949 and recall 0.958. This result is similar to the claimed precision and recall of alternative efficient virtual detection line based methods. For example, the precision of method [24] is 0.86-0.96, while the recall is 0.89-0.96. In [26] the average precision is 0.965, and the average recall is 0.969. These results are only suggestive since all these papers use different test videos. The proposed method was trained and tested on videos with lower quality and many artifacts. However, the most important benefit of the proposed method over other efficient detector based methods is its applicability to counting different kinds of objects.

Table 4.2.2: Counting results and measurement of RNN inference speed on CPU.

Camera	a – Traffic	b – Traffic	c – Traffic
Ground truth	4238	121	285
Predicted count	4278	108	245
True Positives	4059	103	209
False Positives	219	5	36
False Negatives	179	18	76

Speed

The average time of processing a single frame was measured. The length of detection line has little effect on the speed of the method since all the lines are resized to a specified length f_1 before entering the RNN. Essential parameters that affect the speed are the network sizes - number of layers and neurons and the depth in time k. Table 4.2.2 shows how the measured speed of the detection algorithm depends on the temporal depth of RNN. The speed was measured on IntelR XeonR CPU E5-2650 v2 2.60 GHz, while the resolution of input video was 800x450. The length of detection line was 400 pixels and $f_1 = 100$. The

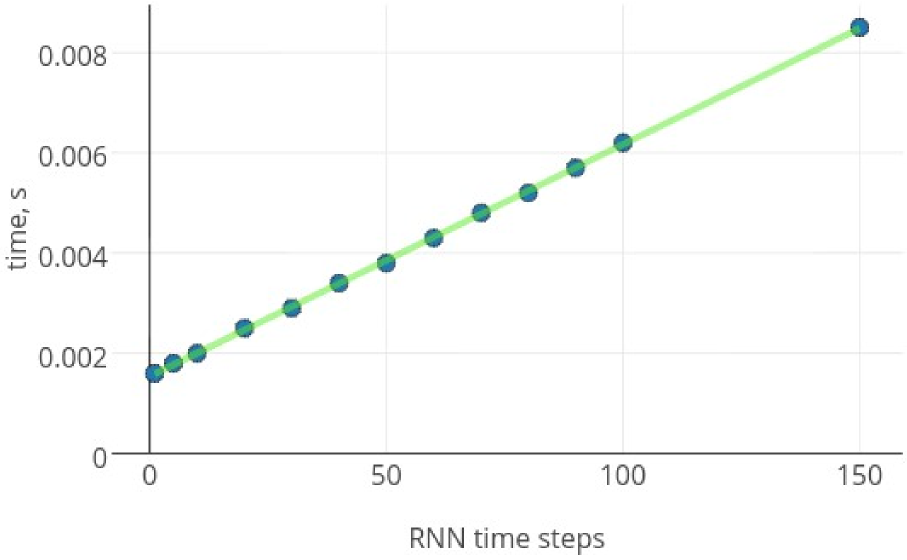

Figure 4.2.8

test shows a linear dependence between inference speed and k. The choice of depth depends on the specific tasks. Slow moving objects and a high frame rate of input video may require RNNs with deeper memory. In current example, the FPS of video was 15. So, if one chooses to use RNN that can remember 50 previous steps, the information from up to 3 second past may be used to decide current output of the network.

The proposed detection method is not a rival of such modern object detection methods as R-CNN or YOLO regarding the versatility or accuracy. For example, if trained with appropriate labeled data, YOLO might show almost perfect result on the same limited task of object counting. However, the proposed method significantly reduces the processing speed. Running the [32] implementation of YOLOs fast version tiny-yolo on the same single processor, one image is forwarded through the network in 0.34 seconds, while the proposed method needs 0.0035 seconds. For this experiment, YOLO model was not retrained for the specific task, but this should not significantly affect its inference speed.

4.2.2.4 Approbation: Car counting system

The object counting technology based on virtual line and neural network (described in the Section above) was approbated at the Turiba University (`http://www.turiba.lv/en`). It was applied on the real-time surveillance videos for car counting. The developed system gathers information/statistics about car parking. The system is successfully tested, and the review (written in Latvian) is obtained. It recommends the developed system. The system readiness level is sufficient, and the technology is ready for use in industry.

4.2.2.5 Conclusions

This work proposes a novel method for detection of moving objects. The combination of the virtual detector approach and the recurrent neural network results in an efficient and adaptable object detector. The efficiency comes from the detector line approach and makes the proposed method scalable for such applications as Intelligent Transportation Systems. In such applications, each camera can be supplemented by a cheap video processing computer (e.g. Raspberry Pi) and still acquire the information about the road in real time. As shown by tests, this method is similar in accuracy with other detection line based methods. However, as demonstrated by additional tests, it can be retrained and adapted for different conditions, roads or even objects, without additional changes in the architecture. With accordingly labeled data, RNN allows the detection of the direction of moving objects by analyzing pixels from a single line in the video.

4.2.3 Summary

The following points can be listed and commented representing the main project results obtained by the BIGDATA group:

1. Understanding deep learning and setting up High Performance Computing environment. In this preparation stage, a lot of work has been done for better understanding deep learning and preparation of computing environment: 1) Deep learning was recognized as the most suited method for video signal and other signal content analysis. The considered smart city data analysis was based on deep learning and further experimentation was mainly focused on investigation of artificial neural networks; 2) Deep learning examples of classification were implemented using Octave. The Octave model of artificial neural networks was created for better understanding of deep learning. It allows experimentally simulate various learning conditions and various network layer configurations. 3) High Performance Computing environment with deep learning frameworks was configured. It consists of configuration of the 12 EDI HPC servers with NVIDIA Tesla K40 graphic cards. Now servers run Ubuntu operating system and Caffe, Torch and Tensorflow deep learning frameworks. Also, it includes creation of deep learning test examples to test deep network training environment. The example of two class classification was created using Deep Learning on labeled data. For this purpose, Cat or rabbit image detector was built (achieving accuracy more than 80 %). The trained classifier was based on AlexNet deep network architecture and ImageNet labeled images [6, 33]. 4) bachelor thesis was prepared: I.Albertina Object tracking in multi-camera environment exploring YOLO and other deep neural networks for object tracking. More results can be found: `https://vault.edi.lv/index.php/s/nFYOQ2ZY6inbuwv`

2. Face identification in images. For exploration of unique object descriptors, the human facial images were processed and deep learning neural networks

were trained. The trained deep neural network descriptor converts any image with face into a feature vector, which can be compared to another vector to find the class members. The descriptor is based on AlexNet artificial neural network (ANN) architecture and trained on COLOR-FERET image data set. Experiments show that trained ANN finally achieves 94 % accuracy on COLOR- FERET frontal image subset containing more than 100 classes in the testing set. More detailed description is presented in the paper K. Sudars ”Face Recognition Face2vec Based on Deep Learning: Small Database Case”. This paper is published in the journal Automatic Control and Computer Science indexed in SCOPUS. Face image identification in images could be improved by performing training on much larger facial image data sets. However, this was not a prime goal of BIGDATA team in this project.

3. Object counting in videos. During the project, R.Kadikis has prepared and predefended draft of his PhD work Efficient methods for detection and characterization of moving objects in video and he is ready to receive PhD degree in the near future. Also, the work on video analysis was presented in a publication: R.Kadikis ”Recurrent neural network based virtual detection line” (the 10th International Conference on Machine Vision ICMV 2017, Vienna, Austria). The developed recurrent neural network counts objects crossing the line. To acquire labeled data for the moving object detector, two approaches were investigated. One of the approaches resulted in a method and software for semi-automatic labeling. According to this approach, an algorithm performs automatic and fast but erroneous labeling. Then a human is presented with a GUI that allows convenient error correction. The second approach was based on the generation of synthetic data using the game engine. Using this engine, a simplified environment with moving spheres was developed. This simulation will allow to generate a large amount of labeled data which in turn will allow to estimate if this approach of data generation is promising for more complex environments.

   The system was approbated under real-time conditions at the Turiba University (`http://www.turiba.lv/en`). It was applied on real-time surveillance videos and gathers statistics about car parking. The system was successfully tested, and the review (written in Latvian) was obtained. It concludes that the technology readiness level is sufficient for use in industry.

4. Efficient sensor data gathering. One of the main project results in the field of efficient data acquisition is K. Ozols dissertation: K.Ozols ”Asynchronous Data Acquisition of Electroencephalogram Signals”. K. Ozols has received a PhD degree from Riga Technical University. Other results of this field are shown in scientific papers: 1) the data acquisition method is developed and results can be found in a paper K.Ozols ”Implementation of reception and real-time decoding of ASDM encoded and wirelessly transmitted signals”, IEEE MAREW 2015; 2) interdisciplinary Baltic Electronics Conference 2016 was attended and the paper presented there in

collaboration with another colleagues from EDI: K. Sudars, I.Bilinskis, E.Buls, "Discrete Fourier Transform of the signals recovered by using high-performance Event Timers"; 3) Signal Processing Symposium was attended and the paper presented: I.Bilinskis, E.Boole, K.Sudars, "Combination of Periodic and Alias-free Non-uniform Signal Sampling for Wideband Signal Digitizing and Compressed Transmitting Based on Picosecond-Resolution Event Timing", `http://spsympo.ise.pw.edu.pl/`

4.2.4 Conclusions

During the project (2014-2017) the artificial neural networks have become the choice number one for the development of all kind of analysis systems. It includes the development of applications for smart cities for safety purposes. Deep learning is used in the systems developed during the project by the BIGDATA team. Currently, the deep learning approach is exclusively used in all state-of-the-art image and speech recognition systems. The companies like Facebook, Google, Baidu etc. are developing technologies based on artificial neural networks.

A big problem in deep learning is the need for a large amount of labeled data. It puts limits on many smart city applications and ideas. Further research should be focused more on methods of unsupervised deep learning.

The project contributes to smart city safety and security by development of two systems described in this Chapter and as well as in publications: 1) K. Sudars, Face Recognition Face2vec Based on Deep Learning: Small Database Case, 2) R.Kadikis, Recurrent neural network based virtual detection line.

Also, some contributions were done in collaboration with colleagues from IECS-EDI, mainly focusing on sensor data acquisition. They are described in publications listed in the Chapter "Summary of project results.

The quantitative results of the BIGDATA team can be summarized as follows: 5 SCOPUS publications prepared, 4 scientific conferences attended, 2 video data analysis systems developed (1 approbated in real conditions), 2 PhD thesis (1 PhD degree received, 1 PhD work finished) and 1 bachelor thesis prepared.

Chapter 4.3

EDI REMSENS group: Investigation of possibilities to use remote sensing data for solving city monitoring tasks

Activities of the REMSENS group were focused of the following tasks related to exploitation of remote sensing data in smart cities:

- development of remote sensing data processing methods for urban land use mapping;
- development of tools for vegetation mapping and its change detection;
- development of precise land surface elevation model from LiDAR data and software for simulation of flooding to assist authorities in flood risk management.

Theoretical studies of land use classification methods were performed within the first task. They included: 1) the study of data fusion possibilities when the area of interest is scanned using the RGB camera and a thermal hyperspectral sensor; 2) the study of informative band selection methods for classification of hyperspectral images; 3) the study of the possibility to exploit fuzzy logic for classification of satellite images. The other two tasks were mainly oriented towards development of algorithms for practical exploitation of remote sensing data for the management of urban territories.

4.3.1 Remote sensing data processing methods for urban land use mapping

4.3.1.1 Classification of land use categories from multisensor data

Multisensor data fusion possibilities were examined for the case when the data were obtained from sensors with different spatial resolution. Classifiers were developed to distinguish between land use categories, based on Bayesian classification principles. They were tested using the data published within the IEEE Geoscience and Remote Sensing section data fusion contest (DFC) (see `http://cucciolo.dibe.unige.it/IPRS/IEEE_GRSS_IADFTC_2014_Data_Fusion_Contest.htm`).

The task of the contest was to classify remote sensing images of land use categories, based on the RGB image from the RGB sensor and the TI image from the thermal sensor in the wavelength range from 7.8 μm to 11.5 μm, both obtained during overflights of the same urban area.

Only subset images from one overflight of the RGB sensor and corresponding part of the TI image were processed, including all ground truth regions. Ground truth for the DFC was presented in a separate image with the same spatial resolution as the RGB image and covered $\sim$17% of the whole area of the subset image. To prepare ground truth for the TI image, only pixels fully included in defined ground truth regions were used, comprising $\sim$12% of the whole area of the subset TI image.

Our approach was to perform classification in two stages: in the first stage, two separate classifiers were designed, each using one of the available images only; in the second stage, these two classifiers were combined to increase the accuracy.

Classifiers of land-use categories were developed on the basis of Bayesian classification principles using Gaussian, Dirichlet and gamma distributions for developing multi-dimensional data models. Classifiers were trained using available ground truth and checked for accuracy against pixels from the same area. RGB image with the best obtained classification results is shown in Fig. 4.3.1.

Combined classification that uses both images (see. Fig. 4.3.2) allows to get better results than the individual image classifiers. It was noticed that the problems of the classifier using RGB image only were largely resolved on the basis of TI image data.

By checking use of the other distributions in the data model, it was concluded that the Gaussian distribution is the most appropriate. The results obtained by using Dirichlet and gamma distributions were worse than in the Gaussian distribution case.

The idea was put forward that it might be appropriate to use different probability distributions for processing of RGB and TI images. However the most accurate combined classifier was obtained when the Gaussian model was used for both images.

During studies of application of different distributions, an approach for com-

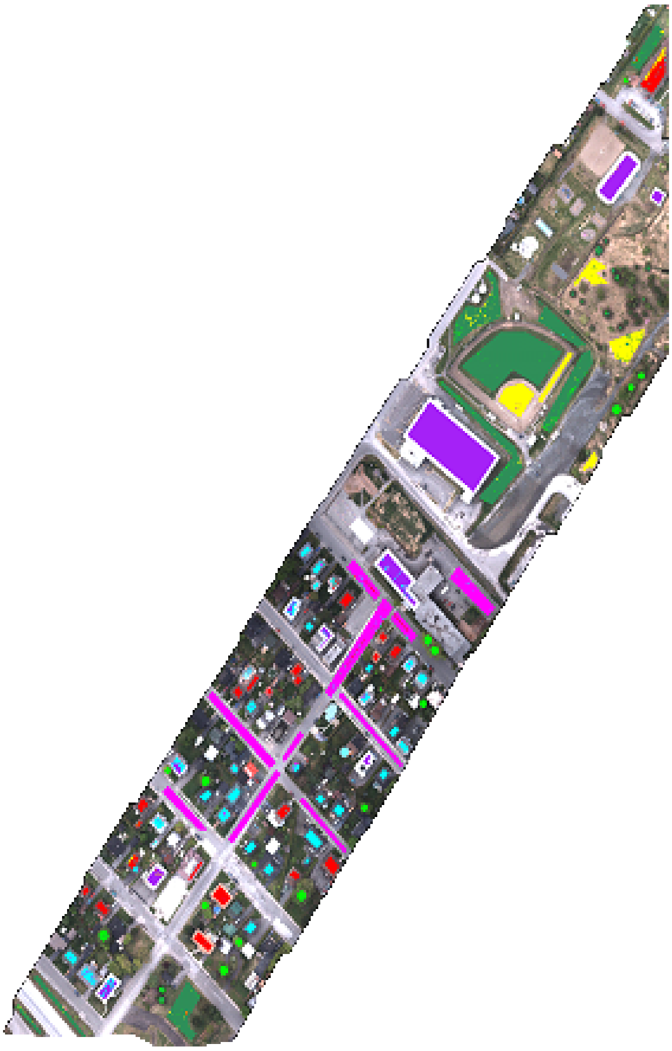

Figure 4.3.1: Processed RGB image with marked classified pixels (the best obtained classification results are shown.

bining distributions in a data model was developed, and it turned out that such approach is productive. Applications of different combinations of distributions were studied. The best results were obtained when all three distribution were combined in the data model (see Fig. 4.3.3). We put forward the hypothesis that combination of distributions slightly improves the model so that such combination can be used intentionally to improve classification results.

Described results were presented in the conference Electronics 2015 and published in the paper "Classification of Multisensor Images with Different Spatial Resolution" (see `http://eejournal.ktu.lt/index.php/elt/article/view/13333`).

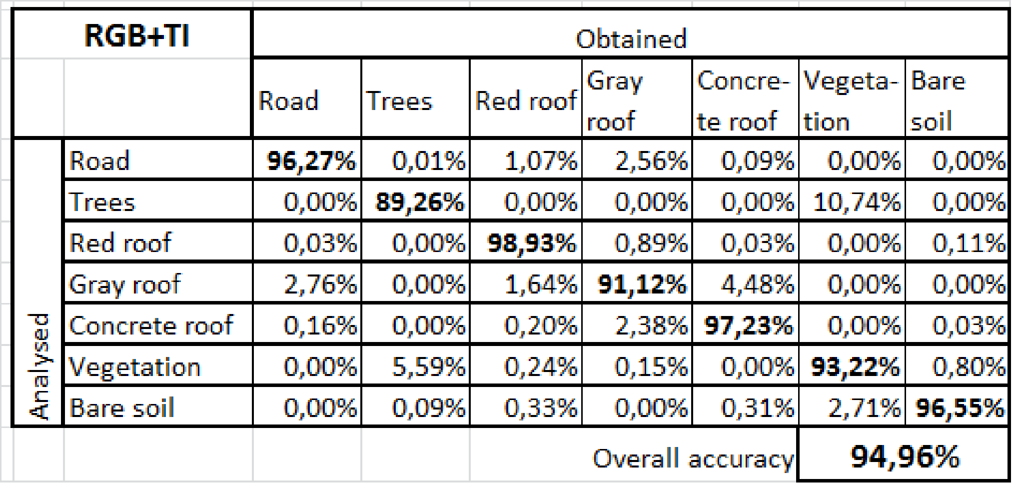

RGB+TI		Obtained						
		Road	Trees	Red roof	Gray roof	Concre-te roof	Vegeta-tion	Bare soil
Analysed	Road	**96,27%**	0,01%	1,07%	2,56%	0,09%	0,00%	0,00%
	Trees	0,00%	**89,26%**	0,00%	0,00%	0,00%	10,74%	0,00%
	Red roof	0,03%	0,00%	**98,93%**	0,89%	0,03%	0,00%	0,11%
	Gray roof	2,76%	0,00%	1,64%	**91,12%**	4,48%	0,00%	0,00%
	Concrete roof	0,16%	0,00%	0,20%	2,38%	**97,23%**	0,00%	0,03%
	Vegetation	0,00%	5,59%	0,24%	0,15%	0,00%	**93,22%**	0,80%
	Bare soil	0,00%	0,09%	0,33%	0,00%	0,31%	2,71%	**96,55%**
						Overall accuracy	**94,96%**	

Figure 4.3.2: Classification results of ground truth pixels, obtained by using Gaussian distribution model and exploiting data from both images.

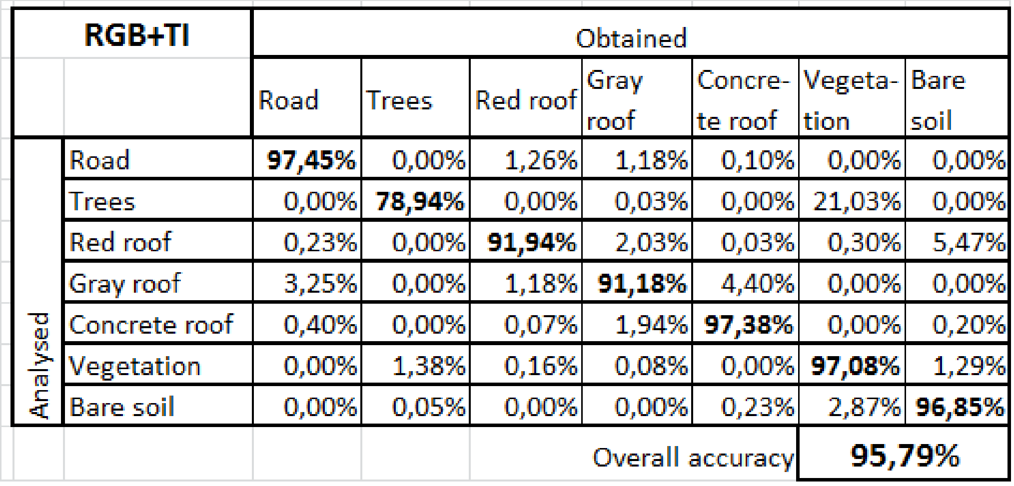

RGB+TI		Obtained						
		Road	Trees	Red roof	Gray roof	Concre-te roof	Vegeta-tion	Bare soil
Analysed	Road	**97,45%**	0,00%	1,26%	1,18%	0,10%	0,00%	0,00%
	Trees	0,00%	**78,94%**	0,00%	0,03%	0,00%	21,03%	0,00%
	Red roof	0,23%	0,00%	**91,94%**	2,03%	0,03%	0,30%	5,47%
	Gray roof	3,25%	0,00%	1,18%	**91,18%**	4,40%	0,00%	0,00%
	Concrete roof	0,40%	0,00%	0,07%	1,94%	**97,38%**	0,00%	0,20%
	Vegetation	0,00%	1,38%	0,16%	0,08%	0,00%	**97,08%**	1,29%
	Bare soil	0,00%	0,05%	0,00%	0,00%	0,23%	2,87%	**96,85%**
						Overall accuracy	**95,79%**	

Figure 4.3.3: Classification results of ground truth pixels, obtained by using data model combined from Gaussian, Dirichlet and gamma distributions and exploiting data from both images.

4.3.1.2 Selection of informative bands for classification of hyperspectral images

Two novel and relatively simple unsupervised procedures for the selection of informative small subsets of spectral bands in hyperspectral images were developed. The preprocessing procedure was proposed to detect and exclude spectral bands where the acquired images are characterized by low signal-to-noise ratio. Development of the procedures was based on the following principles: 1) to ensure the informativeness of the subsets, bands featuring higher entropy are included in subsets; 2) the correlation of band images is restricted to avoid redundancy of the subsets. The subsets obtained were characterized by the performance of classifiers using only data from included bands.

The Entropy Multiple Correlation Ratio (EMCR) procedure employs the entropy-correlation ratio for the selection of spectral bands. The EMCR procedure creates a set of informative bands iteratively by including the band with the highest ratio between its entropy and the absolute value of correlation with already included bands. Bands featuring a too high correlation with one of already included bands are excluded from consideration beforehand.

The Entropy-based Correlated Band Grouping (ECBG) procedure divides the spectrum into groups of bands featuring highly correlated images. The ECBG procedure was developed taking into consideration the following:

- Adjacent correlated bands compose subranges of the spectrum, and each subrange should be represented in the subset of bands employed in the classification process, because it corresponds to the specific physical properties of real object categories;
- The most informative band in each subrange can be chosen on the basis of entropy of the corresponding image.

The ECBG procedure iteratively finds groups of highly correlated spectral bands and forms a subset of informative spectral bands by including the band with the highest entropy from each group in the subset. It provided better results than the alternatives if the number of selected bands was low.

Classification accuracy obtained for the widely known "Indian Pines" hyperspectral image using spectral bands selected by the ECBG procedure is illustrated by Fig. 4.3.4 and Fig.4.3.5.

Another advantage of the ECBG procedure is the possibility of averaging the images obtained for spectral bands within the groups found. It is shown that classification results are significantly improved if such an averaging is used. In the data acquisition practice, it can be used for purposeful merging of spectral bands in the configuration of hyperspectral imagers, which allows one to reduce the amount of data to be saved in real time and thus helps one to improve the achievable spatial resolution.

Results of these studies were presented at the conference BEC-2016 and are in preparation for publication in the International Journal of Remote Sensing (minor corrections before publication suggested by reviewers). Reviewed paper together with the decision letter is presented in Appendix 4.1.

4.3.1.3 Classification of multispectral remote sensing images using fuzzy logic

The problem of mixed pixels is frequently faced in classification of satellite images with moderate spatial resolution. For example, 10m resolution of Sentinel-2 images result in a rather large percentage of mixed pixels representing borders between areas of different categories. In addition, in supervised classification, pixels related to "ground truth" for the categories of interest may also be mixed

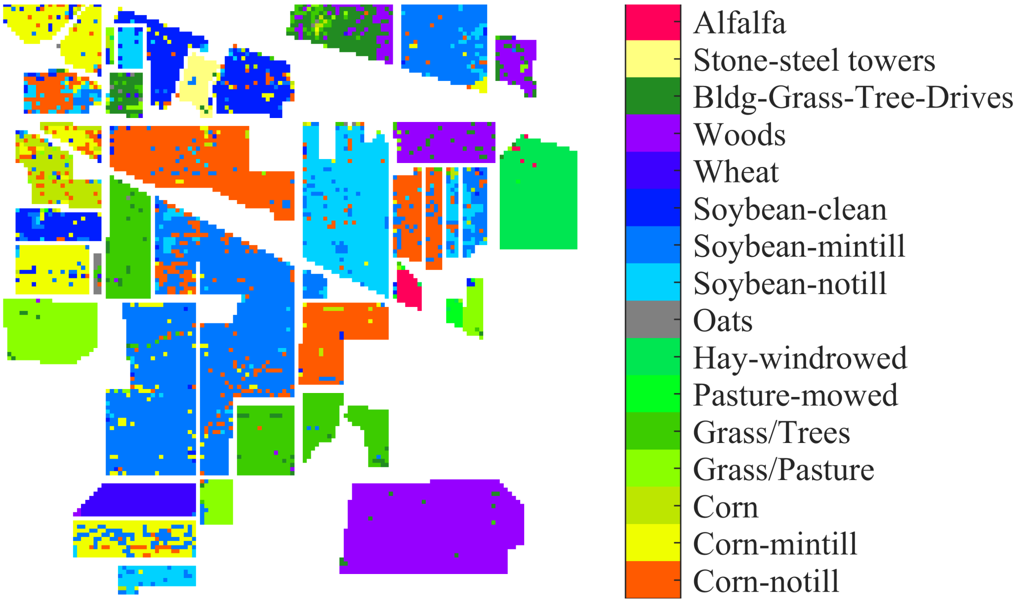

Figure 4.3.4: Pixel classification results of "Indian Pines" marked data.

e.g. when coniferous and deciduous forests must be classified to separate categories. To deal with this problem, application of fuzzy logic is considered, which allows to model such situation and deal with both "clean" and mixed pixels. Rather good results have been achieved using Bayesian classifier based on various statistical distributions, as described in section 4.3.1.1. Therefore here we focused on fuzzy generalization of the Bayesian classifier in order to analyze the differences in performance of crisp (not employing fuzzy approach) and fuzzy classifiers.

Input data source is an image (I) of land surface area close to Riga taken by WorldView-2 satellite on 11^{th} of June, 2017. Image contains 8 spectral bands with wavelengths from 400 to 1040 nm. Pixels of the image are represented by vectors $x = (x_1, x_2, ..., x_8)^T$ where x_i is the sensed light intensity of the corresponding spectral band. Classification of the pixels in 5 categories (deciduous trees, coniferous trees, grass, water and agricultural land) was done using selected areas of the image as *ground truth*. One fifth of these pixels (chosen randomly) were used to design the intended classifiers and therefore they are elements of the design set, the rest were used to validate the classification results. The main problem of such choosing is that the natural growth areas are rarely homogeneous and therefore the *ground truth* chosen is probably imprecise and contains elements that does not actually belong to the category selected. Nevertheless it is nearly impossible to acquire perfectly homogeneous sets for *ground truth*. Let us denote by S the design set of pixels in image I. Pixel classifiers designed within this research are constructed as Bayes type classifiers based on Gaussian distribution. As there is no information available about the prior probabilities of categories, they are assumed to be equal.

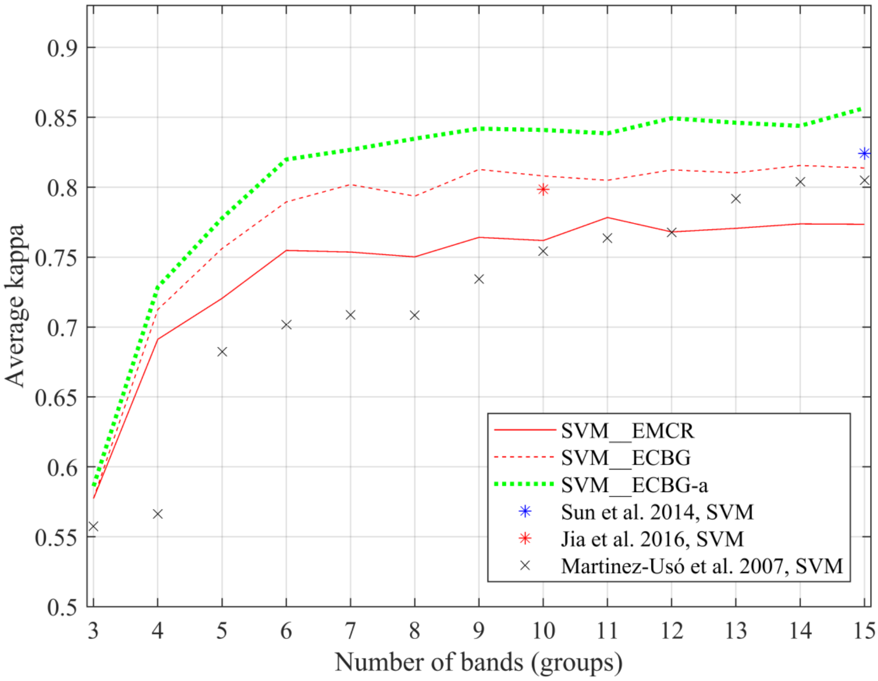

Figure 4.3.5: Average kappa for the Indian Pines dataset from 20 experiments with different design sets of pixels. 20% of the ground truth pixels were used for training and all the rest for testing. Support vector machine (SVM)- based classifiers used. ECBG procedure with data averaging within found groups designated by ECBG-a.

To use the n-dimensional Gaussian distribution as a model for the pixel vectors of category k, it is necessary to calculate the estimates of parameters μ_k and Σ_k of the probability density function

$$p_{X_k} = \frac{1}{\sqrt{(2\pi)^n}\sqrt{|\Sigma_k|}} exp\Big(-1/2(x-\bar{x}_k)^T \Sigma_k^{-1}(x-\bar{x}_k)\Big), \tag{4.3.1}$$

where $\bar{x}_k = E(X_k)$ is the mean value and $\Sigma_k = E\Big((X_k-\bar{x}_k)(X_k-\bar{x}_k)^T\Big)$ is the covariance matrix. In a crisp classifier these two parameters are all that is needed for training. Fuzzy classifier uses modified formulas for mean and covariance matrix. Fuzzy generalization of mean and covariance matrix is defined as

$$\bar{x}_k^* = \frac{\sum_{i=1}^{n_k} \mu_k(x_i)x_i}{\sum_{i=1}^{n_k} \mu_k(x_i)} \tag{4.3.2}$$

and

$$\Sigma_k^* = \frac{\sum_{i=1}^{n_k} \mu_k(x_i)(x_i-\bar{x}_k^*)(x_i-\bar{x}_k^*)^T}{\sum_{i=1}^{n_k} \mu_k(x_i)}, \tag{4.3.3}$$

where n_k is the number of elements in the training set of class k and $\mu_k(x_i)$ is the membership degree of a pixel x_i to class k. Membership degree is defined as

$$\mu_k = \frac{p_{X_k}}{\sum_{j=1}^{k} p_{X_j}}. \qquad (4.3.4)$$

Evidently definition of the membership degree is circular. In practical calculations, membership degree is found iteratively - starting with crisp parameters and recalculating until there is no significant variation in the present and previous estimation of parameters in consecutive iterations.

As indicated before, natural growth areas usually are not homogeneous, and therefore areas marked as *ground truth* contains impurities. As it is practically impossible to avoid errors while choosing training sets, those sets has to be filtered afterwards. In this study, data filtering was performed by iteratively finding membership degrees of training set pixels and if the membership degree to pixels supposed category is less than 0.7 then the pixel is excluded from the training set.

The results obtained are illustrated in the table below.

Threshold		Deciduous	Coniferous	Grass	Agriculture	Water	Overall
	Crisp	57,3 %	69,8 %	89,2 %	99,8 %	96,6 %	93,3 %
	Fuzzy	71,3 %	84,5 %	94,2 %	99,9 %	97,3 %	95,7 %
0,7	Crisp	72,1 %	85,5 %	94,7 %	99,9 %	97,4 %	95,9 %
	Fuzzy	72,2 %	85,8 %	94,9 %	99,9 %	97,4 %	96,0 %

Before filtering of the training set, fuzzy classifier performed noticeably better. After filtering, the differences were minor. We can conclude that filtering of the training set using the fuzzy approach is a useful tool that can improve the classification accuracy.

Research within this topic is continued.

4.3.2 Development of tools for vegetation mapping and its change detection

Activities within this task were oriented towards accumulation of necessary knowledge and development of practical tools for detection of vegetation changes in urban and suburban areas that can be used by municipalities to monitor situation in that respect. Sample images from Sentinel-2 were explored to reveal their properties and potential problems related to dynamic mapping of vegetation changes.

Software tools for vegetation mapping based on calculation of the Normalized Difference Vegetation Index (NDVI) [[34]] were created and tested with two Sentinel-2 images of Riga taken on 28^{th} August, 2015 and on 10^{th} September, 2016.

NDVI is calculated using the formula:

$$NDVI = \frac{NIR - RED}{NIR + RED}$$

, where NIR is the image of the near infrared spectral band and RED is the image acquired in red visible light region. Calculations of NDVI for a given pixel always result in a number that ranges from minus one (-1) to plus one (+1); however, no green leaves gives a value close to zero. A zero means no vegetation and close to +1 (0.8 - 0.9) indicates the highest possible density of green leaves [`http://earthobservatory.nasa.gov`]. After calculating NDVI values for both images, a threshold was applied to replace image of multiple shades of gray with pseudo-color image. Pixel is marked red if its NDVI is less than 0.2, marked green, if NDVI exceeds 0.55, otherwise it is marked blue. The results are illustrated in Fig.4.3.6. We can see that vegetation levels have increased, as areas which were mostly colored blue in 2015's image are green in 2016's image. One of the explanations for this change is that in the hot summer of 2015 the grass was partially withered. To further analyze vegetation changes, a difference of NDVI's was calculated and displayed as another pseudo-color image (see Fig.4.3.7): pixel is marked black if both NDVI's are less than 0.2 (no vegetation in both images), marked green if NDVI is increased by more than 0.1, marked red if NDVI is decreased by more than 0.1, otherwise it is marked blue. Some areas that showed increased vegetation in thresholded NDVI are marked blue now indicating vegetation has no noticeable changes. Explanation is that vegetation increase is small (therefore unnoticeable in current image) but large

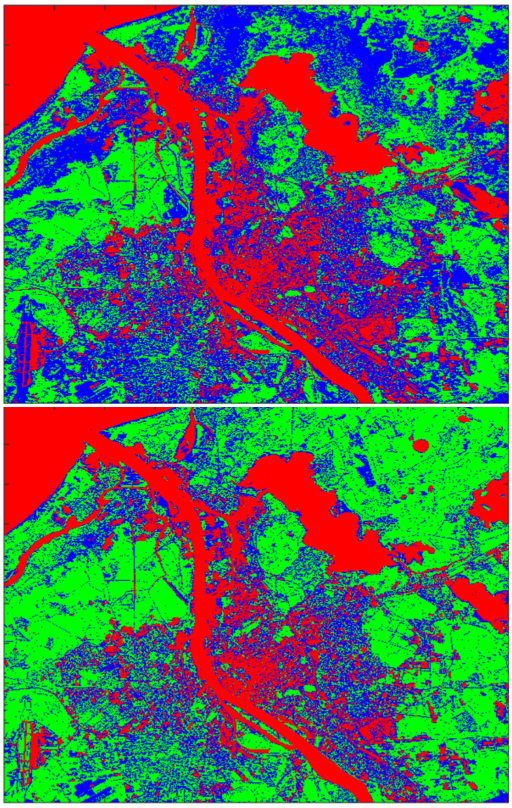

Figure 4.3.6: NDVI pseudo-color images of Riga.

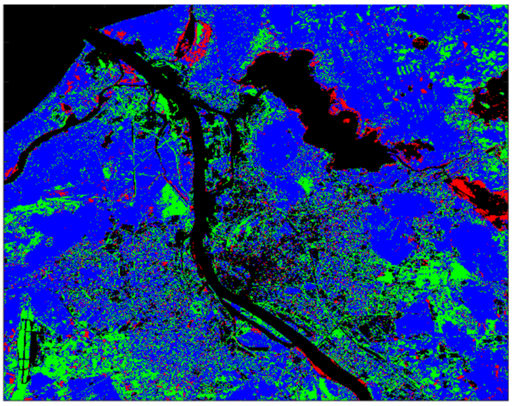

Figure 4.3.7: Vegetation difference

enough to cross NDVI threshold. The mapping of land use was based on the Bayes classifier that uses Gaussian distribution. The main problem here was acquiring ground truth data for deciduous trees and bushes (see Fig.4.3.8).

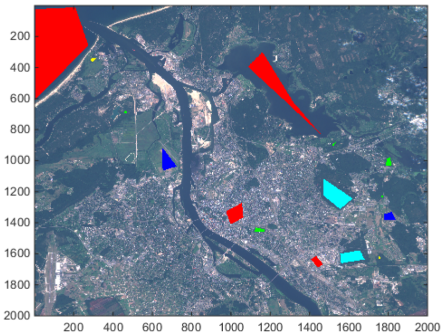

Figure 4.3.8: Ground truth samples.

Vegetation classification results are shown in Fig.4.3.9 and visualized in Fig.4.3.10. Deciduous trees are marked green, conifers - light blue, grasslands - dark blue, bushes - yellow and areas without vegetation are red.

As only ground truth areas were classified, accuracy is high but not really informative. More interesting is to compare classification results between both images presented in Fig.4.3.11. It is noticed that the same vegetation categories are obtained for approximately 80% of ground truth pixels. Further classification experiments with more ground truth data are planned to reveal error sources and increase classification stability between different time instances. Experiments with different other vegetation indexes are planned to analyze their application potential.

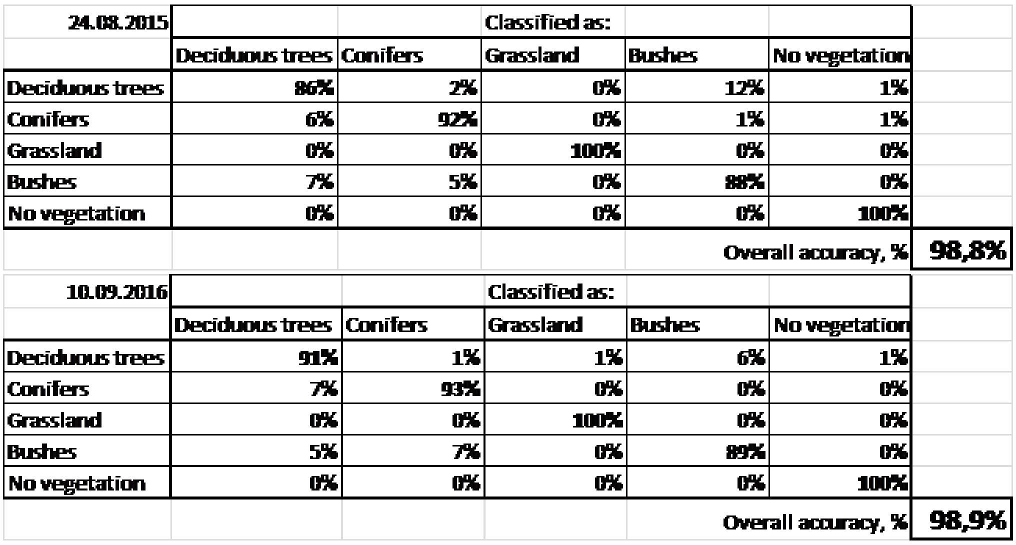

24.08.2015			Classified as:			
	Deciduous trees	Conifers	Grassland	Bushes	No vegetation	
Deciduous trees	86%	2%	0%	12%	1%	
Conifers	6%	92%	0%	1%	1%	
Grassland	0%	0%	100%	0%	0%	
Bushes	7%	5%	0%	88%	0%	
No vegetation	0%	0%	0%	0%	100%	
					Overall accuracy, %	98,8%

10.09.2016			Classified as:			
	Deciduous trees	Conifers	Grassland	Bushes	No vegetation	
Deciduous trees	91%	1%	1%	6%	1%	
Conifers	7%	93%	0%	0%	0%	
Grassland	0%	0%	100%	0%	0%	
Bushes	5%	7%	0%	89%	0%	
No vegetation	0%	0%	0%	0%	100%	
					Overall accuracy, %	98,9%

Figure 4.3.9: Vegetation classification accuracy.

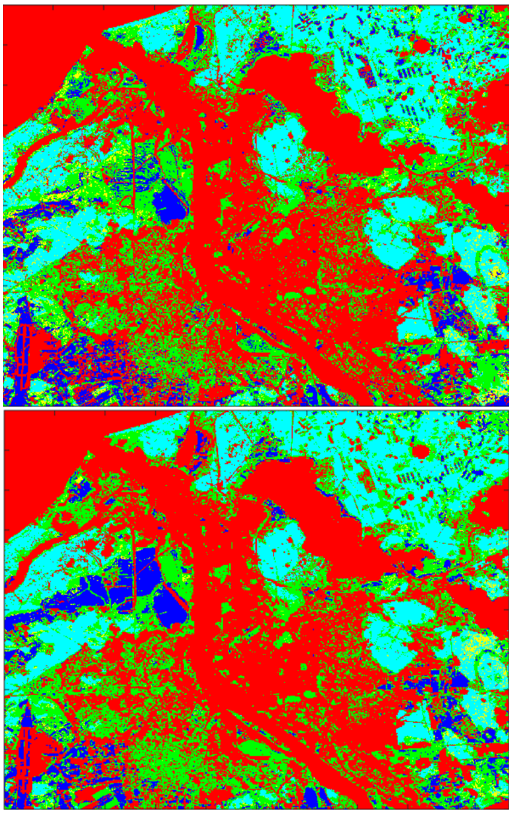

Figure 4.3.10: Vegetation classification results.

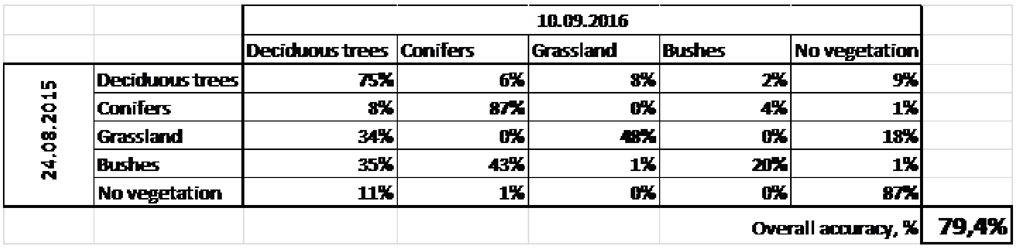

		10.09.2016				
		Deciduous trees	Conifers	Grassland	Bushes	No vegetation
24.08.2015	Deciduous trees	75%	6%	8%	2%	9%
	Conifers	8%	87%	0%	4%	1%
	Grassland	34%	0%	48%	0%	18%
	Bushes	35%	43%	1%	20%	1%
	No vegetation	11%	1%	0%	0%	87%
					Overall accuracy, %	79,4%

Figure 4.3.11: Classification accuracy between years 2015 and 2016.

4.3.3 Development of land surface elevation model from LiDAR data and software for simulation of flooding

To assist municipalities with information about potential flooding of their territories, LiDAR data can be used to develop land surface elevation models and software tools derived from them showing possible flooding areas when the water level exceeds certain limits. To deal with that in Riga and surrounding territories, LiDAR data (LAS files) collected by the Latvian Geospatial Information Agency (see `http://map.lgia.gov.lv/index.php?lang=2&cPath=4_5&txt_id=126`) were acquired. Average density of laser scans are 4 points per square meter and vertical accuracy is not worse than 12 cm with confidence level 95%. These data were used to develop ground elevation models with spatial resolution 1m using only data from last reflections of laser pulses.

The initial elevation model misses data for water basins as LiDAR fails to detect reflections from water. To facilitate simulations of water level and its rise, it is necessary to fill in these holes with real elevation data from the sea level. Fig.4.3.12 shows the elevation model created from LiDAR data with missing data represented by white color.

Three different types of "holes" were considered, namely 1)lakes, 2)rivers and 3)other. We define a lake as a water basin (object of connected pixels with missing elevation data) that is characterized by expected equal elevation above the sea level of all pixels. To fill in elevation data for lakes, the following procedure was proposed:

- interactively choose a point within the lake on the image;
- delineate a lake object around the chosen point and ask for confirmation. This step is needed to ensure that the lake object does not extend to connected rivers that fall into lake or flow out of it. If such happens, a tool for drawing a border between the lake and the river should be used;
- find the coast pixels closest to the lake using the morphological dilation of the binary lake object.
- collect elevation data from coast pixels;

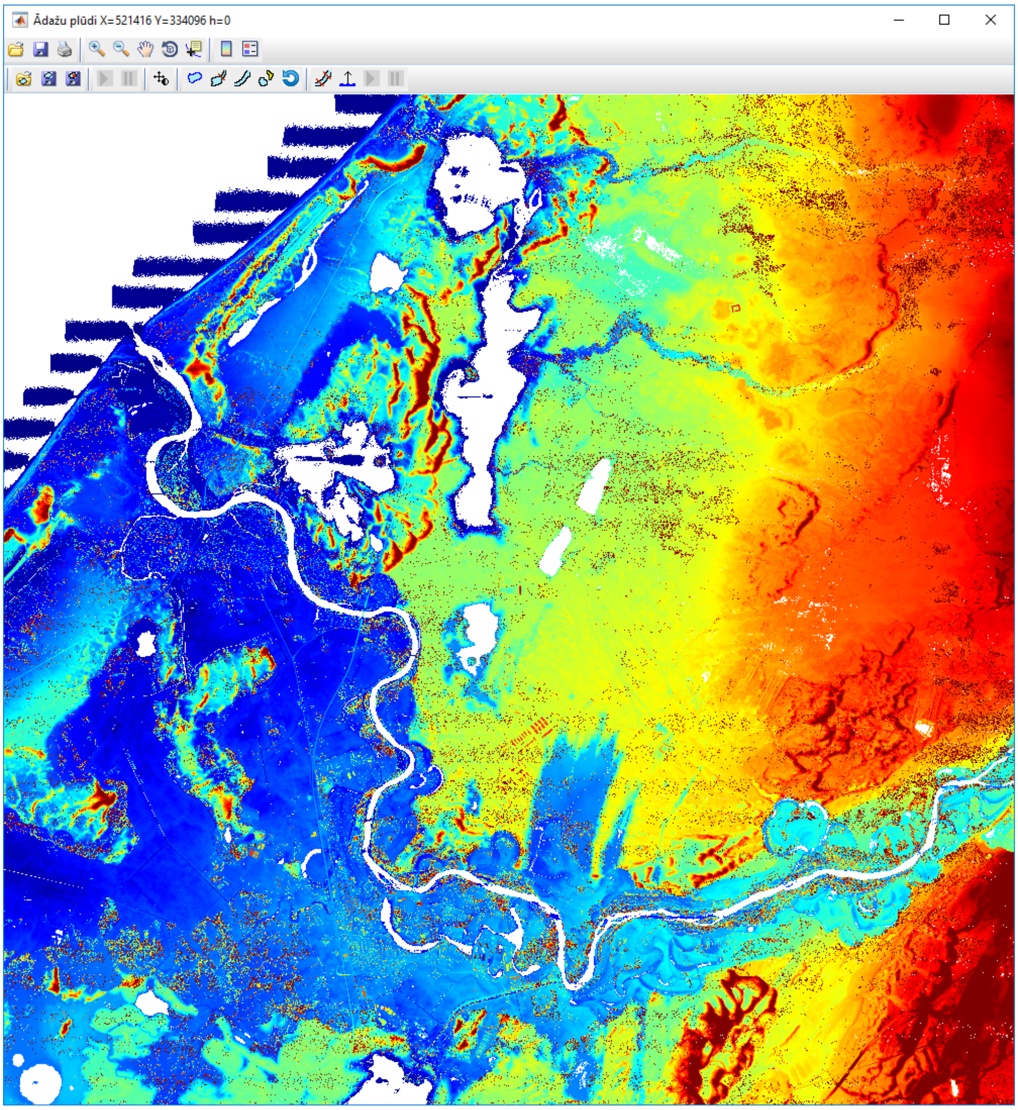

Figure 4.3.12: Elevation model of river Gauja region created from LiDAR data. Spatial resolution is 1m, elevation range from 0 to 20m.

- calculate elevation of the lake above the sea level and fill in the lake object with this number (equal for all lake pixels). Within this step, it is proposed to choose an elevation value of the lower coast pixels, dismissing 2 percent "outsiders".

More sophisticated procedure is needed to fill in river objects as the elevation of river pixels is different. We define a river as a water basin (object of connected pixels with missing elevation data) that is characterized by expected rising elevation above the sea level from pixels closer to the sea to pixels farther from the sea (distance calculated by the centerline of the river flow). To fill in elevation data for rivers, the following procedure was proposed:

- interactively draw a centerline of the river by selecting points within the river object on the image, starting from points closer to the sea;
- delineate a river object around the chosen points;
- assign maxRadius = 0;
- calculate elevation of each selected centerline point as follows:
  - draw a circle surrounding the centerline point that contains at least 1/4 pixels with elevation data available (coast pixels). To achieve that, iterate with a growing radius. If the radius used is greater than maxRadius, set new maxRadius value equal to the radius used;
  - calculate elevation of the centerline point above the sea level as the minimum height of the coast pixel included in the found circle;
- filter the elevation curve of centerline points using a median filter;
- ensure that elevation is not lowering from point to next point upper the river;
- form a detailed centerline with equal (10m) steps between the points;
- calculate elevation of each river pixel above the sea level as the height of the closest detailed centerline point. If the point is farther away from this centerline point than maxRadius*2, exclude that pixel from the river object (it possible relates to the influent river).

Information about the river objects defined by the procedure above should be saved for later use within the flooding simulation.

"Other" objects are filled in after lakes and rivers by applying the algorithm used for the lakes automatically.

Fragment of the image after filling all objects is shown in Fig.4.3.13.

When the river elevation data are filled in, simulation of flooding due to the rise of the water level in the river was implemented in the program. In real flooding situations, changes of the water level in different places in the river are not equal. Water level forecasts for flooding situations were obtained from Adazi municipality and introduced into the program. Simulations of flooding then can be performed by raising water levels proportionally with respect to the flooding forecast. Alternatively, simulation where all river pixels are rising with the same increment as the pixel for what the rise is simulated can be done (that is a serious simplification, of course, and should be used for the local fragment of the river if no forecast is available for it).

Adazi municipality pays a lot of attention to potential flooding problems and is currently started development of a new dam to protect the area. It was therefore feasible to implement software functions for introduction of a virtual dam into the elevation model. Another issue was related to forest areas. If there are insufficient number of reflections from the ground in these areas, flooding

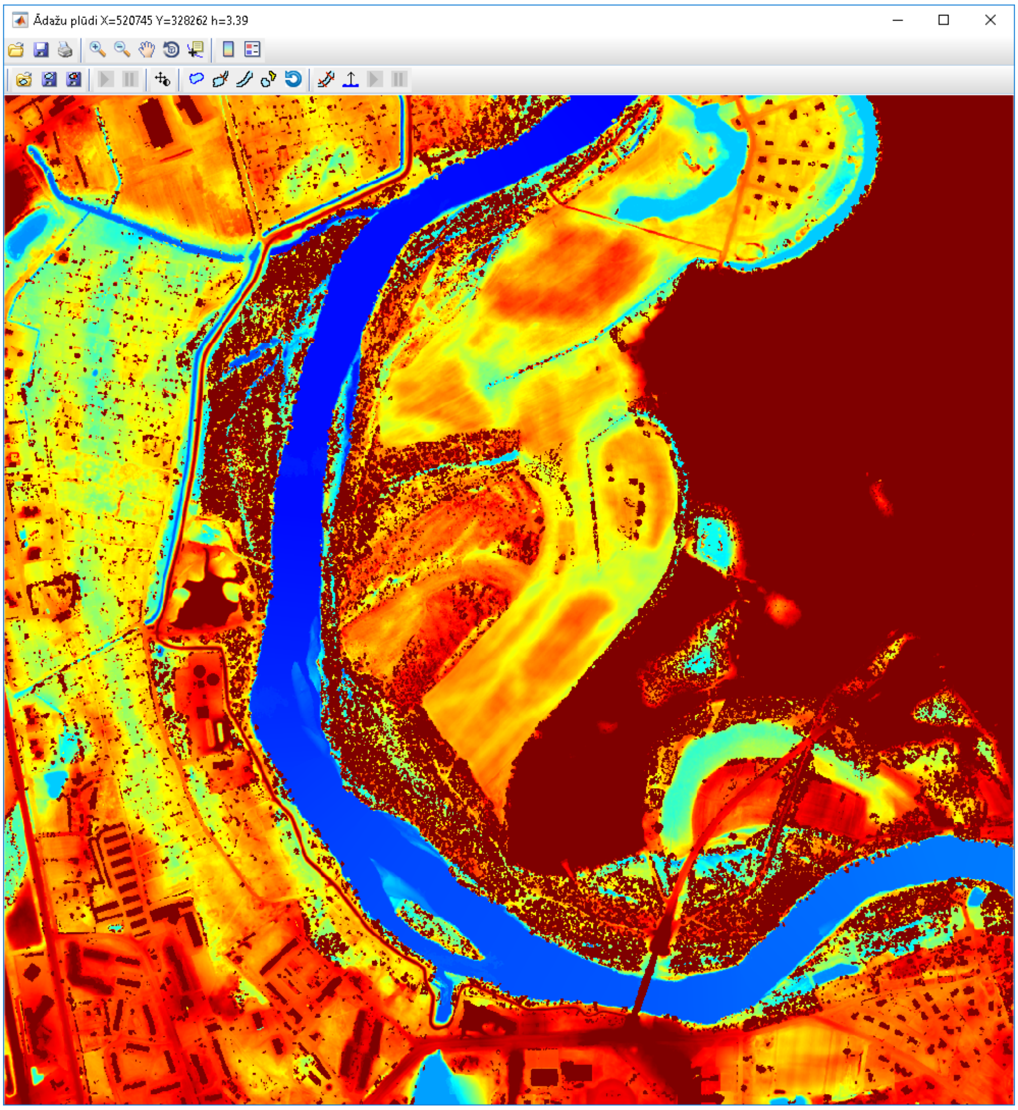

Figure 4.3.13: Elevation model of a fragment of river Gauja near the bridge from Adazi to Kadaga after filling all water objects, elevation range from 0 to 6m. An existing dam to the left of the river is noticed.

of the forest areas cannot be simulated. Therefore the tool for filtering of the selected forest areas was implemented.

Simulation of flooding in Adazi area (57.08° N, 24.33° E) was implemented using the following algorithm:

- interactively choose a ”measurement” point on the river the rise of which will be simulated;
- input a new elevation of the chosen point and calculate the increment in respect to the original value;

- form a new elevation model of the flooded river by raising the elevation of each river pixel (taking into account the flooding forecast or by the same amount as the ”measurement” pixel);
- iterate to simulate flooding of nearest coast pixels:
    - find the current unflooded coast pixels using the morphological dilation of the current binary river object;
    - add coast pixels to the flooded river object if they feature lower elevation than the neighboring water pixels and set their elevation values to that of the higher neighboring water pixels;
    - visualize the new instance of the flooding river;
    - finish iterations if no new flooding river pixels are detected.

The program ”AdazuPludi” was developed as a result of these activities, described in `http://www.edi.lv/media/uploads/UserFiles/Gudpils-RemSens-pludi.pdf` (in Latvian). It was demonstrated and installed in Adazi municipality to assist in flooding simulation and provide informational services to inhabitants.

The main functions of the ”AdazuPludi” application are as follows:

- file operations with elevation models;
- vizualization of elevation models with pseudo-colors in different elevation ranges with zoom and pan;
- filtering out tree canopies in selected forest areas;
- viewing elevation profiles and 3D plots of selected areas;
- interactive filling of water areas;
- introduction of dams and culverts;
- simulation of flooding due to raise of a water level in river.

Sample simulation results of flooding in the Adazi area are presented in Fig.4.3.14

4.3.4 Summary

The following main results of the REMSENS group should be emphasized:

- theoretical studies in remote sensing data processing have provided the following new methods applicable to land use/ land cover classification in smart cities:

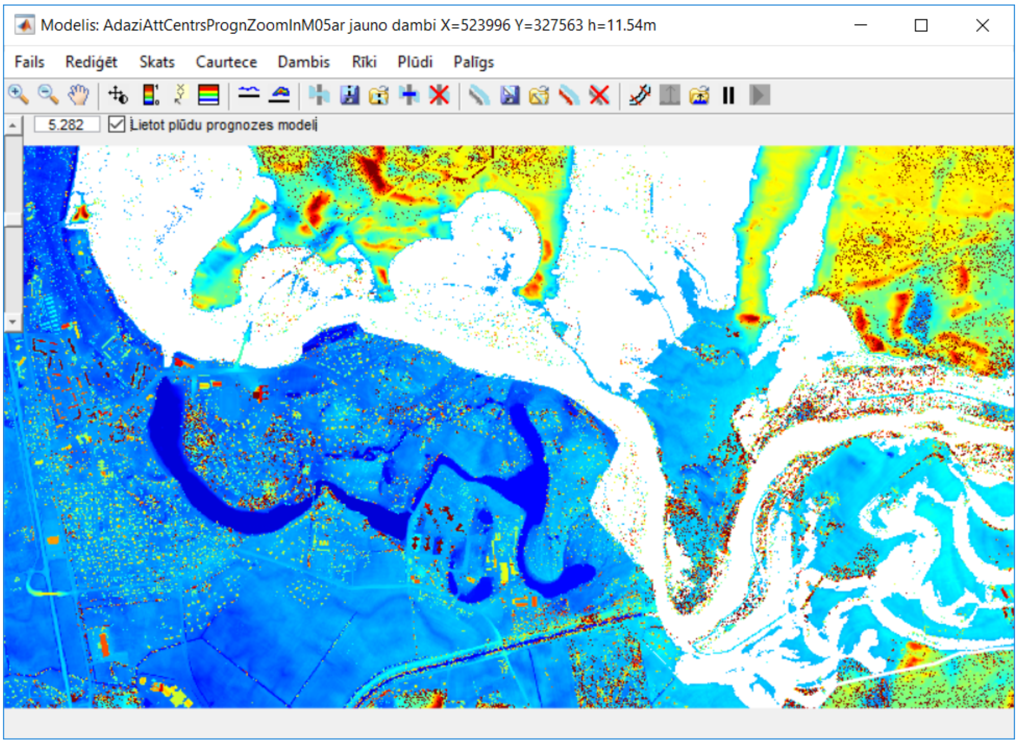

Modelis: AdaziAttCentrsPrognZoomInM05ar jauno dambi X=523996 Y=327563 h=11.54m

5.282 ☑ Lietot plūdu prognozes modeli

Figure 4.3.14: Flooding simulation result of river Gauja near the bridge from Adazi to Kadaga, elevation range from 0 to 20m. A dam under construction is introduced into the model. Rise of the water level near the bridge to Kadaga to 5.28m is simulated. Potential water levels from the flooding forecast with 1% probability (each 100 years) are taken into account.

- the method for classification of data from different sources with different spatial resolution. It allows to perform fusion of sensor data within the Bayesian classifier and to combine several distributions in the design of the classifier. Obtained results have shown that it is possible to improve classification accuracy if the data fusion was used in the proposed way. In addition, classification accuracy was slightly improved when several distributions were combined in the design of the classifier;
- two methods for selection of informative spectral bands for classification of hyperspectral images. Informativeness of spectral bands were considered on the basis of entropy of the band's image but correlation between images of spectral bands was used to avoid redundancy in the set of selected ones. Informativeness of the whole set of selected bands was characterized by classification results of hyperspectral images using only data from bands included in the set. It was shown that one of the proposed methods provides for higher classification accuracy than methods known in scientific literature;

    - the approach based on fuzzy logic was proposed for classification of mixed pixels in satellite images. It was shown that this approach is promising as it allows to clean the training sets of supervised classifiers;

- problems faced when the vegetation mapping for smart cities from satellite images is to be implemented were assessed and practical tools for solving this task were developed;

- elevation models with high spatial resolution and precision were developed from LiDAR data and software allowing to simulate flooding situations on the basis of such models developed. This software was approbated in Adazi municipality and found useful for planning of new dams and providing informational services to inhabitants of the areas.

Results of the EDI REMSENS team are summarized in 3 scientific papers, 1 doctoral thesis, 1 master thesis; 1 software package was developed and approbated in external organization. Accumulated knowledge and experience of the team resulted in starting the European Space Agency project "Dynamic land use monitoring by fusion of satellite data" (DynLand, see `http://www.edi.lv/en/projects/esa-projects/dynland/`).

Chapter 4.4

EDI RADAR group: Development of the ultra-wideband (UWB) radar technology and UWB-based systems for security monitoring

This Chapter describes project results of the EDI RADAR group. Activities from periods 1, 2 and 3 are summarized briefly, starting with the introduction to the UWB radar technology. UWB radar development and test measurements performed during the period 4 (year 2017) are described in more detail. List of group's activities during the project period 4 is as follows:

1. Development of Ultra-wideband radar sensors and evaluation of their applications for urban security monitoring
   (a) UWB radar sensor development for human movement tracking
   (b) UWB pulse based technology development for human counting
2. Development of technological prognosis for application of ultra-wideband radar sensors in smart cities

4.4.1 Introduction of ultra-wideband technology

Lower microwave band electromagnetic waves (below 10GHz) can be used in ultra-wideband sensors. Those waves penetrate well into most materials (except metals). Due to the large bandwidth, electromagnetic waves used in the sensors provide high resolution and excellent accuracy in remote measurements. The technology can be used in non-contact, mobile, non-invasive and non-destructive security systems, for obtaining images of objects behind walls, buried in ground and in low visibility conditions (darkness, fog, rain, etc.). One UWB radar sensor can be used to measure distance to an object that reflects the transmitted pulse; using two sensors, an object image in the 2D plane can be formed, but three appropriately placed sensors provide for forming a three-dimensional object image. Observing a fixed position radar image from one and the same area but in different time moments, small changes in the room can be detected, like shifted furniture, displacement or absence of mobile phone and other devices or equipment. This approach can be used in room security systems.

The radar sensor principle relies on sounding a scenario under test using radio waves in the GHz range and process the obtained echo signal (Fig. 4.4.1) .

The radar echo depends on target size, shape and material composition and from the test room configuration. From the obtained echo signal the desired information: distance, location, orientation, speed, shape, material composition can be calculated using signal processing methods and algorithms using some *a priori* knowledge about the scenario under test (system model, material parameters, etc.).

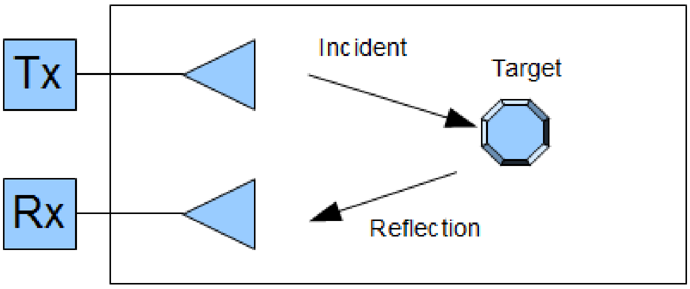

Figure 4.4.1: Fundamental impulse radar principle.

4.4.1.1 Theoretical UWB radar object resolution

1. Range resolution (δ_r) [35] is the ability to of the radar sensor to distinguish between two closely located point targets of identical radar cross section

$$\delta_r \approx \frac{t_w c}{2} \approx \frac{c}{2BW}, \tag{4.4.1}$$

   where t_w - transmitted pulse width (envelope width), c - the speed of light, BW - bandwidth of the transmitted pulse.

2. Range accuracy (δ_A) [35] is the minimum range error for a single point target that can be attained in case of noise-affected measurements.

$$\delta_A = \frac{c\varphi_j}{2} = \frac{ct_r}{2\sqrt{SNR}} \approx \frac{c}{4BW\sqrt{SNR}}, \tag{4.4.2}$$

   where c - the speed of light, $varphi_j$ - standard deviation of the temporal position of the envelope edges of the receive signal, t_r - rise time of the envelope, SNR - signal-to-noise ratio, BW - bandwidth of the transmitted pulse.

For example, a UWB radar sensor device, working in the 3GHz to 5GHz frequency range and using a 2 GHz bandwidth and having an Signal to noise ratio SNR = 100 (40 dB), could have a approximate range resolution of $\delta_r = 7.5cm$ and a range accuracy $\delta_A = 0.75cm$. Of course, these are just approximate numbers because they do not take into account the physical parameters of the environment where the device is working (wave propagation speed, radio wave absorption, wave diffraction, reflections, near field effects, etc.).

4.4.2 UWB security applications

Modern society in a smart city should use information and data from all sensors (building security sensors, street monitoring cameras/sensors and others) to increase efficiency of infrastructure like traffic light optimization using traffic data or pavement and building pathway design choices based on people walking habits.

UWB pulse radar properties, namely high resolution, low output pulse power and high energy efficiency can effectively be used for short range security sensor applications, ranging from simple movement detection to human trajectory mapping from hidden sensors with a possibility of replacing other sensors (PIR, ultrasonic) for added information benefits in smart city. Pulse propagation properties of UWB radars can be used for other security applications e.g. to remotely monitor breathing of patients in hospitals or to measure ice thickness in a simple and convenient way.

4.4.2.1 Ice thickness measurement

The UWB radar sensor can be used for non-metallic material thickness testing. For water safety monitoring, remote ice thickness measurements could be useful. To test UWB radar sensor ice thickness measurement capabilities an indoor test setup was made (Fig. 4.4.2). Using the measurement test setup, it can be seen that the acquired signal contains three components: 1) the direct pulse; 2) reflection from air/ice boundary; 3) reflection from ice/floor boundary.

Experimental measurements using different thickness ice cubes were performed (Fig. 4.4.3). From the 5 cm and 17 cm thick ice cube measurement signals it can be seen, that: 1) the sounding impulse is too long to correctly measure ice thickness below 10cm; 2) the long antenna ringing makes the peak detection more difficult on larger ice thickness measurements.

After measuring the travel time t in the ice layer from the reflected impulse peaks and prior knowledge of the material dielectric constant (ε), the ice thickness could be calculated using a simplified equation:

$$x = \frac{c}{2 \cdot \sqrt{\varepsilon}} \cdot t \tag{4.4.3}$$

.

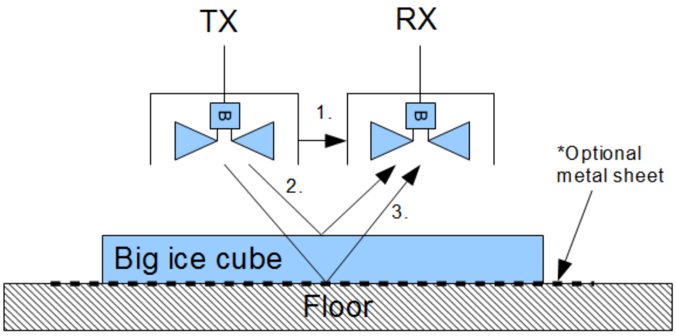

Figure 4.4.2: Indoor ice thickness measurement test setup.

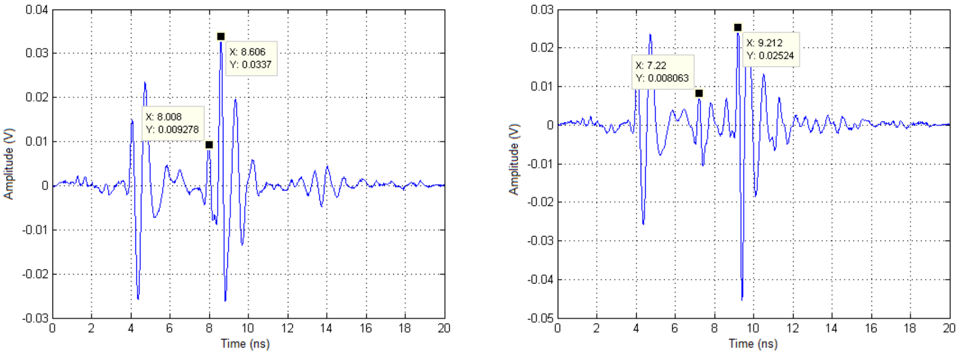

(a) 5cm thick ice cube

(b) 17cm thick ice cube

Figure 4.4.3: Indoor ice thickness measurement results.

The opposite calculation of the material's dielectric constant can be done by expressing the dielectric constant from the equation 4.4.3, the result is equation 4.4.4:

$$\varepsilon = \left(\frac{c \cdot t}{2 \cdot x}\right)^2 \tag{4.4.4}$$

.

The results from three different ice block thickness measurements are summarized in Table 4.4.1. These experimental measurements were made as a part of student's bachelor thesis [36].

Table 4.4.1: Ice thickness measurement results.

Ice thickness	Time between impulse peaks, $[ns]$	Calculated ε	Calculated ice thickness using $\varepsilon = 3.1$	Error, %
5 cm	0.598	3.2184	5.095 cm	1.9
11 cm	1.286	3.0752	10.956 cm	0.4
17 cm	1.992	3.0893	16.971 cm	0.2

Ice thickness measurements were also tested in real life environment on lake Jugla. To get thickness measurements in constant steps (10 cm), the radar was supplemented with a distance encoder wheel. Each radar signal trace sample value was converted to the equivalent grayscale pixel intensity to get a visual illustration of the ice structure (fig. 4.4.4).

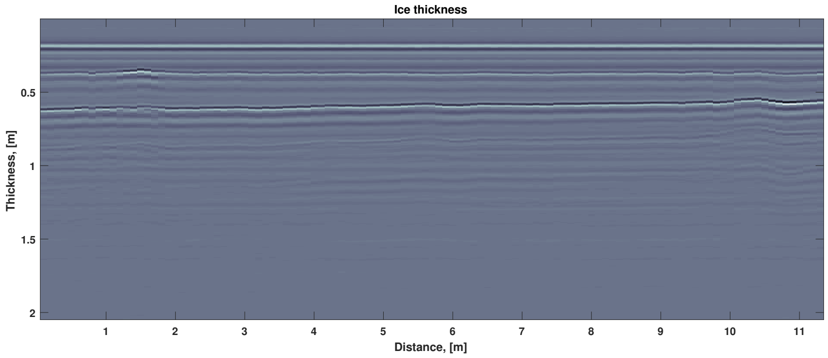

Figure 4.4.4: Outdoor ice thickness measurements from lake Jugla.

From each signal trace, ice thickness could be calculated using the same equation 4.4.3. Measurements were performed in 10 cm steps over a distance of ≈11 m. Result is visualized in Fig. 4.4.5.

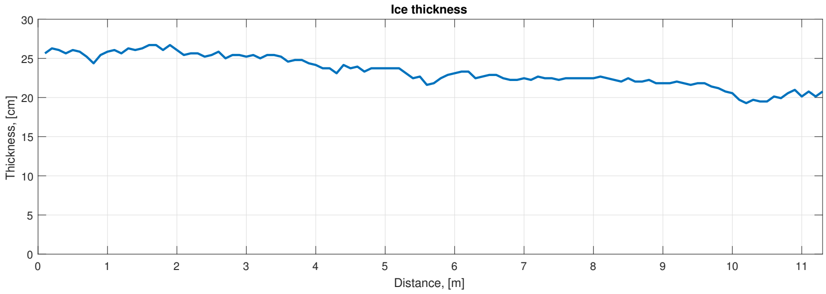

Figure 4.4.5: Calculated ice thickness on lake Jugla.

4.4.2.2 Building material structure inspection

To illustrate application of UWB radars for urban security and protection, it was decided to inspect the structure of concrete and measure its moisture level in a non-destructive manner using UWB radar technology. To achieve this goal, several tasks were fulfilled: analysis of impulse radar sensors; antenna tests; building bulkhead analysis and experimental signal processing.

To measure the moisture level of a construction, the dielectric permittivity has to be measured. In order to do that, the travel time of a signal in any given medium has to be measured and from this, the dielectric permittivity can be calculated using Eq. 4.4.5.

$$\varepsilon = \left(\frac{c \cdot t}{2 \cdot x}\right)^2 \tag{4.4.5}$$

, where ε is the dielectric permittivity, c is the speed of light in vacuum, t is signal propagation time in medium, x is medium thickness.

The test setup consisted of a concrete wall with thickness 12.5 cm, where radar was positioned 50cm from the wall (Fig. 4.4.6). Planar bow-tie antennas were used for the test. A-scan data were acquired (Fig. 4.4.7a). Afterwards it was possible to collect B-scan data throughout the length of the wall (Fig. 4.4.7b).

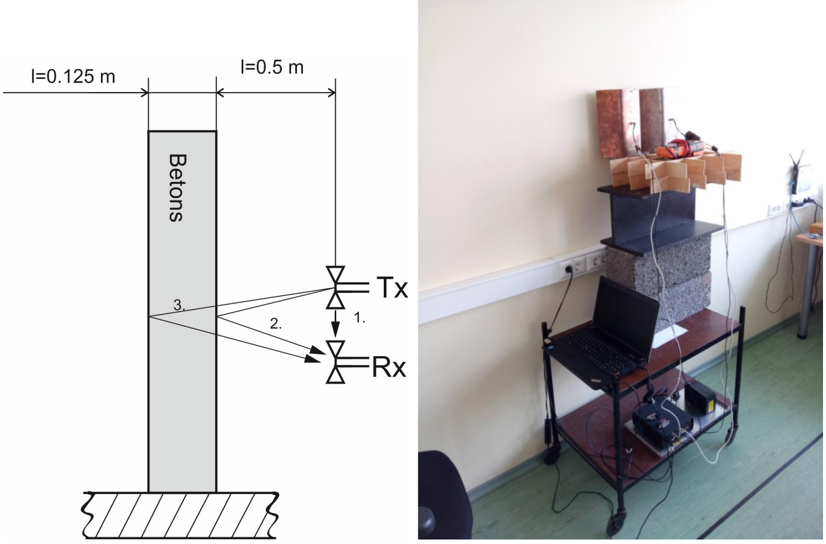

(a) Test setup (b) Experiment

Figure 4.4.6: Concrete wall test set up and experiment

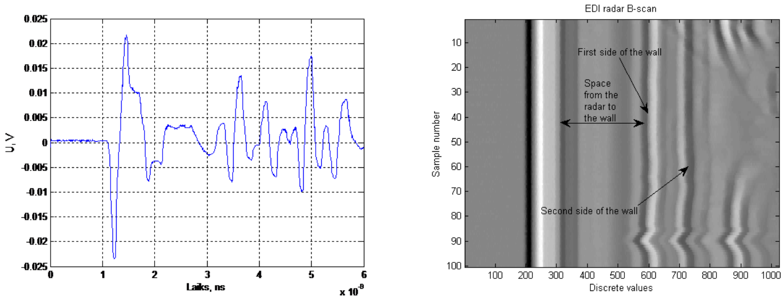

(a) A-scan (b) B-scan

Figure 4.4.7: Experimental EDI radar prototype

The concrete wall as an experimental object behaved as planned. Knowing its thickness, we could calculate the travel time of the signal and then calculate the dielectric permittivity.

4.4.2.3 Remote life-sign detection

A prototype device for life-sign detection was presented at *Invention and Innovation Exhibition MINOX 2016*. The exhibition took place at the Riga Technical University, from 7th to 8th of October, 2016. The exhibition was organized as the main event of Latvian Inventors Day with the aim of promoting inventiveness in the society, and fostering the commercialization of inventions.

UWB radar sensor presented was used to send short, low energy electromagnetic pulses into the medium (in this case human chest) and receive reflected signals. By processing the reflected signal, it is possible to estimate both the environmental parameters and their changes. If any motion occurs within the operation area of the device e.g., cardiac, respiratory or other human movement, then the reflected signal varies and this can be detected by the highly sensitive receiver developed. Using original digital signal processing methods, it is possible to separate signals related to cardiac and respiratory movements.

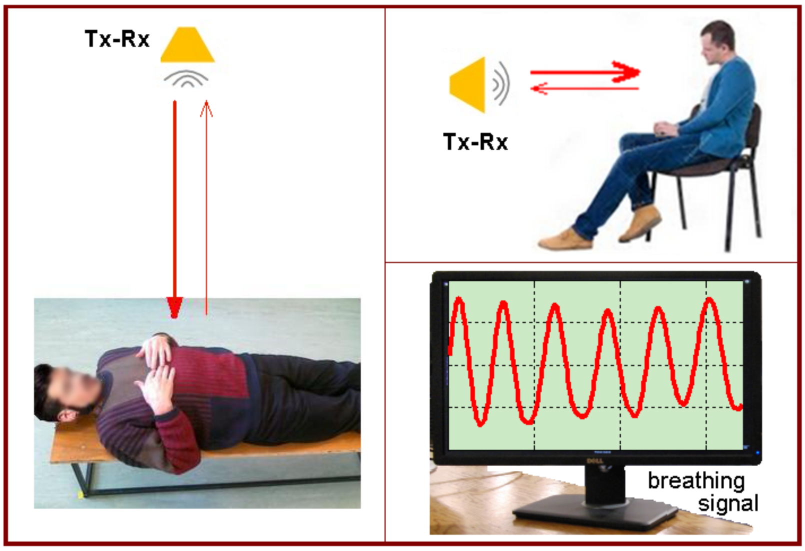

Figure 4.4.8: Remote life-sign detection system

The device serves for the remote detection of human life-signs (breathing, heartbeat, movement). The life-signs can be detected behind walls and other non-metallic obstacles as well. The presented device can be used for:

- medical purposes, e.g., in hospitals to remotely monitor the patients or infants respiratory rate during sleep,
- security purposes, e.g., for detecting living persons or beings in the room or behind the wall,
- rescue operations, e.g., searching for people in the rubble that are showing signs of life,
- research work, e.g., for animal activity monitoring.

Human chest excursion in radar data provides very small signal deviation that is why research on detection of small moving target (object) in ultra-wide band pulse radar sensors systems was carried out. The research aim was to investigate methods of small object movement detection that are masked by large signal reflections from other objects in the area covered by the radar sensor. Karhunen Loeve transform was used to filter out small object movements from the reflected radar sensor signals. The method was tested on synthesized signals and on signal obtained from experiments. The research results were published in a scientific journal paper: *Aristov V. (2016) Karhunen Loeve transform as a tool to eliminate signal's redundancy, when small targets detection. Sciences of Europe. Vol 2, No 2 , 53-57.* Journal link [PDF,RU].

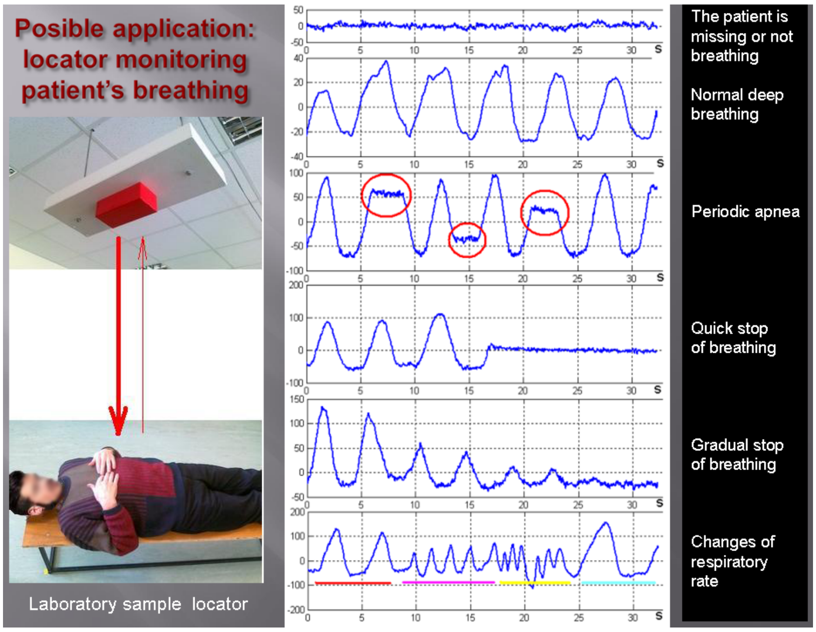

Figure 4.4.9: Example of acquired breathing patterns from processed data

An example of obtained results can be seen in Fig. 4.4.9. The reflected signal is small and masked by strong reflections from the surroundings. Results in Fig. 4.4.9 are acquired after signal processing.

4.4.2.4 Object detection, counting and tracking

An object can be detected by using only one transmitter (Tx) and receiver (Rx). If the antennas are placed at fixed positions and the background signal $u(t)$, which is composed of a direct pulse (coming from Tx to Rx) and reflected pulses from the walls and other static objects, is recorded, then reflected pulses from any nearby object, which was not present at the time when $u(t)$ was recorded, can be distinguished from $u(t)$ and therefore the object can be detected.

Object counting

The ability of sensing (detecting) objects can be used for counting the number of persons entering or leaving the building or passing particular small areas under inspection. For example, if the antennas are placed at the corridor ceiling, then the recorded signals, when one person crosses the area under antennas, are shown in Fig. 4.4.10(a).

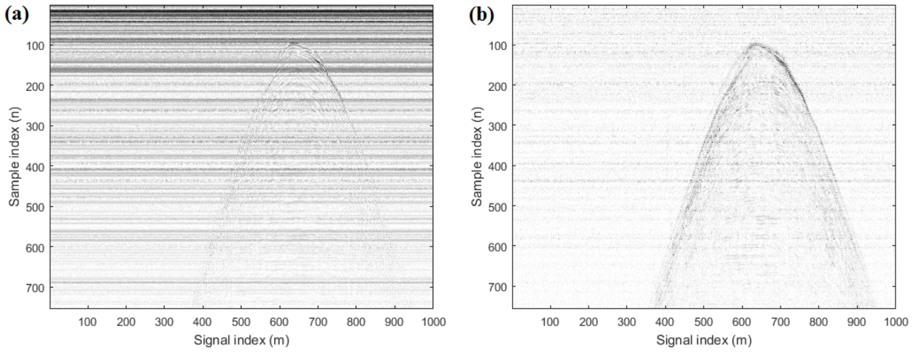

Figure 4.4.10: Recorded signals at Rx during one person passing the antennas along the corridor: (a) raw signals $s_m(t) = u(t) + x_m(t)$; (b) the time-varying part $x_m(t)$ of $s_m(t)$

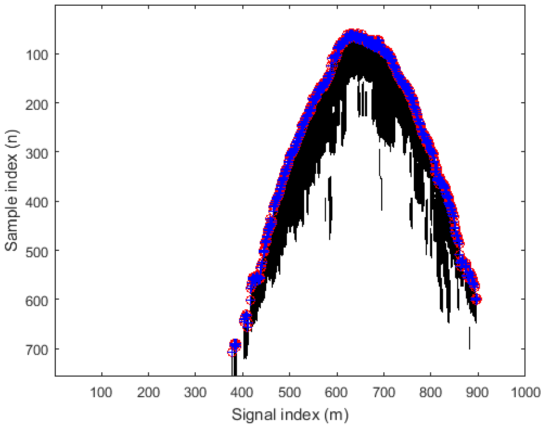

Figure 4.4.11: The obtained trace $y(m)$ (blue line) corresponding to the person first approaching and then leaving the area under the antennas

The received signals $s_m(t)$ in Fig. 4.4.10(a) can be written as $s_m(t) = u(t) + x_m(t)$, where $u(t)$ is the non-varying background signal, while $x_m(t)$ are composed of reflected pulses from the person. By subtracting $u(t)$ from $s_m(t)$, only time-varying part $x_m(t)$ remains and becomes clearly visible, as shown in Fig. 4.4.10(b). After low-pass filtering and thresholding the data, the trace $y(m)$

can be obtained, as shown in Fig. 4.4.11, from which a decision of the person passing the area can be made.

Object tracking: simulation model

A task of the simulation model is to generate UWB signals which are received by multiple UWB receivers Rx_n, $n = 1, 2, \ldots$, located at coordinates (x_{R_n}, y_{R_n}) after being radiated by one UWB transmitter Tx at (x_T, y_T) and reflected from multiple objects O_m, $m = 1, 2, \ldots$, located at (x_{O_m}, y_{O_m}). An example of one Tx, one Rx and two objects is shown in Fig. 4.4.12.

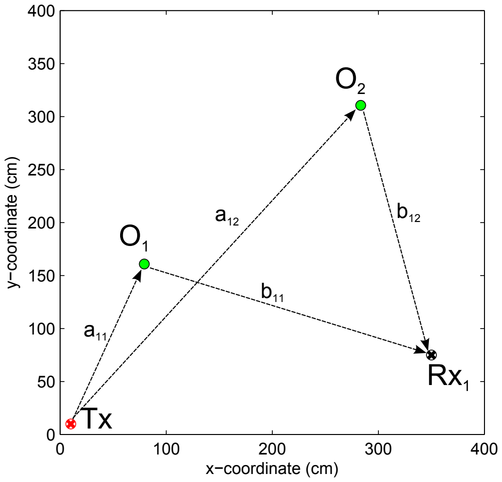

Figure 4.4.12: A model consisting of one transmitter Tx, one receiver Rx_1 and two objects O_1 and O_2, which reflect the UWB signals radiated by Tx and received by Rx_1

By assuming that UWB pulse is radiated at $t_0 = 0$ and with c denoting the speed of light in vacuum, reflected pulses from the objects O_1 and O_2 reach the receiver at $t_{11} = (a_{11} + b_{11})/c = L_{11}/c$ and $t_{12} = (a_{12} + b_{12})/c = L_{12}/c$, respectively. In addition, a background signal $u(t)$, which is composed of a direct pulse (coming from Tx to Rx_1) and reflected pulses from the walls and other static objects, reaches Rx_1 as well. However, since $u(t)$ is known and can be obtained when O_1 and O_2 are not present, the background signal can be excluded from the expression of the received signal, which can therefore be written as:

$$s_{R_1}(t) = A_{11}g(t - t_{11}) + A_{12}g(t - t_{12}), \tag{4.4.6}$$

where $g(t)$ is the UWB pulse located at $t_0 = 0$ and A_{11}, A_{12} are the amplitudes of the pulses depending on the distances L_{11} and L_{12}. An example of $s_{R_1}(t)$, when $g(t)$ is the derivative of a Gaussian pulse, is shown in Fig. 4.4.13.

In general, given M objects, the received signal by Rx_n can be calculated as:

$$s_{R_n}(t) = \sum_{m=1}^{M} A_{nm}g(t - t_{nm}), \tag{4.4.7}$$

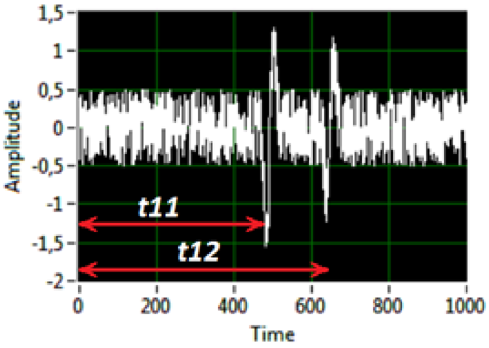

Figure 4.4.13: The signal $s_{R_1}(t)$ at Rx_1 after subtracting the background signal $u(t)$ (white Gaussian noise is also added to $s_{R_1}(t)$).

where

$$t_{nm} = \frac{1}{c}\left(\sqrt{(x_T - x_{O_m})^2 + (y_T - y_{O_m})^2} + \sqrt{(x_{R_n} - x_{O_m})^2 + (y_{R_n} - y_{O_m})^2}\right). \tag{4.4.8}$$

In real world applications, given the received signals and the coordinates of the transmitters and receivers, the task is to find locations of the objects. Similarly, given the simulated signal $s_R(t)$, which depends on the coordinates of Tx, Rx and objects, and is calculated according to (4.4.7), the task is to find the locations of the objects assuming that coordinates of Tx and Rx are given.

Let us consider the case, where only one receiver and two objects, as shown in Fig. 4.4.12, are present. By finding the locations of the reflected pulses (Fig. 4.4.13), the distances of the paths Tx-O_m-Rx_1, $m = 1, 2$, are calculated:

$$L_{1m} = ct_{1m}. \tag{4.4.9}$$

Next, given a distance l_1 from Tx to Rx_1:

$$l_1 = \sqrt{(x_T - x_{R_1})^2 + (y_T - y_{R_1})^2}, \tag{4.4.10}$$

and a coordinate (x_{m1}, y_{m1}) of its midpoint:

$$x_{m1} = (x_T + x_{R_1})/2, \quad y_{m1} = (y_T + y_{R_1})/2, \tag{4.4.11}$$

the expressions of ellipses for each object are obtained:

$$\begin{cases} x = 0.5L_{1m}\cos\alpha\cos\beta - 0.5\sqrt{L_{1m}^2 - l_1^2}\sin\alpha\sin\beta + x_{m1} \\ y = 0.5L_{1m}\cos\alpha\sin\beta + 0.5\sqrt{L_{1m}^2 - l_1^2}\sin\alpha\cos\beta + y_{m1}, \end{cases} \tag{4.4.12}$$

where $\alpha \in [0, 2\pi]$ and

$$\beta = \arctan\left(\frac{y_{R_1} - y_T}{x_{R_1} - x_T}\right). \tag{4.4.13}$$

The ellipses with their two focal points (foci) located at Tx and Rx_1 are shown in Fig. 4.4.14.

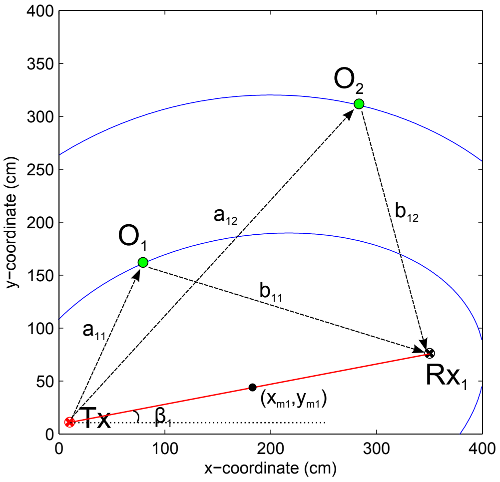

Figure 4.4.14: Two ellipses, which are drawn according to (4.4.12) depending on the coordinates of Tx and Rx_1 and the measured distances $L_{11} = a_{11} + b_{11}$ and $L_{12} = a_{12} + b_{12}$.

Any point on the ellipse can potentially be a location of the object since the sum of the distances from the point to the two foci of the ellipse is constant and equal to the measured distance. Therefore, at least two more receivers must be added in order to find the coordinates of the objects at the crossings of the three ellipses. This is shown in Fig. 4.4.15, where the third receiver Rx_3 is placed at the same location as Tx.

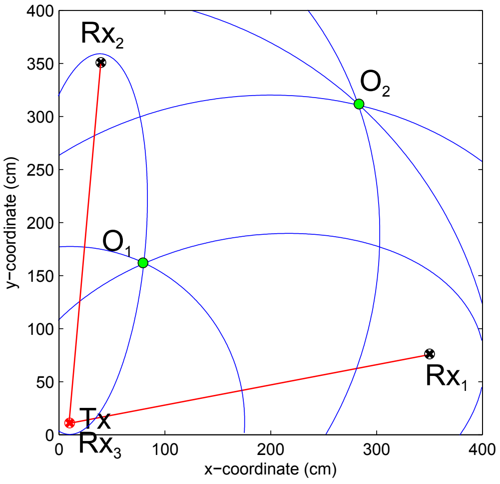

Figure 4.4.15: Drawing of the ellipses determined by the coordinates of Tx and Rx_n, $n = 1, 2, 3$, and the received signals by Rx_n containing the reflected pulses from the objects – the crossings of at least three ellipses correspond to the locations of the objects

After obtaining the equations of all the ellipses which follow from the measured delays of the reflected pulses in the received signals $s_{R_n}(t)$, the task is to find the intersection points of at least three ellipses, which are then assumed to be the positions of the objects.

One way of finding the crossing points of the obtained ellipses (4.4.12) is to solve the systems of such equations analytically, however, a more simple solution is achieved by converting an XY graph of each ellipse into a binary image as shown in Fig. 4.4.16 with white color pixels representing the line of the ellipse (on the left side pixels of size 2 × 2 cm are used, while on the right side pixels of size 8 × 8 cm are used).

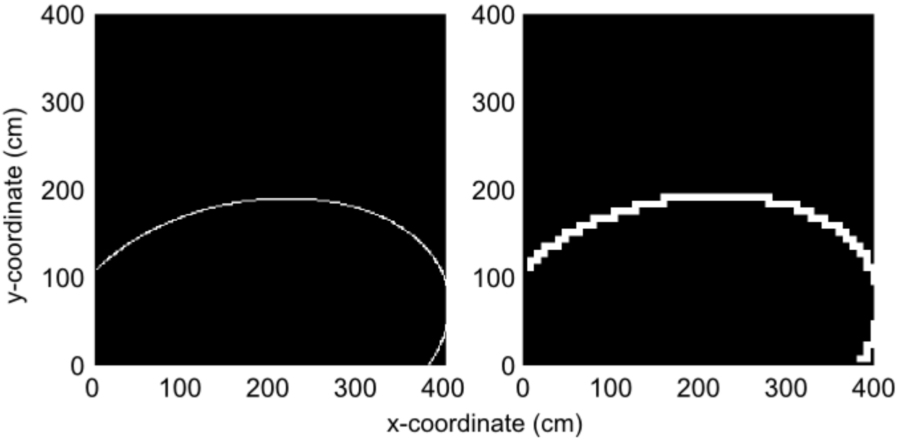

Figure 4.4.16: Binary images of the ellipse – pixels of size 2 × 2 cm and 8 × 8 cm are used on the left and on the right sides respectively.

After obtaining the binary images of all ellipses, the interception points are found by applying a logical AND operation between the images. Also, the influence of the noise, which is present in the received signals, can be reduced on the outcome of the results by varying the size of the pixels.

Object tracking: experimental results

In UWB system for object tracking one transmitter, located at coordinates (x_T, y_T), radiates UWB pulses, which after reflecting from objects O_m, $m = 1, 2, \ldots$, located at (x_{O_m}, y_{O_m}), are received by multiple UWB receivers Rx$_n$, $n = 1, 2, \ldots$, located at coordinates (x_{R_n}, y_{R_n}). A task of the signal processing is to find the coordinates of the objects given the signals $s_{R_n}(t)$ at the receivers (Fig. 4.4.17).

In order to calculate the positions of the objects, the following steps are performed.

1. The time instants t_{mn} of the received reflected UWB pulses are found and the corresponding distances Tx-O_m-Rx_n are calculated as $L_{mn} = (t_{mn} - t_0)c$, where t_0 is the time instant when pulses are radiated and c is the speed of light in vacuum.

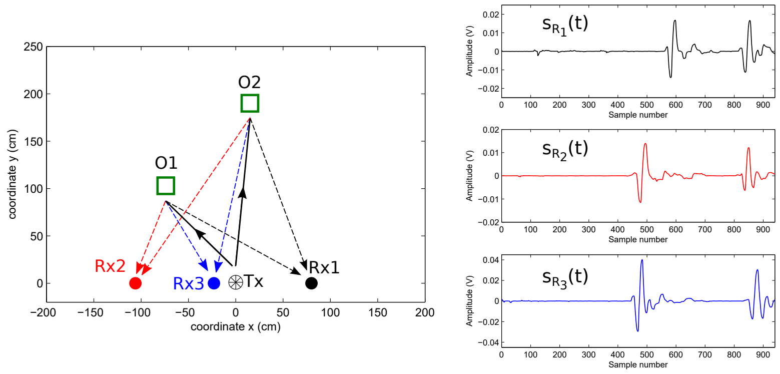

Figure 4.4.17: Paths of UWB pulses after being radiated by UWB transmitter Tx – the pulses are reflected from objects O_1 and O_2 and received by UWB receivers Rx_1, Rx_2 and Rx_3 producing the signals $s_{R_1}(t)$, $s_{R_2}(t)$ and $s_{R_3}(t)$, respectively (a background signal, which is composed of a direct pulse (coming from Tx to Rx$_n$) and reflected pulses from the walls and other static objects is excluded, since it is known and can be obtained when objects are not present)

2. Given the coordinates of the transmitter and receivers and the corresponding distances L_{mn}, the equations of ellipses are obtained:

$$A_{mn}x^2 + B_{mn}xy + C_{mn}y^2 + D_{mn}x + E_{mn}y + F_{mn} = 0, \tag{4.4.14}$$

where the coefficients A_{mn}, B_{mn}, C_{mn}, D_{mn}, E_{mn} and F_{mn} are determined by coordinates (x_{O_m}, y_{O_m}) and (x_{R_n}, y_{R_n}) and the corresponding distances L_{mn}.

3. Given the equations (4.4.14), the intersections of ellipses are found by solving the systems of two equations:

$$\begin{cases} Ax^2 + Bxy + Cy^2 + Dx + Ey + F = 0 \\ \hat{A}x^2 + \hat{B}xy + \hat{C}y^2 + \hat{D}x + \hat{E}y + \hat{F} = 0, \end{cases} \tag{4.4.15}$$

where A, B, C, D, E, F and $\hat{A}, \hat{B}, \hat{C}, \hat{D}, \hat{E}, \hat{F}$ are the coefficients A_{mn}, B_{mn}, C_{mn}, D_{mn}, E_{mn} and F_{mn} with different indices mn and $\hat{m}\hat{n}$.

4) After solving the systems of equations, all the intersections are obtained and analyzed to find the positions of the objects. An illustrative example of this procedure when 3 receivers are used is shown in Fig. 4.4.18.

In Fig. 4.4.18 the blue triangles are intersections of the ellipses corresponding to receivers Rx1 (blue lines) and Rx2 (red lines), the black empty circles are intersections of the ellipses corresponding to Rx1 (blue lines) and Rx3 (black lines), while the red squares are intersections of the ellipses corresponding to receivers Rx2 (red lines) and Rx3 (black lines). By using the graph as shown in the middle part of Fig.radar-fig02fig02, these differently marked points can be interconnected to form all the possible triangles the vertices of which conform to the intersections of differently colored ellipses (in this example only three combinations are shown). If the lengths of at least two edges (a, b or a, c or b,

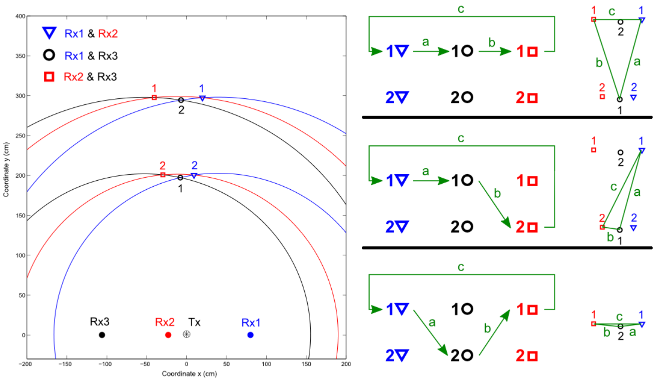

Figure 4.4.18: Intersections of differently colored ellipses corresponding to Rx1 (blue lines), Rx2 (red lines) and Rx3 (black lines), and 3 combinations of their interconnections (triangles on the right side) obtained by using the graph (in the middle part) consisting of all the differently marked intersections

c) are less than a predefined threshold value, then it is assumed that the three intersections which are the vertices of the triangle, correspond to one object, the position of which is assumed to conform to the centroid of the triangle as shown in Fig. 4.4.19.

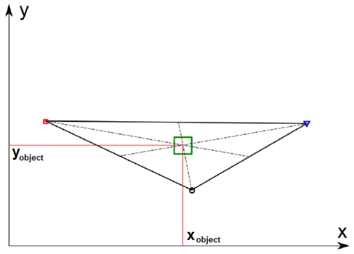

Figure 4.4.19: Position of the found object at the centroid of triangle the vertices of which conform to differently marked intersections of ellipses corresponding to Rx1, Rx2 and Rx3 and the lengths of two edges of which are less than a predefined threshold value

Experimental results. The first experiment was carried out by using one Tx and two Rx antennas, and the object was a 1m×1m metal plate which was placed on a straight line perpendicular to the line connecting the antennas at the distance of 0.6m and increasing by 0.2m up to 3m from Tx. The obtained localization results are shown in Fig. 4.4.20 and correspond well to the real positions of the object as it produces strong reflections and peaks of the received pulses can be clearly distinguished.

The second experiment was carried out by using the same antennas, but the object was a person that was approaching and then moving away from Tx in the same straight line. The obtained positions are shown in Fig. 4.4.21 with the

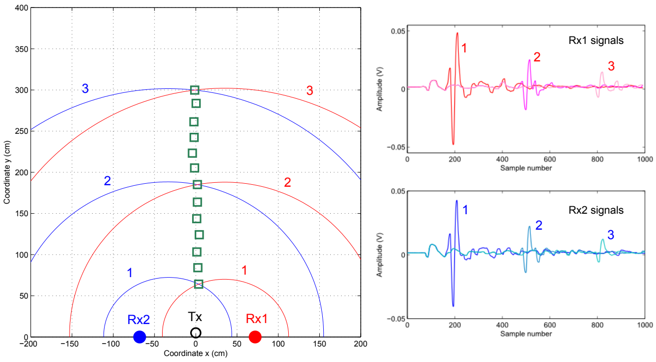

Figure 4.4.20: Localization result of the metal plate placed on a straight line perpendicular to the line connecting the antennas at the distance of 0.6m and increasing by 0.2m up to 3m from Tx (the signals on the right side are obtained at the receivers Rx1 and Rx2 allowing to produce the corresponding ellipses 1, 2, and 3)

dots getting darker as time progresses. The obtained signals at both receivers are shown on the right side with the red line representing the location of a global maximum point in each signal. As it follows, the positions are more precise at smaller distances from Tx since stronger reflections are obtained, and more noise is produced when the object is located at larger distances from antennas. After reducing the noise by filtering the obtained red lines on the right side of Fig. 4.4.21, the result improves at larger distances as shown in Fig. 4.4.22 (it is noted that all the processing is causal with the output depending only on past and current received signals).

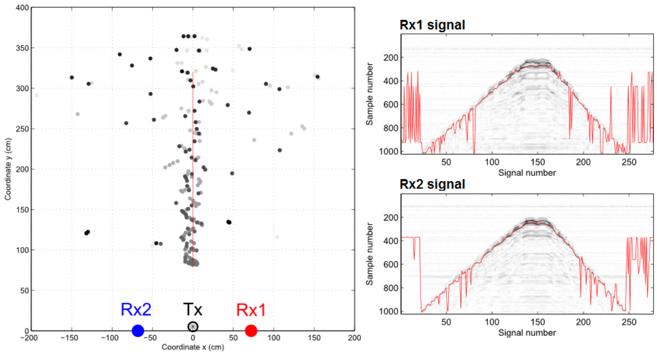

Figure 4.4.21: Localization result of a person approaching and then moving away from Tx in the straight line – the dots (positions) are getting darker as time progresses (the signals on the right side are obtained at Rx1 and Rx2 with the red line representing the location of a global maximum point in each signal)

The third experiment was carried out by using one Tx and three Rx antennas, and the object was a person that was moving along a triangular trajectory

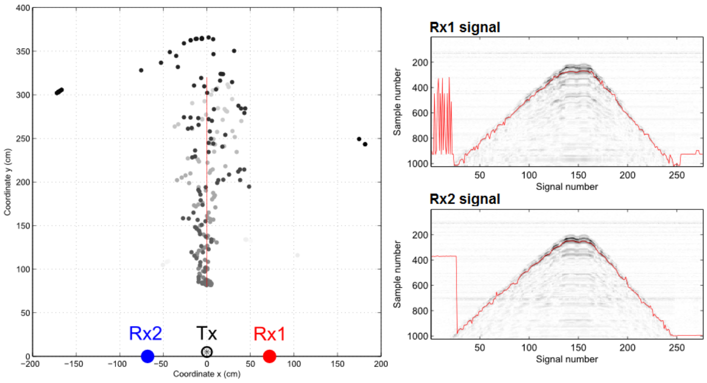

Figure 4.4.22: Localization result of Fig. 4.4.21 after causal filtering of the red lines on the right side of Fig.radar-fig05fig05

(anticlockwise). The obtained positions are shown in Fig. 4.4.23 with the points getting darker as time progresses. The first upper figure is obtained when ellipses corresponding to Rx1 and Rx2 are used, the second upper figure is obtained when ellipses corresponding to Rx1 and Rx3 are used, the third upper figure is obtained when ellipses corresponding to Rx2 and Rx3 are used, and the fourth upper figure is obtained when ellipses corresponding to Rx1, Rx2 and Rx3 are used by combining all the intersections as explained in Fig. 4.4.18. The lower three figures show the obtained signals at the receivers with the red lines representing the estimated locations of reflected pulses in the signals. As it follows from the rightmost upper figure, the calculated positions conform approximately to the real trajectory.

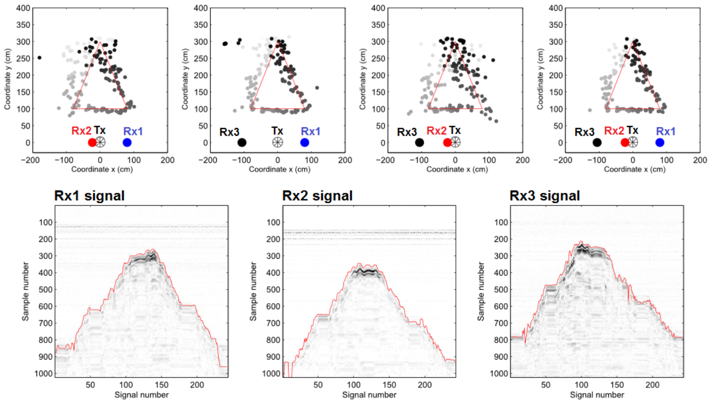

Figure 4.4.23: Localization result of a person moving along a triangular trajectory (anticlockwise) – the dots (positions) are getting darker as time progresses (the lower three figures show the signals at Rx1, Rx2, and Rx3 with the red lines representing the estimated locations of reflected pulses in the signals)

The last experiment was carried out by using one Tx and three Rx antennas, and the objects were two persons approaching and then moving away from antennas at different speeds along straight lines perpendicular to the line connecting the antennas. The obtained positions are shown in Fig. 4.4.24 allowing to conclude that the limitation of the current method is that only one object most closely located to antennas can be detected due to only the first reflected pulses are considered. The problem of detecting and tracking multiple objects will be the topic of further research.

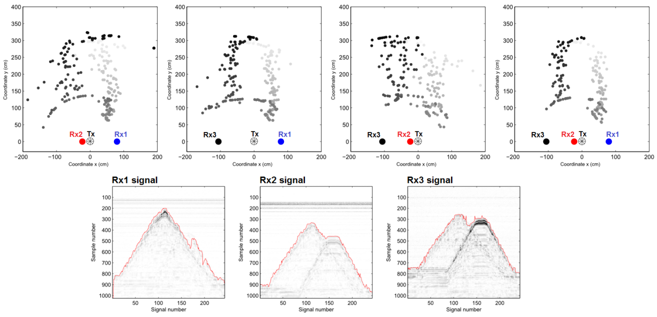

Figure 4.4.24: Localization result of two persons approaching and then moving away from antennas at different speeds along straight lines perpendicular to the line connecting the antennas – the dots (positions) are getting darker as time progresses (the lower three figures show the signals at Rx1, Rx2, and Rx3 with the red lines representing the estimated locations of the first reflected pulses in the signals)

4.4.3 Short range UWB radar development

4.4.3.1 Miniature UWB radar sensor development

One of projects goals is a development of UWB radar sensor prototype. The prototype could be used for a range of applications indoors for example in security systems as simple movement detector replacing shortcomings of PIR sensor or using more than one of them for position tracking in rooms for more detailed information. Other applications could be mobile ice thickness detector as a convenient alternative to drilling a hole in ice. For the sensor to be useful in these applications it should be able to work autonomously, make local computations and if necessary transmit data to other devices like smartphone, tablet or personal computer. Additionally, a LCD display was included for debugging and local data indication purposes (Fig. 4.4.25).

UWB radar sensor uses sampling receiver principles where samples are received from the high frequency signal and converted to low frequency equivalent time signal. That allows to simplify the main sensor board. The obtained raw signal can be pre-processed in the on-board micro controller (Stm32F4 series); the results are displayed on the two line LCD or sent to PC via USB for more sophisticated signal processing.

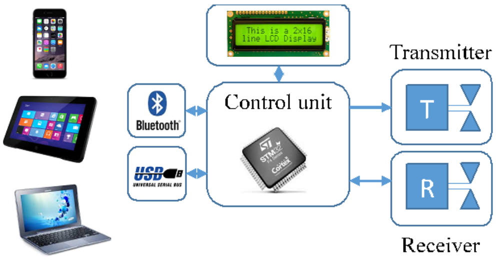

Figure 4.4.25: Radar sensor block diagram.

The experimental radar sensor prototype with mock-up antennas can be seen in Fig. 4.4.26.

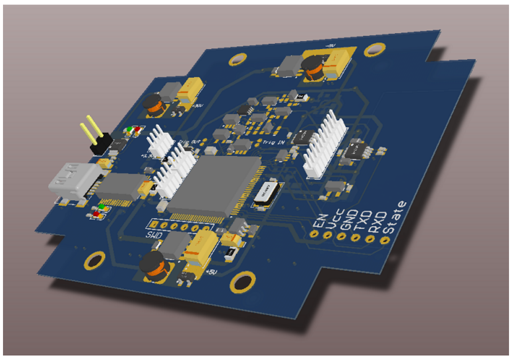

(a) PCB 3D model

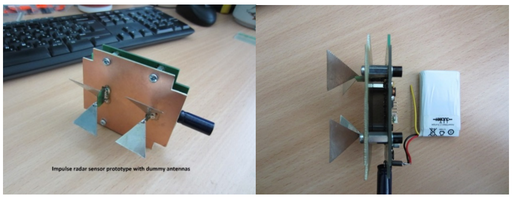

(b) Sensor front view (c) Sensor top view

Figure 4.4.26: First experimental radar sensor prototype images.

Besides circuit improvements and debugging, a lot of work was done to develop suitable antennas for this prototype. The improved prototype with shielded Bow-Tie type antennas can be seen in Fig. 4.4.27 (a).

Signal acquired from the UWB radar sensor is illustrated in Fig. 4.4.28. The first pulse does not represent reflection but corresponds to the signal received directly from transmitter at the shortest distance; the second pulse is reflected from a metallic object.

There were observed several problems with particular prototype. One or few circuit blocks did not meet expected jitter and noise parameters. Data from receiver were distorted and equivalent input frequency of receiver was lower than expected. Radar sensor prototype functional blocks must be tested separately to identify faulty sections. That lead to development of universal UWB radar

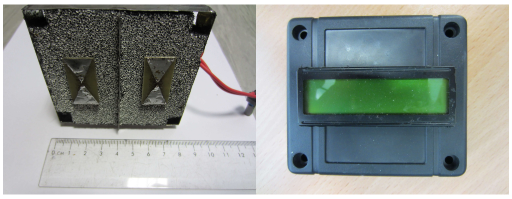

(a) Sensor front view (b) Sensor top view

Figure 4.4.27: Improved experimental radar sensor prototype.

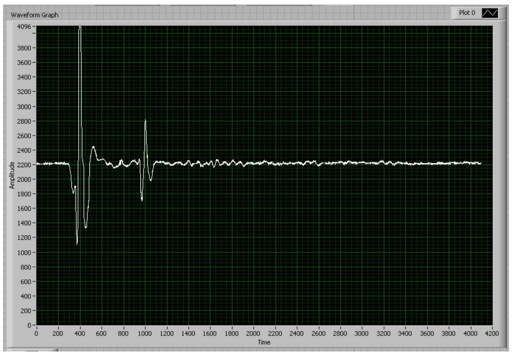

Figure 4.4.28: Reflection from an object.

with proper noise and jitter analysis in each of functional blocks.

4.4.3.2 Universal UWB radar prototype design

Certain requirements needs to be met to use the radar for broader application spectrum in smart city applications:

1. Device size must be as compact as possible.
2. Low power consumption (under 5 W).
3. Low noise figures for reliable operation.

Device capability requirements were deduced from evaluation of previous radar prototypes. Data acquisition had to be improved for fast and dynamic process monitoring. For example fast moving car detection or precise people location tracking. Signal acquisition jitter, which includes both receiver sampling jitter and pulse transmitter jitter, has to be under 12 ps for correct equivalent time conversion. Central frequency bandwidth had to be increased to increase range resolution for more accurate measurements and easier multiple object detection.

Sampling jitter in previous versions were higher than expected which interferes with signal processing and reduces accuracy of results. Total jitter is a combination of several jitter sources. Main source of jitter is fast saw circuit in combination with both control comparators. Fig. 4.4.30. Fast saw signal noise

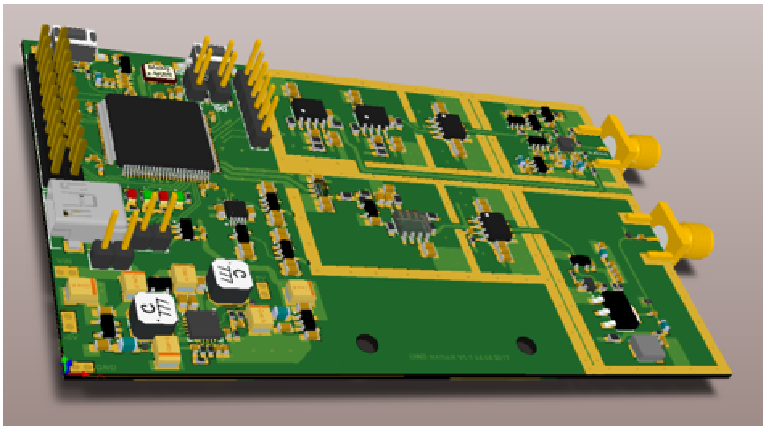

Figure 4.4.29: Developed universal radar prototype

with low rise time (40 ns) can contribute to jitter as well as low comparator precision and noisy comparator power supply.

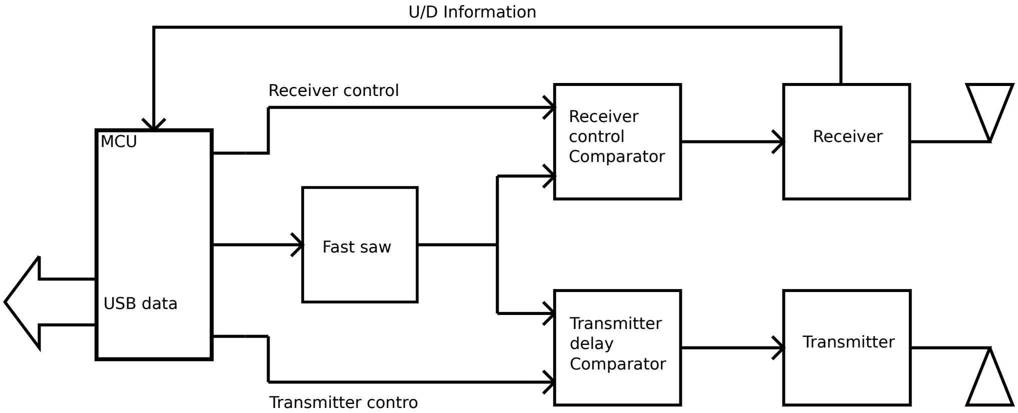

Figure 4.4.30: Radar functional blocks

PCB design plays a large role in reaching the set design requirements. For easier component and trace layout 4 layer PCB was used. Top layer is used as the main component and signal layer. Middle layer 1 is a ground layer which additionally shields top layer from lower power layer. Bottom layer is mostly used as a ground and signal layer. Current radar design is similarly arranged as shown in Fig. 4.4.30 so individual functional blocks in analog part of the circuit are isolated with exposed ground plane which can be used to shield them with metal cover to reduce incoming noise from electromagnetic radiation generated from different parts of the circuit: transmitter, antennas, MCU as well as environment. Shielding of transmitter and receiver is crucial as receiver itself is sensitive to noise and transmitter generates a lot of noise and is located very close to the receiver.

Some problems were identified with the design. Unbuffered DAC output traces were susceptible to noise witch was amplified after the DAC buffer Fig. 4.4.31(a). Trace length in combination with the trace location makes them

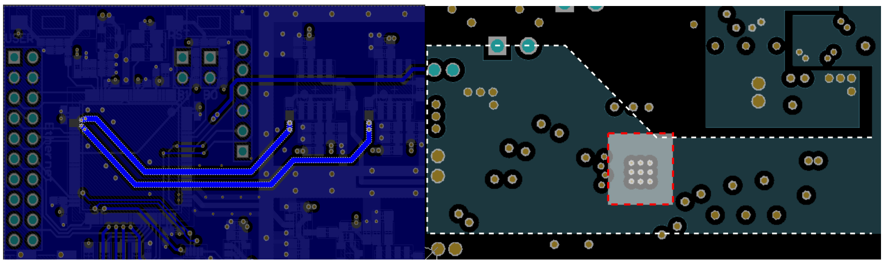
(a) DAC output trace layout (b) Power supply polygon and IC location

Figure 4.4.31: Identified problems with radar design (a)- Unbuffered DAC output trace layout at bottom layer. (b)- Power polygon outlined white crossing directly under power supply IC outlined red at power layer

vulnerable to noise generated by MCU and other sources. Both ends of the trace had to be cut and rewired over the air with shielded cable which isolates signal from noise generated by MCU. Another identified problem was negative voltage supply noise which was higher than expected. Part of the reason could be that the negative voltage polygon crosses directly under switch mode power supply integrated circuit which controls both positive and negative supply voltages. As the switching currents can be considerably high (700 mA) and switching happens directly trough the integrated IC, switching noise is induced in power polygon directly under the IC. Fig. 4.4.31(b). Unfortunately this problem cannot be solved with a simple fix so partial redesign of power supply circuit is required.

This universal radar prototype used older transmitter version with lower center frequency band because higher central frequency bandwidth transmitter development took place after the universal radar PCB was finished. For ability to implement new transmitter into the radar it was designed as a module to be placed on top of previous transmitter connecting it to PCB with wires over air and coaxial cables.To shorten the length of the wires input, output and power traces were located similarly to previous transmitter version.

4.4.4 Approbation: advanced traffic density measurements using UWB radar

Radar system for smart traffic density measurements was approbated at SIA "VPWash". System was tested for 2 weeks from December 1, 2017 and optimized for measurements. It was concluded that measurement precision mostly depends from selected position and its pointing direction. Radar system was set up at 4.5 meter height, 4 meters away from the beginning of the first driving lane and 7.5 from the second. After two weeks experimentation period and signal processing adaptation, system was approbated for another week on vehicle counting for both driving lanes. In addition to the radar system, another camera was set up to compare measurements and validate results for short time intervals.

During the 30 minutes observation period, radar system counted 78 cars

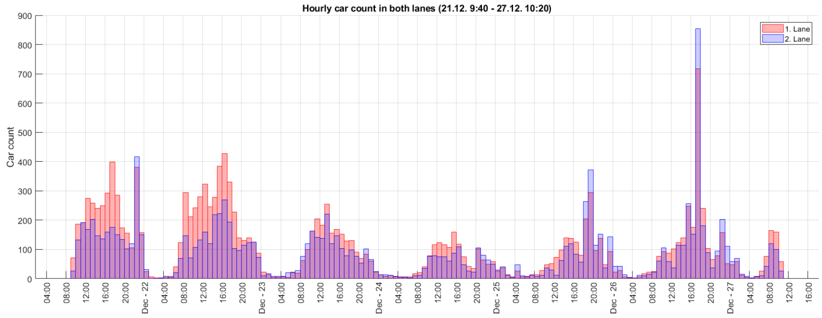

Figure 4.4.32: Detailed car count

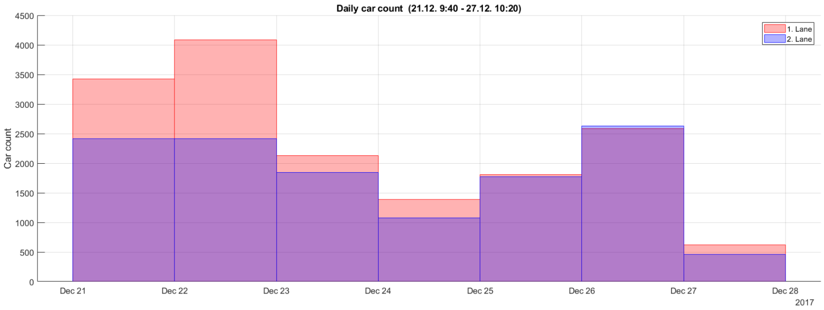

Figure 4.4.33: Daily car count

(from 86) in first driving lane and 44 (from 112) in second resulting in 90.6% precision for first lane and 39.2% for second. During observation period no false positive cars were counted. Later it was concluded that lack of precision was mainly because of bad radar setup angle.

4.4.5 Conclusions

During the execution of project, ultra wideband technology have established its place in smart city applications. In a technical report published by European Telecommunications Standards Institute on May 2017, it is stated that ultra wideband radar sensors will be most suited presence detectors in smart street lighting application [37]. Based on this publication, it is safe to assume that EDI RADAR team's research is a step in a right direction.

The most serious problem for UWB based sensor implementation in real life applications is a lack of manufactured devices. Frequency band in range from 3.1 GHz to 4.8 GHz is in early stage of development. That is why the main focus of the EDI RADAR team was on hardware development.

The project results of the EDI RADAR group are summarized in 6 publications, 1 attended exhibition, 2 Latvian Republic patents, 6 bachelor thesis and 1 predefended PhD thesis.

Chapter 4.5

RTU TI group: Development of fiber optics transmission technologies

4.5.1 General description of the research area

Nowadays, information transmission technologies using the optical fiber as the medium of information transmission bear a major importance in the field of telecommunications. The rapidly increasing volume of data flows to be transmitted demand a faster introduction of technologies in the telecommunications sector. Services like high-speed Internet and 3D television, which are ensured using one and the same client connection, demand ever increasing data transmission speeds. The analysis performed by the company Cisco shows that the data amount transmitted in access and metro networks has experienced a rapid increase, and already in 2013 exceeded the data flow amount transmitted in long-haul networks (see Fig. 4.5.12). This rate of increase will also continue further on and it is expected that in 2018 the amount of data transmitted in access and metro networks will amount to 62 % of the total transmitted data amount.

Bearing in mind the fact that the largest increase in the transmitted data amounts is observed at the access level, particular attention must be paid specifically to optical access networks. Most often, information transmission in these optical access lines right to the clients apartment or house is ensured using a single optical fiber (OF).

The subject-matter examined in the research is topical because currently Latvia is undergoing a rapid development of the communications sector. As of now, the existing optical access communications systems are using time division multiplexed passive optical network (TDM-PON) technology, but within the upcoming five years, as the need for bigger data transmission speeds increases, it will be necessary to update the existing network infrastructure and to introduce a high-speed wavelength division multiplexed passive optical network (WDM-PON) technology, which can ensure higher data transmission speeds (over 2.5 and 10 Gbit/s) at a longer distance (at least 20 km) than the current TDM-PON

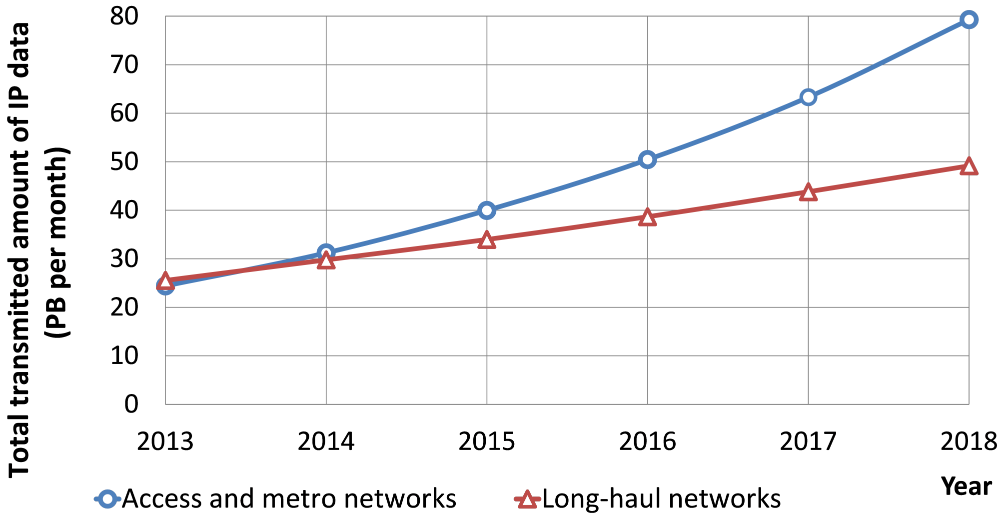

Figure 4.5.1: Cisco global transmitted traffic forecast for the time period from 2013 to 2018.

technology can provide (with transmission speeds of up to 2.5 Gbit/s).

The growing amount of Internet users and data flows (from such services as online video games, high resolution video streaming, telemedicine services, video conferencing, computerized high frequency trading systems and others) pose several challenges for the communications network operators, and they are forced to improve the infrastructure of the fiber optical network. Therefore, optical access networks must be capable of ensuring ever higher data transmission speeds (2.5 and 10 Gbit/s) with lower signal latency, by using the existing electrical and opto-electrical components inasmuch as possible. It must be mentioned that an ERDF project Next Generation Electronic Communications Networks in Rural Areas is being implemented in Latvia since 2012; its aim is to develop next generation networks (NGN) in the remote rural areas of Latvia and to promote the achievement of the Europe 2020 strategy targets (by 2020, to ensure that all households have an option to receive access to Internet at a minimum speed of 30 Mbit/s and 50 % of households in 2020 will have the Internet with the access speed of at least 100 Mbit/s). The project provides for developing a 7000 km long optical line which would ensure optical network access at 500 connection points. Thus, it will be necessary to ensure access technologies that perform last mile data transmission, which is the network from the service providers access point to an individual telecommunications service user. The technologies and solutions developed within the research can be fully used for successful implementation of the aforementioned project and for ensuring communications services from the service provider to the end-user.

The electrical and opto-electrical components, which are found in the transmitter and receiver block (transceiver) of the high-speed fiber optical access transmission system, are considered to be its weak point or bottleneck due to the limited frequency bandwidth and the transmission speed. The transmission speed of electrical components and accordingly the throughput band is restricted by the switching speed of transistors contained therein, as well as the heat originating as a result of it, which must be released. The solution for the limited throughput bandwidth problem that does not require a complete transceiver replacement is an electro-optical spectrum sliced transceiver for high bitrate optical signal transmission and receiving in optical access networks, where, by using digital signal processing (DSP), the electrical baseband signal containing the transmitted information is sliced. Certain parts of the sliced signal are transmitted through the fiber optical access network and the initial signal is restored in the receiver. Such spectrum sliced transceiver can ensure faster transmission speeds by using the already existing transceivers with a limited frequency throughput bandwidth. This way, the telecommunications service provider can increase the frequency bandwidth of optical access network components multiple times and accordingly also the transmission speed.

Next generation optical access networks must be adaptive with regard to the ensured data transmission frequency bandwidth, which can dynamically change depending on the user demand. Thus, spectrum sliced transceiver technology, using DSP, in the nearest future will be a potential solution for overcoming the restrictions imposed by the limited frequency bandwidth of electrical components.

The given studies were conducted together with Technical University of Denmark (DTU), at the Metro-access & Short Range Systems Group Laboratory, in collaboration with researchers from DTU Fotonik (Denmark) and Heinrich Hertz Institute (Germany) under the supervision of Professor Idelfonso Tafur Monroy and the Assoc. Prof. Juan Jos Vegas Olmos.

4.5.2 Analysis of different optical access network topologies

By employing the baseband electrical signal spectrum slicing method, it is possible, using the electro-optical transceivers already existing in optical access networks, to transmit a signal that is spectrally at least two times or four times broader than it is possible by high frequency electronics used therein, without replacing the existing electrical and electro-optical components with others. Spectrum slicing method is scalable, which means that the electrical signal with N GHz frequency bandwidth can be sliced not only in two signal slices, each taking up $\triangle f_{slice} = N/2$ GHz frequency baseband, or in four slices (each taking up $\triangle f_{slice} = N/4$ GHz frequency baseband), but even in 10 slices ($\triangle f_{slice} = N/10$ GHz). Signal processing in frequency or time domain is performed in a DSP block, which in essence is a MATLAB computing environment, where the fast Fourier transform or the inverse fast Fourier transform of the transmitted signal is realized, see Fig. 4.5.13.

Spectrum sliced signal slices can be transmitted one after another using time division multiplexing (TDM) (see Fig. 2a) or parallel by employing wavelength

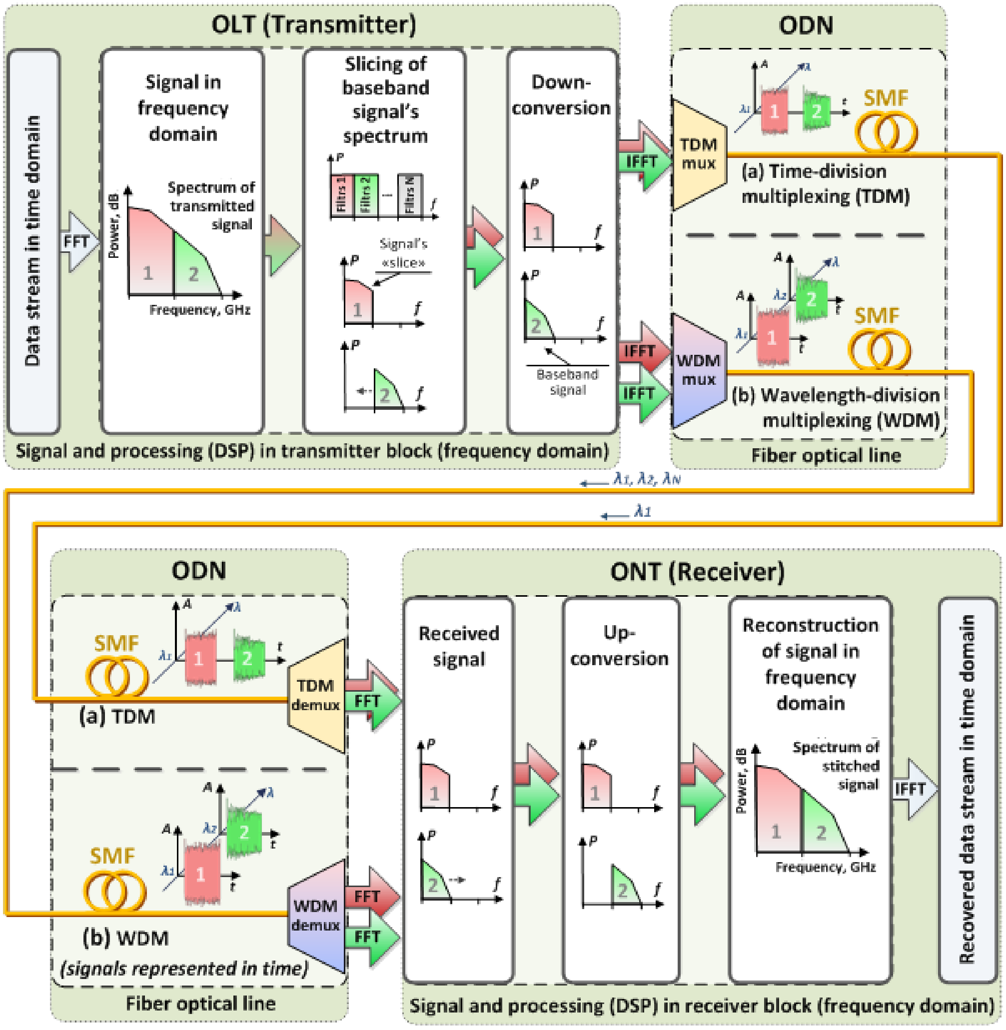

Figure 4.5.2: Principle of slicing an input electrical baseband signal into two equal bandwidth slices at the OLT, transmission, reception and a reconstruction of the origin signal waveform at the ONT by using: (a) TDM or (b) WDM multiplexing technique.

division multiplexing (WDM) (see Fig. 2b). In both cases, the bandwidth of electro-optical and electrical components of the transceiver is scalable and the necessary electrical bandwidth of the high-frequency network hardware is at least two times smaller than in the case of the initial electrical signal before slicing.

4.5.2.1 Development of spectrum sliced transceiver

To prove the spectrum slicing technology principle and to assess its performance, an experimental prototype of a spectrum sliced transceiver was developed and its operation was assessed. The created prototype performs 1 Gbit/s NRZ electrical data signal slicing in two limited bandwidth slices, modulates them in optical domain one after another over time, transmits along up to 25 km long single-mode optical fiber (SMF) span, receives and restores the initial waveform of the signal, using a bandwidth of electrical equipment that is two times smaller, namely 500 MHz. The experimental scheme of spectrum sliced transceiver is shown in Fig. 4.5.14. It must be noted that before processing in DSP block, the electrical NRZ signal with the transmission speed of 1 Gbit/s takes up 1 GHz frequency baseband, whereas after processing with DSP, not more than 500 MHz.

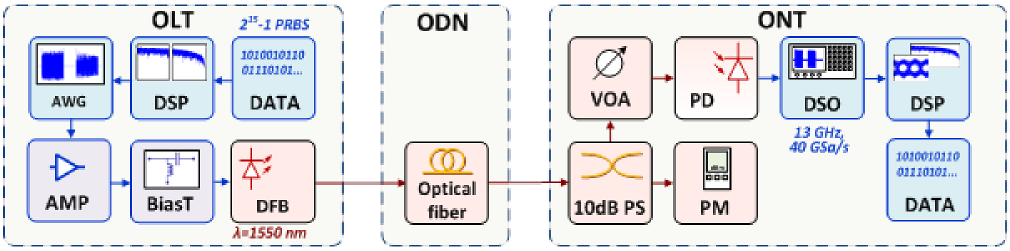

OLT – Optical line terminal
ONT – Optical network terminal
ODN – Optical distribution network
DSP – Digital signal processing block
DATA – Bit sequence generator
AMP – Electrical signal amplifier
BiasT – Alternating current and direct current splitter/coupler
DFB – Distributed feedback laser
AWG – Arbitrary waveform generator
VOA – Variable optical attenuator
PD – Photoreceiver with PIN photodiode
PM – Optical power meter
DSO – Digital storage oscilloscope
PS – Optical power splitter

Figure 4.5.3: Experimental setup of sliceable transceiver for slicing electrical baseband signal into two slices, transmission and reconstruction of initial signal in the receiver.

Initially, the electrical signal generator is creating a pseudo-random $2^15 - 1$ bit sequence with the bandwidth of 1 GHz, which is fed to the coder and a NRZ coded electrical signal is created with the transmission speed of 1 Gbit/s (see Fig. 4.5.4 a). This electrical signal contains information, which is transmitted in the created optical communications system. The spectrum of transmitted electrical signal with 1 GHz occupied electrical frequency baseband is shown in Fig. 4.5.4 b.

In the DSP block, using digital signal processing in the MATLAB environment, the electrical data signal, which takes up 1 GHz frequency bandwidth (see Fig. 4.5.4 b), will be sliced into two identical bandwidth ($\triangle f_{slice} = 500MHz$) frequency slices (see Fig. 4.5.5). After the slicing operation, the signal slice with the higher frequency band (2^{nd} slice) was shifted to the baseband (see Fig. 4.5.5 b) using DSP. Afterwards, once both frequency slices are in the baseband from 0 to 500 MHz, they are prepared for transmission through the fiber optical transmission line.

To perform both frequency slice transmission, they together with a 2.45 μs time guard-band were combined in a single signal, which, as a result, took up no more than 500 MHz frequency baseband. This bandwidth is two times smaller than the bandwidth taken up by the signal before the slicing operation. The length of a signal containing each slice waveform is 4.1 μs. Figure 6a shows both slices separately in a time domain (for better representation, only time-frame

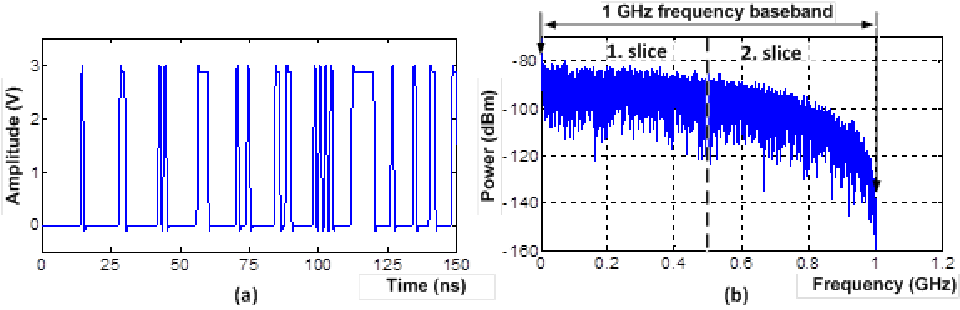

Figure 4.5.4: (a) Time diagram and (b) spectrum of generated 1 Gbit/s electrical signal.

from 0 ns to 150 ns is shown) as well as both slices combined in a time domain (see Fig. 4.5.6 b).

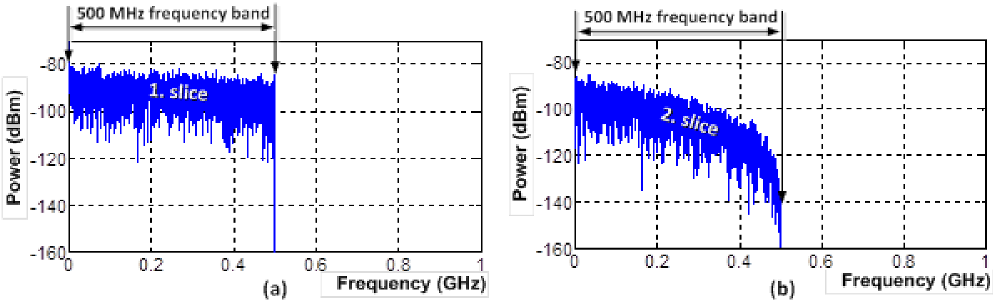

Figure 4.5.5: Spectrum of sliced signal with 1 GHz bandwidth into two 500 MHz bandwidth slices.

The signal with the waveform shown in Fig. 4.5.6 b containing both slices is sent to 1.25 GS/s Agilent arbitrary waveform signal generator (AWG) with the bandwidth of 500 MHz. In the output of AWG, an electrical signal of a certain waveform is generated depending on the digital control signal as shown in Fig. 4.5.6 b.

The electrical signal generated in the output of AWG was amplified and used through BiasT (separator of direct current from alternating current) for direct DFB laser modulation. In the experiment, a DFB laser with the central wavelength of $\lambda = 1550$ nm was used. It was measured that the average optical signal power on the output of directly modulated laser was 2.9 dBm. The further modulated optical signal was fed into the optical distribution network (ODN) depicted by the optical single-mode fiber. The received signal quality and the

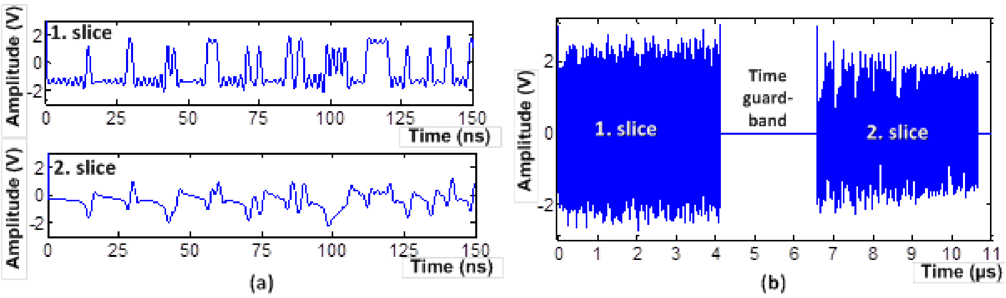

Figure 4.5.6: (a) Separately shown time diagrams of both 500 MHz slices and (b) time diagram of formed electrical signal obtained by combining both slices in time, which is used for direct modulation of DFB laser.

performance of spectrum sliced transceiver was assessed using 3 different single-mode optical fiber types up to 25 km long: standard single-mode optical fiber (SMF), dispersion shifted fiber (DSF) and non-zero dispersion shifted optical fiber (NZ DSF). The received optical signal was initially split in the power splitter (PS), where one output with 10 dB attenuation was used for system monitoring purposes, whereas the other was fed further on to a variable linear attenuator (VOA).

The optical signal from the output of VOA was fed to the photoreceiver block with PIN photodiode, where it was transformed into an electrical signal. In a B2B configuration (without an optical transmission line) the average received signal power was -6.4 dBm. The electrical signal in the output of the photoreceiver (see Fig. 7a) was received and stored in the *Agilent* digital storage oscilloscope (DSO) memory. Experimentally used DSO featured a 13 GHz frequency bandwidth, and for recording the received electrical signal, 1.25 GSa/s sampling rate was used. The signal stored in the DSO memory was then processed in the DSP block, as a result, from two signal slices, which both together took up a 500 MHz frequency baseband, the initial 1 GHz signal was reconstructed, and the BER was evaluated depending on the average power of the received optical signal. In order to restore the initial signal waveform from the received signal (see Fig. 4.5.7 a) containing both sliced signal slices, each individual signal slice was extracted (see Fig. 4.5.7 b).

In order to successfully restore the transmitted signal, it is necessary that the second slice is located in its initial frequency band (from 0.5 to 1 GHz). Therefore, by using DSP, the second slice was shifted to its initial position, which meant that all pre-requisites were met for restoring the sliced, transmitted and received signal (see Fig. 4.5.8 a and 4.5.8 b).

As the second slice is located in its initial frequency position, it is possible to combine both frequency slices in a single baseband signal, as seen in Fig. 4.5.9 a.

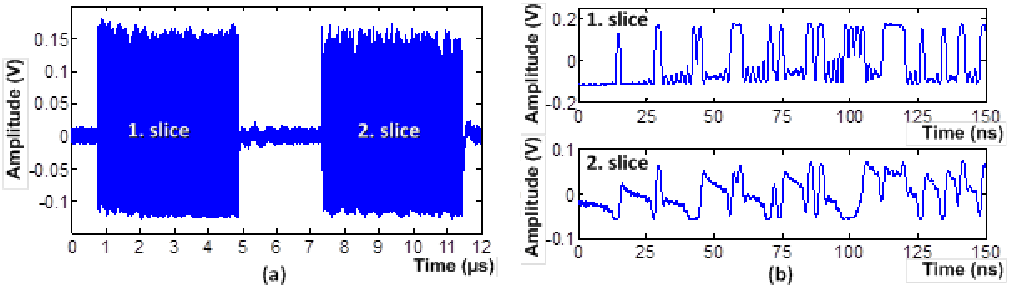

Figure 4.5.7: (a) DSO captured electrical waveform which is used for further processing in DSP block and (b) both electrical slices of received signal, separated in time by using DSP.

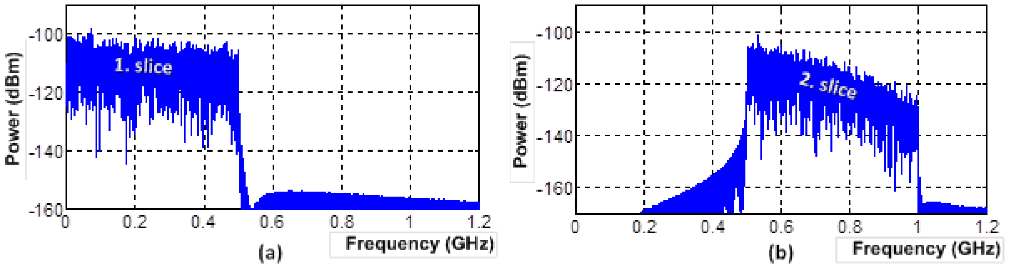

Figure 4.5.8: (a) Spectrum of first slice and (b) second slice extracted from received signal, before realization of signal stitching operation in DSP block.

Figure 4.5.9 b shows that the eye diagram opening of the restored signal after receiving in B2B configuration (the transmitter output is connected directly to the receiver input with an optical patch cord) is big enough; however, minor signal distortions are observed, as well as jitter. The cause of these distortions is the use of an electrical amplifier, as well as multiple digital signal processing (FFT, IFFT) in the time and frequency domain. Figure 4.5.10 shows a comparison between the initial 1 Gbit/s NRZ signal and the restored 1 Gbit/s NRZ signal, which was transmitted, received and restored, using the 500 MHz electrical frequency bandwidth.

As shown in Fig. 4.5.10 b, using the restored signal it is possible to fully reconstruct the initial sequence of bits, which was transmitted and received using the spectrum sliced transceiver solution. Figure 4.5.11 a shows the eye diagram of received signal after a 25 km transmission through a standard single-mode optical fiber (SMF) section. As can be seen, the eye is open enough, which

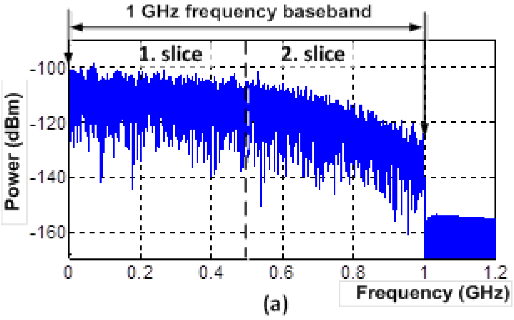

Figure 4.5.9: (a) Spectrum of restored 1 Gbit/s electrical baseband signal and (b) its eye diagram after signal detection in B2B configuration (without using transmission line).

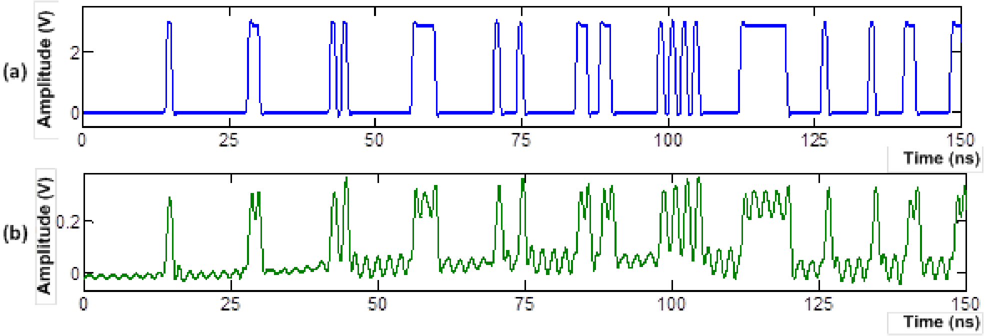

Figure 4.5.10: (a) Time diagram of initial input electrical signal before realization of slicing operation and (b) time diagram of transmitted and restored sliced signal.

means that successful information transmission can be achieved in the distance of up to 25 km. BER, depending on the average received optical power of the signal, by employing SMF, DSF and NZDSF optical fibers in the transmission can be seen in Fig. 4.5.11 b. This diagram shows the performance of a spectrum sliced transceiver with the data transmission speed of 1 Gbit/s, by realizing the electrical baseband signal slicing, transmission and stitching in the receiver, using DSP.

As shown in the BER diagram, by employing forward error correction (FEC) with 7 % of data overhead and ensuring at least the average optical signal power -15.8 dBm received at the photoreceiver, the two slice spectrum sliced transceiver can ensure error-free data transmission with BER $< 10^{-10}$, by using up to 25 km long optical line with the SMF, DSF, or NZDSF optical fiber for data transmission. An additional 7 % overhead means that the transmitted bit sequence is

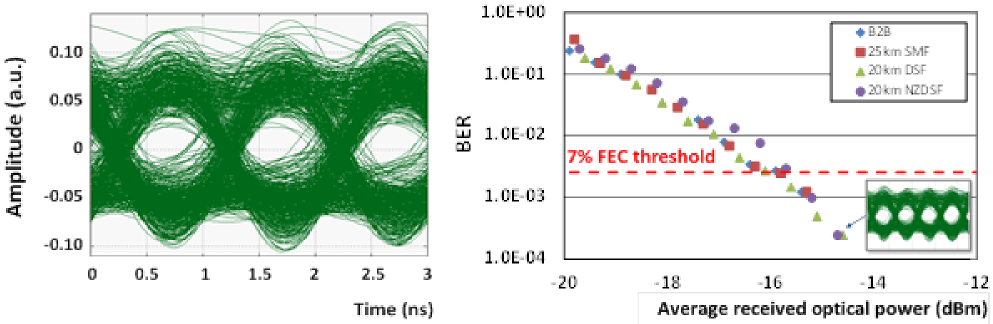

(a) (b)

Figure 4.5.11: (a) Eye diagram of detected and restored signal after transmission through 25 km long standard single-mode fiber, and (b) BER as a function of received power by using various optical fiber types in transmission.

supplemented with additional 7 % of bits, which allows performing error correction of the received signal bit sequence, if any errors have occurred. By employing the forward error correction, it is possible to perform the signal BER correction from the level BER $< 2.55 \cdot 10^{-3}$ to the level BER $< 1 \cdot 10^{-10}$.

4.5.3 Investigation on the minimum channel spacing in the WDM-PON system taking into account channel bitrate, laser parameters and overall spectral and energy efficiency

In the WDM-based PON, five separate stages of the optical signal transmission could be set off: (i) generation of a carrier signal; (ii) multiplexing the optical signals; (iii) transmission of optical signals along a fiber-optical link (FOL); (iv) separation of optical signals according to the wavelengths (frequencies); (v) reception, demodulation and detecting of signals (see Fig. 4.5.12.). The first and the fifth stages are linked to the chosen format of optical signal modulation. The second and the fourth stages are connected with the method that is used for assignment of channel central frequencies. The third stage is associated with the mechanisms of linear and nonlinear distortions that affect transmission of modulated signals in the optical fiber. The assignment of central wavelengths (or frequencies) of the channels is based on two ITU-T recommendations: G.694.1 and G.694.2. The former recommendation describes the fixed and elastic DWDM gratings. In case of a fixed DWDM grating, the recommendation determines only and solely the central frequencies of channels at different channel spacing values, e. g., 200, 100, 50, 25 and 12.5 GHz, while in the elastic DWDM grating case this recommendation determines not only the channel central frequencies, but also the width of frequency slot. In this case for assignment of central frequency of the channels a 6.25 GHz step is used (see Eq. 4.5.1), whereas for determination of the width of frequency slot twice as large step is taken, i. e., 12.5 GHz (see Eq. 4.5.2).

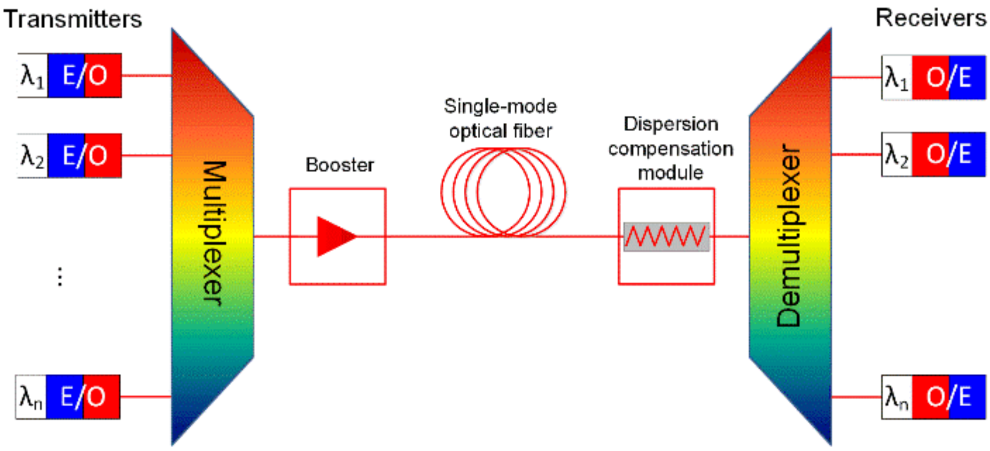

Figure 4.5.12: A simplified block-diagram of the WDM-based PON.

It has been necessary to introduce the elastic DWDM since the fixed DWDM grating works well, while in the WDM system all transmission channels operate at one data transmission rate and/or for modulation of optical signals the same modulation format is used. In the opposite case, either overlapping of optical channels occurs or the frequency resources of optical fiber are employed inefficiently.

$$f_c = 193.100 + n0.00625[THz], n = 0, \pm1, \pm2, \pm3, ... \tag{4.5.1}$$

$$\Delta f_{width} = 12.5m[GHz], m = 1, 2, 3, ... \tag{4.5.2}$$

Analysis of the signal propagation along an optical fiber evidences that one of the main linear effects which significantly distort transmission of signals in the backbone optical networks is the ASE noise due to optical line amplifiers (OLAs), while the cross-phase modulation (XPM) is the main nonlinear optical effect. The level of ASE noise at the receivers end directly depends on the noise factor of the EDFA used, on the gain itself determined by the distance between two OLAs, on the optical fiber attenuation coefficient and on the bandwidths of the electrical and optical filter used. This happens because the ASE noise after its reception and optical-to-electrical conversion appears as electrical noises. The XPM causes just increase in the amplitude noises that arise due to dispersion observed in optical fibers. Such dispersion converts the phase modulation into the intensity modulation. Therefore, the XPM-related amplitude noises can seriously affect the intensity-manipulated signal (e. g., NRZ-OOK) transmission and the BER value at the receivers end. It has been found that in case of 10 Gbps NRZ-OOK transmission with the quality of received signal being $Q = 7.3$, the level of XPM-related nonlinear noises exceeds noises by more than 20 times due to four-wave mixing (FWM). Considering the degrees of freedom for the optical signal the amplitude (intensity), phase and state of polarization the modulation formats that manipulate with the given degrees of freedom have been determined (see Fig. 4.5.13). The non-return-to-zero encoded on-off Keying (NRZ-OOK) is a historical solution for 10 G bit/s networks. The phase of the optical signal is already employed in the next stage of optical network development namely, in the 40 G bit/s channel. In this case, one of the common modulation formats is the NRZ encoded differential phase-shift keying (NRZ-DPSK). The differential quadrature phase-shift keying (DQPSK) and the optical duobinary format (ODB) are an alternative solution for a data rate of 40 Gbps in a single wavelength.

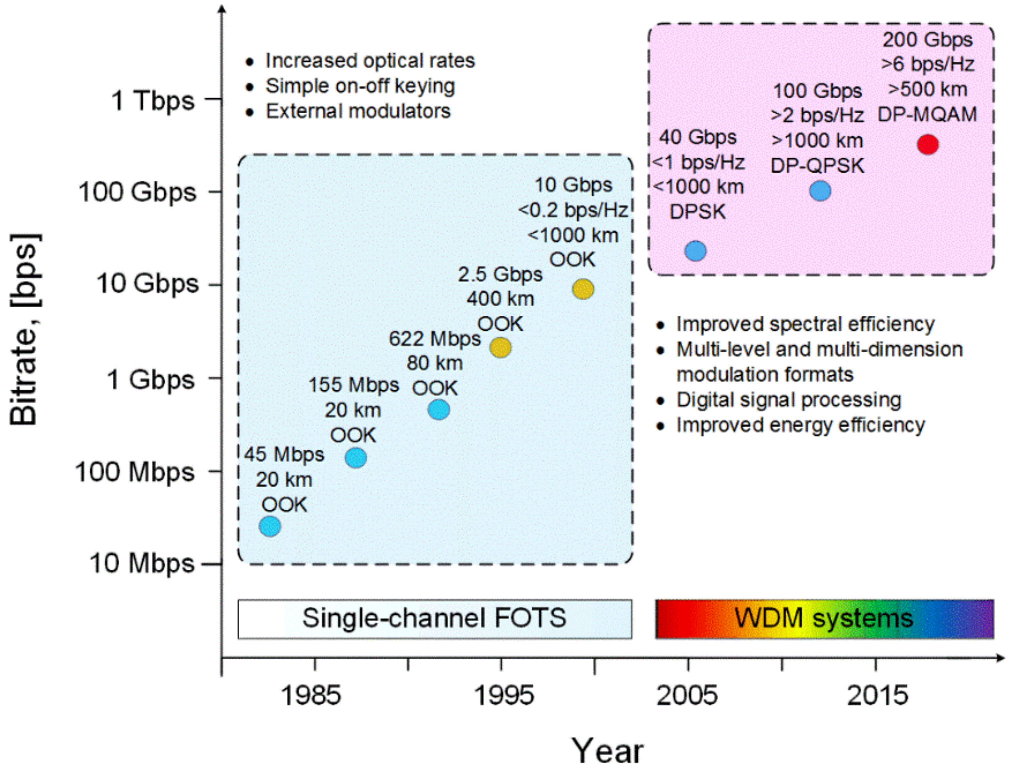

Figure 4.5.13: The development of transmission rate and modulation formats used in optical primary networks in the time period from 1980 to 2015.

As far as the optical signal state of polarization is concerned even though this could also be applied to optical signal modulation (e. g., using the binary orthogonal polarization state keying (2-POLSK)) in the backbone optical networks of today this state is employed for additional optical signal polarization division multiplexing (PDM). For example, in case of 100 Gbps DP-QPSK solution two 50 Gbps QPSK signals are multiplexed after they have been in the particular state of polarization, one of them having linear X-polarization while the other linear Y-polarization. The optical signal polarization division multiplexing (PDM or PolMux) allows reducing the width of frequency band required for transmission and the baud rate. For demodulation of such multi-level and multi-dimension modulation formats it is necessary to apply the coherent detection methods and digital signal processing (DSP). Dealing with coherent optical signal modulation formats one more distortion source should be taken into account phase and frequency noises from the transmitter and receiver laser sources. This is especially important, since for cost minimization semi-conductor lasers are employed to generate radiation.

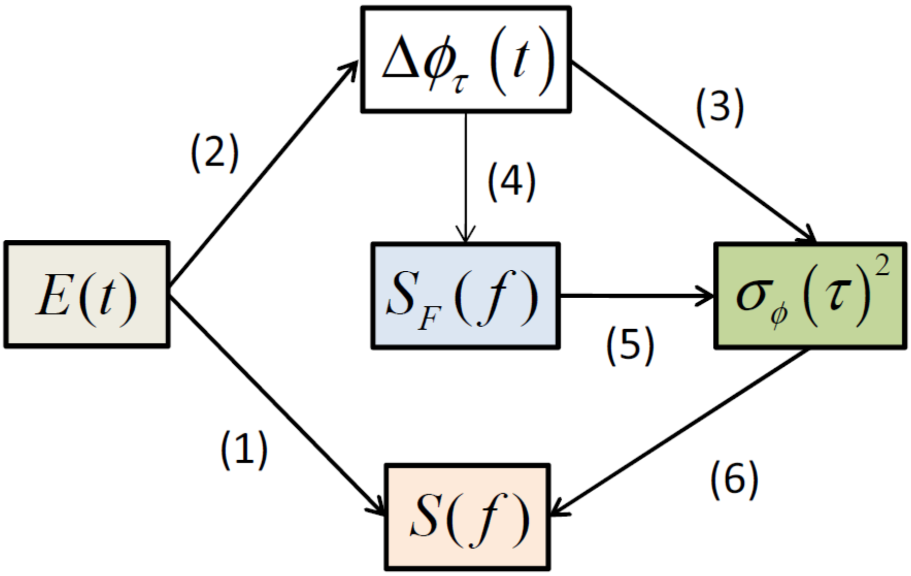

Figure 4.5.14: Relations among the complex amplitude $E(t)$ of laser field, the phase difference $\Delta\phi_\tau(t)$, the field spectrum $S(f)$, the frequency noise spectrum $S_F(f)$, the phase difference spectrum $S_{\Delta\phi_\tau}(f)$ and the phase noise variance $\sigma_\phi^2(\tau)$.

Several functions could be used for characterizing the laser field the phase and frequency noise spectra are one of them. Fig. 4.5.14 shows the relations among the complex amplitude $E(t)$ of laser field, the phase difference $\Delta\phi_\tau(t)$, the field spectrum $S(f)$, the frequency noise spectrum $S_F(f)$, the phase difference spectrum $S_{\Delta\phi_\tau}(f)$ and the phase noise variance ${\sigma_\phi}^2(\tau)$. Mathematical expressions which are linking each of these parameters are given by eqs. (4.5.3) to (4.5.8).

$$S(f) = \langle | \, F[E(t)] \, |^2 \rangle \tag{4.5.3}$$

$$\Delta\phi_\tau(t) = \phi_n(t) - \phi_n(t-\tau) \tag{4.5.4}$$

$${\sigma_\phi}^2(\tau) = \langle \Delta\phi_\tau(t)^2 \rangle \tag{4.5.5}$$

$$S_{\Delta\phi_\tau}(f) = 4\left(\frac{\sin(\pi \cdot f \cdot \tau)}{f}\right)^2 S_F(f) \tag{4.5.6}$$

$$\sigma_\phi{}^2(\tau) = 4\int_0^\infty \left(\frac{\sin(\pi \cdot f \cdot \tau)}{f}\right)^2 S_F(f)df \tag{4.5.7}$$

$$S(f) = F\left[\exp\left(-\frac{\sigma_\phi^2(\tau)}{2}\right)\right] \tag{4.5.8}$$

Note that the Fourier transformation is represented as $F[*]$ where $\langle * \rangle$ is the ensemble average.

4.5.4 Studies of optical fiber nonlinearity coefficient

Research on optical fiber nonlinearity coefficient measurements first of all involved development of the measurement method. It is based on the four wave mixing initiation in the fiber and requires two optical sources, namely pump and signal separated in the frequency domain that are passed through the fiber under test. Due to fiber nonlinearity there is a new frequency component called idler appearing at the output spectrum. Nonlinearity coefficient measurements are so called indirect, because the result is calculated from the measured input and output optical powers according to the created equation:

$$P_3(L) = \eta(\Delta\beta)(\gamma P_1(0)L_{eff})^2 P_2(0)e^{-\alpha L} \tag{4.5.9}$$

where P_1 pump power, P_2 signal power, $P3$ idler power, η FWM efficiency, $\Delta\beta$ phase mismatch, γ nonlinearity coefficient, L_{eff} effective length, α attenuation coefficient. From here, it can be seen that nonlinearity coefficient measurements also require other fiber parameters. Therefore full fiber characterization is achieved that is necessary for the selection of the most appropriate fiber for data transmission over WDM-PON network. Experimental measurement method validation was performed on three different optical fibers: Corning SMF-28 ultra optical fiber, Draka enhanced single-mode optical fiber and highly nonlinear fiber. Obtained results have shown that measured values of the nonlinear coefficient are 0.78 $W^{-1}km^{-1}$ for SMF-28 fibers, 1.45 $W^{-1}km^{-1}$ for enhanced single mode fiber and 10.68 $W^{-1}km^{-1}$ for highly nonlinear fiber that conforms to typical values. From all fibers under test the SMF-28 fiber fits the best for the WDM-PON network since it has the lowest nonlinearity coefficient.

4.5.5 Conclusions

- From the analysis of network topologies, it was concluded that passive optical network transmission technology (PON), supplemented by wavelength division multiplexing (WDM), is the most suitable for metro and access network level, that corresponds to the scale of the urban network and provides a high degree of branching. Consequently, the WDM-PON network was selected as the most appropriate technological solution for smart city data transmission, and further research was related to the analysis of various individual system components.

- The spectral efficiency of the frequency band can be increased up to two times if for channel separation in mixed line rate (MLR) WDM-PON instead of the fixed DWDM grating described in the ITU-T recommendation the improved grating with unequal frequency intervals is used. The increase in spectral efficiency depends on the initial system configuration that determines the data transmission rate and modulation formats in different channels (at different wavelengths).
- Apart from the used configuration of the mixed 1040100 Gbps WDM-PON, there is also the point of equal energy efficiency determined by the number of 10 Gbps NRZ-OOK channels, by the energy efficiency of 40 Gbps and 100 Gbps transponders, and by the length of fiber-optical link according to which a definite quality of the received signal must be guaranteed.

Main scientific results:

1. An improved fixed DWDM grid for separation of central frequencies of transmission channels has been developed, which allows to increase the spectral efficiency of the bandwidth used for transmission in WDM-PON solutions.
2. By means of the proposed scheme for allocation of 10 Gbps, 40 Gbps and 100 Gbps transmission channels the relationship has been determined between the spectral efficiency (bps/Hz) in the frequency band, the average power consumption per bps transmitted (i. e., energy efficiency, J/bit) and the overall transmission distance in the 10-40-100 Gbps WDM-based FOTS.
3. Technological solutions of 8 and 16 channel SS-WDM PON systems with the transmission speed of up to 10 Gbit/s in a channel have been developed enabling them to be fully integrated in the existing optical access networks, based on ITU-T G.694.1 frequency plan.
4. The application of the semiconductor optical amplifier has been evaluated in increasing the data transmission speed from 2.5 to 10 Gbit/s in 16-channel spectrum sliced WDM-PON systems.
5. A multichannel light source that doubles the originally available wavelength range and is applicable in WDM-PON networks has been developed. It is based on a fiber optical parametric amplifier and its main elements are high-nonlinear fiber and two high-power pumping lasers. The light source model created as a result of the research makes it possible to double the initial number of 16 low-power laser spectral components to up to 32, by using the idle components created by four-wave-mixing nonlinear optical effect. Consequently, the efficiency of each laser increases twice. This is

explained in more detail in the following article: *S.Olonkins FOPA Pump Phase Modulation and Polarization Impact on Generation of Idler Components,* published in the journal Elektronika ir Electrotechnika, Vol.77, No.4, 2016, pp. 77-81, ISSN 1392-1215, included in the SCOPUS database.

6. The measurement method of nonlinearity coefficient, based on the four-wave-mixing nonlinear optical effect, was experimentally tested. Such a measurement method can be used to evaluate the most important parameters of the optical fiber. Fiber attenuation and dispersion measurements are required to calculate the nonlinearity coefficient by using optical input and output power of optical fiber. Such an analysis of optical fiber parameters is needed to find the most suitable fiber for data transmission in WDM-PON optical transmission systems. This is explained in more detail in the publication: *I.Lavrinoviča Evaluation of Effective Area and Nonlinearity Coefficient of Erbium-Ytterbium Doped Optical Fibers, published in full text conference proceedings: Progress in Electromagnetics Research Symposium (PIERS 2016): Proceedings, China, Shanghai, 8-11 August, 2016. Shanghai: The Electromagnetics Academy, 2016, pp.1-5. ISBN 78-1-934142-30-1* and presented in conference: *S.Spolitis Different Optical Fiber Nonlinear Coefficient Experimental Measurements. Proceedings of 6th International Workshop on Fiber Optics in Access Networks (FOAN 2016), 4 p., Lisbon, Portugal, 2016.*

7. Developed WDM-PON access communication system with a completely optical channel add-drop module in optical line section (see Fig. 4.5.15), which provides solution for a transmission system expansion and/or branching and adding of new subscribers or services with passive (does not require power supply) optical elements without conversion from optical to electrical signal. Optical channel add/drop module (OCADM) is located in optical line section and is based on the Fiber Bragg Grating (FBG) optical filter (Fig. 4.5.15 Element 11.2) and two optical circulators (Fig. 4.5.15 elements 11.1 and 11.3). The use of this filter allows simultaneously separate necessary wavelength channel from the WDM signal and at the same time add to WDM system new signal in the same wavelength channel. Application of such a multiplexer is to add new subscribers to existing optical cable infrastructure (separating channel from WDM system) as well as to expand the applicability of optical access networks, for example, by transmitting various sensor data (adding new signals to WDM system). For this invention the Republic of Latvia patent No. 15276 *WDM-PON Transmission System with All Optical Channel Add-Drop Function* was obtained.

4.5.6 Summary

From the results of the project the following should be highlighted:

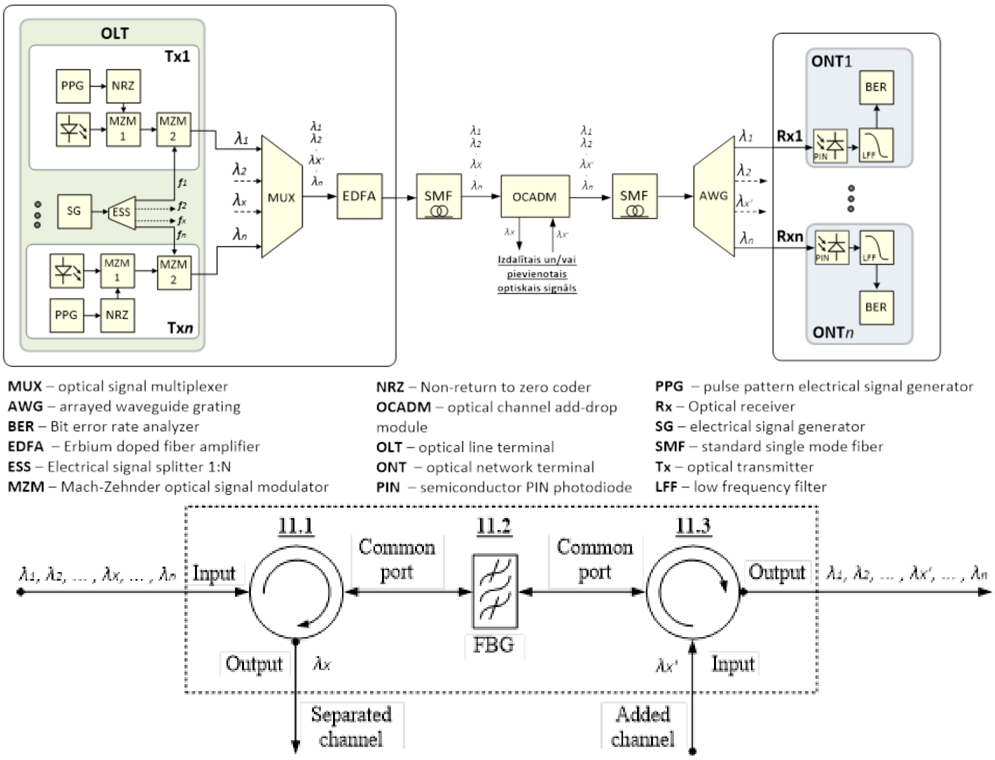

Figure 4.5.15: Developed WDM-PON access communication system with a completely optical transmission channel add-drop multiplexer in optical line section

1. Developed multi-channel light source has a high potential for use in WDM-PON access systems. In such systems each of end users need a light source with a certain wavelength. Accordingly, as the number of end-users increases, it is necessary to increase the number of light emitting sources. Respectively, transmission system maintenance becomes more complex because wavelength control of each light source must be carried out. In addition, laser diodes and lasers has a certain lifetime after which their parameters did not match the initial technical specification provided by the manufacturer and must be replaced. Therefore, in the optical access networks which are characterized by the tree type branching topology very promising are light sources which allows to generate multiple wavelengths at the same time and each of them is further used for data transmission. RTU TI proposed solution allows amplifying the power of initial lasers light at the same time doubling the number of transmission channels. Therefore each light source efficiency is at least twice higher than in the traditional solution where each light source is used for transmitting one data signal;

2. The add/drop multiplexer is necessary to connect sensors to an optical fiber infrastructure. This application is very topical in the context of smart cities because remote sensors and automated monitoring systems is one of

> the upcoming development directions that goes under Internet of Things (IoT) and Tactile Internet (TI) concepts. It will have a marked impact on business and society, introducing numerous new opportunities for emerging technology markets and the delivery of essential public services. That would make possible to provide such a services like remote control video surveillance systems, security systems, environment pollution monitoring systems, etc. in various locations where fiber infrastructure is available.

As a result of the research performed by RTU TI scientists, a prototype of add/drop multiplexer has been created and tested in the laboratory environment. The future work would be to create optimized (size, performance, costs, etc.) component that could be tested and eventually applied in real working conditions.

During the project: 2 doctoral and 14 master thesis were defended, 10 scientific publications were prepared, 6 Latvian patents were obtained, and the results were reported at 7 conferences.

Chapter 4.6

RTU WRL group: Development of the bacteriological quality monitoring system for city water supply system

Research goal: to develop a model of the quality control in a water supply system for protection against intentional or unintentional bacteriological contamination.

List of tasks:

1. A literature analysis about the existing methods and technologies used for drinking water on-line monitoring, data analysis and interpretation tools;
2. Tests of different methods in batch experiments, which could be used for drinking water network monitoring, and testing the feasibility of biological methods as the reference. Optimization of the methods where it is necessary;
3. Design and installation of the lab-scale experimental drinking water supply network;
4. Development of hydraulic model for lab-scale drinking water supply system;
5. Development of drinking water quality modeling tool for predicting drinking water quality in drinking water supply system;
6. Experiments in lab-scale and real scale drinking water supply system;

7. Experiments within pilot scale drinking water supply system by simulation of contamination events to evaluate the efficiency of drinking water on-line monitoring and early warning system;
8. Development of the algorithm for drinking water contamination event detection and alarm triggering;
9. Long term drinking water quality monitoring at drinking water consumption point.
10. Verification of event detection and alarm triggering algorithm by the measurements in pilot scale drinking water supply system;
11. Implementation of event detection and alarm triggering algorithm in on-line drinking water quality monitoring system;
12. Approbation of drinking water bacteriological quality monitoring system in real scale network.

4.6.1 Introduction

Drinking water quality monitoring is a vital tool to ensure good drinking water quality. The aim of this project was to develop an early warning monitoring system for drinking water supply network, which should warn the water utilities in case of drinking water quality deterioration, thus helping to prevent further distribution of contaminated water and reduce potential risks. In this study, detection of biological contamination was chosen as a primary risk, because most of the reported outbreaks are related to the sources of biological origin (WHO, 2014). Biological contamination of various types and sources could enter DWDS. The reasons of this could be as following: failure at the water treatment plant, pipe breakage/leakage, growth of bacteria, biofilm bacteria proliferation, and deliberate contamination. The existing drinking water microbiology monitoring methods, which are usually applied at water utilities worldwide, have severe limitations. For example, heterotrophic plate count (HtPC) method is based on bacteria cultivation on the growth media and counting the colonies subsequently. Although the method undoubtedly indicates on viable bacteria, less than 1% of indigenous water bacteria are cultivable by this method. The long time required for analysis (up to two weeks) ([38]) is another important disadvantage of the method. Several emerging methods have a potential to be used for the assessment of biological quality, however, the new technologies are usually rather expensive and could require experienced operators that are not always available in rural areas. Nowadays the legislation regulates drinking water monitoring procedure and frequency in most of the developed countries; normally it is not required to perform sampling in a drinking water distribution network more often than once per day. Apparently, in a worst-case scenario of the system failure this could lead to distribution of unnoticed contamination to customers. Moreover, rather high level of distrust of the drinking water quality exists within society, which asks for more reliable monitoring technologies. On-line drinking water quality monitoring system could be a solution of these problems. Its ability to measure various water quality parameters with a time step of 1 minute allows to provide much more data, which should minimize the probability to overlook contamination, and therefore society could change the opinion on safety of drinking water.

4.6.2 Literature studies and background

Extensive literature analysis was performed during the first period of the project to understand the latest achievements in on-line drinking water monitoring methods, tools and data analysis. The information obtained from these sources was analysed, summarized and presented as a state-of-the-art report. The publication *Review of Existing and Emerging Biological Contamination Detection Tools for Drinking Water Distribution Systems (DWDS) Online Monitoring* (Appendix 4.2) was submitted for the IWA 7th Eastern European Young Water Professionals Conference (Belgrade, Serbia 17 19 September) where it was presented with an oral presentation and published in conference proceedings. In short, the microbial and general contamination events detection methods have been discussed regarding possible application in DWDS water quality monitoring. The principle of event detection system operation has been reviewed in detail. It was concluded that choice of water quality parameters used for analysis by an as well as adjustment and configuration of event detection software is critical.

The most promising combination of parameters for contamination detection has been selected: temperature (T), electrical conductivity (EC), total organic carbon (TOC), chlorine ion (Cl-), oxidation-reduction potential (ORP), tubidity and pH sensors. Besides on-line physically chemical sensors, novel biological methods were used for system validation/comparison with indirect sensors. Namely adenosine tri-phosphate (ATP) and flow cytometric (FCM) measurements were performed.

4.6.3 Testing of different drinking water quality monitoring methods in batch scale and pilot-scale experiments

4.6.3.1 Testing of different drinking water quality monitoring methods in batch scale experiments

The batch tests were conducted to check reproducibility and feasibility of some of the tools and methods, which could be used manually and/or developed as on-line tools. Flow cytometry methods, ATP measurements, chlorine in-situ approach, total organic carbon (TOC) measurements were tested. Chlorine and TOC measurements are chemical water quality parameters, and are often used as sensors in chlorinated drinking water. The measurements of free and total chlorine were tested in the lab with Hach DPD free and total chlorine reagent powder pillow and measured with Hach DR-890 prior the experiments. Standard deviation of the method was 0.01 mg/L for total chlorine, and 0.025 mg/L for free chlorine measurements. However, it was decided not to use this parameter in this study due to very low (under detection limit) chlorine concentration in experimental location. TOC is an important parameter for water quality monitoring. The existing method for TOC determination is based on total carbon (TC) and inorganic carbon (IC) measurements on Skalar FormacsHT analyser. The measurements were performed with autosampler, and the standard deviation of the measurements ranged from 0.11 to 1.74 % for TC and from 0.04 to 0.76 % for IC. ATP, flow cytometry and growth potential tests were meant to describe water biological quality. ATP was chosen as one of the monitoring methods, because it showed the ability to provide some additional information, e.g. extracellular and intracellular ATP ratios, which can be sensitive to water chlorination. The data about ATP behaviour in a presence of chlorine was summarized and interpreted in the research article Behavior and stability of ATP during chlorine disinfection in Water Research journal (Appendix 4.3). Flow cytometry measurements were performed on Partec CyFlow instrument, and two basic methods were tested determination of total cell count and intact cell count. For total cell count SYBR Green I (SG) stain was used for labelling the cells. Intact cell count was determined with SG and propidium iodide (PI) stain (SGPI). The latter was particularly interesting since it shows potentially viable bacteria without cultivation. The method, used for this study, was optimized from the methods described in various sources ([39, 40, 41]). The results obtained in the present study were included in the scientific publication *A pipeline for developing and testing staining protocols for flow cytometry, demonstrated with SYBR Green I and propidium iodide viability staining*, published in Journal of Microbiological Methods (Appendix 4.4). It describes various factors, which could influence methods outcome, including necessity of EDTA addition.

4.6.3.2 Testing of different drinking water quality monitoring methods in pilot-scale experiments

Total cell count (TCC), intact cell count (ICC) and ATP were applied in the pilot-scale system to test the feasibility of the methods and to understand their advantages and limitations in detection of contamination. Flow rate was adjusted to a constant value before the start of the experiment, then flow rate was stopped (Q = 0 m/s) for 20 minutes, and continued again.

The samples for FCM and ATP were taken every 30 min from two sampling points belonging to Station A and Station B. The measurements were proceeded within 2 h from sampling time. The results of the run are shown on Fig. 4.6.1 (FCM data) and Fig. 4.6.2 (ATP). The results show that both methods could be used for microbiological quality characterization. These demonstrate clear difference between points A and B, where the latter has higher ATP, ICC, and TCC values during all observation time, which could be explained by biofilm influence. This also could be a reason why changes in point A were not detected increase of biomass is likely a function of distance, which is particularly interesting and important for potential contamination/system failure localization. FCM

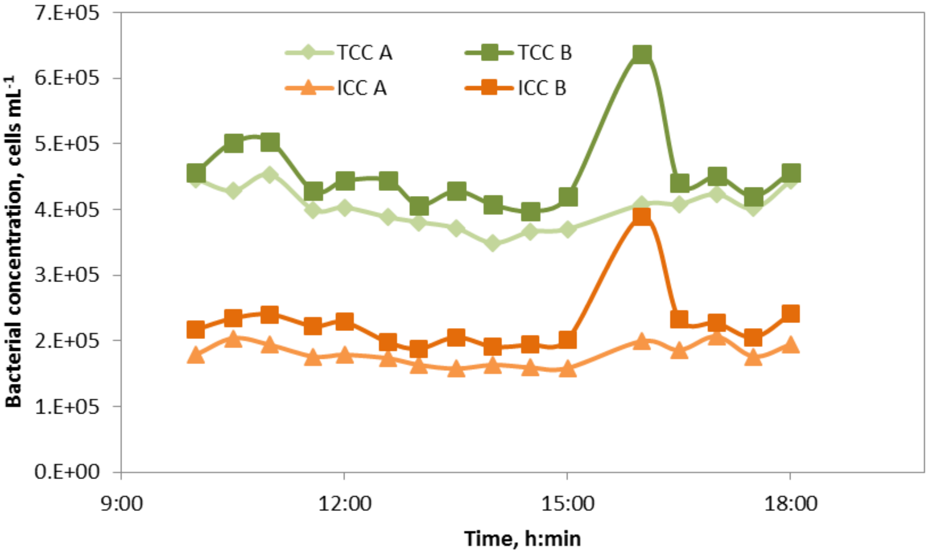

Figure 4.6.1: Changes in TCC and ICC during 8 h monitoring, and a response of these parameters to a change of the flow rate (16:00). A and B indexes correspond to the samples from the Stations A and B.

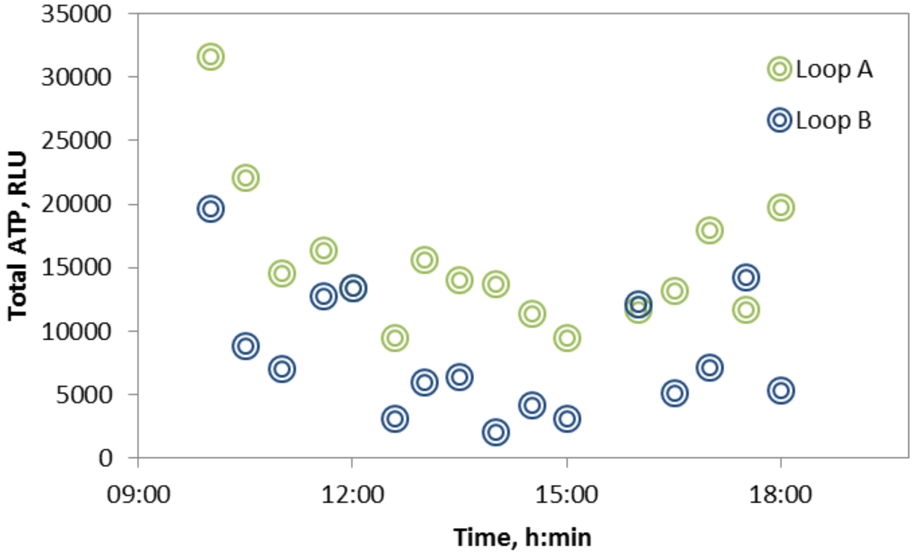

Figure 4.6.2: Changes in total ATP during 8 h monitoring, and a response of these parameters to a change of the flow rate (16:00).

ICC and TCC showed better response to changing flow rate, than ATP measurements. This could be explained by low sensitivity of the instrument for minor bacterial changes (drinking water bacteria normally have low ATP content), or it can be influenced by extracellular ATP. When compared with recently published research article, where extracellular ATP behavior was specifically investigated during water chlorination, the difference with this experiment was that this was a dynamic system and not static, as in the mentioned study ([42]).

4.6.4 Design and installation of the lab-scale experimental drinking water supply system

Based on the literature studies and batch experiments, the lab-scale experimental pilot system was designed. The aim of the system is to reach hydraulic, biochemical and physical conditions that might exist in real DWDS and transfer batch scale experiments in an environment that is more similar to natural conditions in DWDS. The system was designed to meet maximum available size of it and laboratory dimensions (Fig. 4.6.3). The system is equipped with two online sampling points with online sensors for temperature, pH, electrical conductivity (EC), chloride ions (Cl-), oxidation-reduction potential (ORP) and total organic carbon (TOC). The sensors installed in the system are Hanna Instruments Inc., Adrona ltd., Sigrist Inc. production. All of the data collected from the online sampling points are transmitted to the computer where they are processed. An electromagnetic flow meter and 5 pressure sensors with online monitoring were installed to monitor the hydraulic parameters of system. The data from the sensors are processed and stored directly with the personal computer (PC). Data collection frequency is variable, and it is set to 1 reading every 1 - 5 minutes to keep reasonable data amount for a long term monitoring. Inlet water is taken from the public drinking water supply network and outlet water is collected in the 12 m3 underground tank and afterwards discharged in public wastewater system. The system is designed with the possibility to change the flow rate from 0 to 0.6 m/s to simulate the hydraulic conditions as they are in a real scale system. The system pressure is designed that it cannot exceed 1 bar due to sensitivity and operating limits of drinking water quality sensors.

Pilot system parameters:

- pipe length 200 meters (for experimental usage) + 100 meters for supply and waste water;
- pipe diameter 25 mm (inner), 33 mm (outer);
- pipe material PVC (polyvinylchloride);
- water source Riga city DWDS;
- contamination dosage points 1;
- manual sampling points 3;
- sampling points equipped with drinking water quality online sensors 2;

Figure 4.6.3: Lab-scale (pilot scale) DWDS.

- sampling points for hydraulic monitoring 5;
- max designed system pressure 1 bar;
- average designed flow velocity 0.1 m/s;
- average designed hydraulic retention time approx. 30 minutes;
- total volume of experimental piping 98,17 litres.

4.6.5 Development of a hydraulic model for lab-scale DWDS

The hydraulic model for drinking water supply system was developed to achieve the aims of the project and scientific goals. It is a crucial point for the whole system that is going to be developed in terms of project because it is the core for the possible contamination spreading in DWDS. The hydraulic model was designed in open-source code software EPANET 2.0 (provided by US Environmental Protection agency) to ensure that there are possibilities to change the source code and upgrade the model in upcoming tasks. The model was simplified to keep a reasonable data amount that must be obtained and modeled (Fig. 4.6.4).

The values, settings and parameters assumed in hydraulic model:

- Junctions 15;

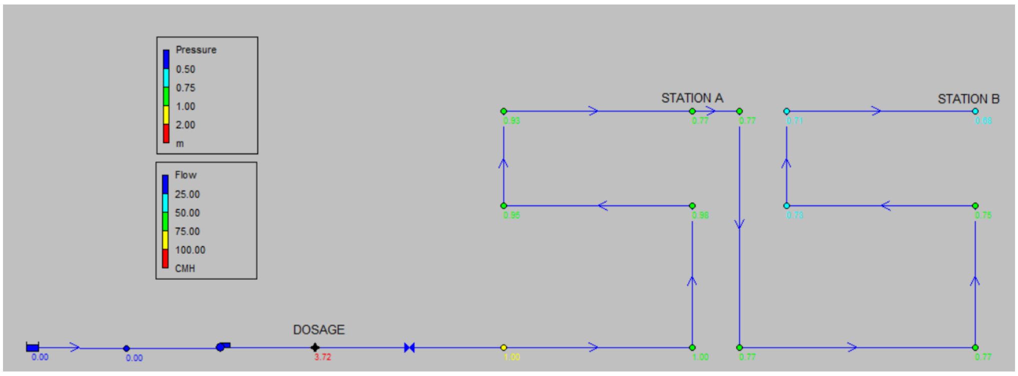

Figure 4.6.4: Lab-scale (pilot scale) DWDS.

- Reservoirs 1;
- Links (pipes) 13;
- Pumps 1;
- Valves 1;
- Headloss formula Hazen-Williams;
- Maximum trials - 40;
- Roughness of PVS pipes 150;
- Hydraulic time step 1 minute;
- Quality time step 5 minutes;
- Total model duration depends on scenario (24 or 120 hours).

The calibration of the hydraulic model was done by using the hydraulic parameters such as pressure and flow. The validation of the model was done by using the drinking water quality parameters, electrical conductivity and water resistance time.

The EC sensors mounted in both station A (after 100 m from beginning of the system) and station B (after 200 m) were used for the system validation. The validation was done for two scenarios: the short term scenario (one day) and the long term scenario (five days), where the measured EC values were used to compare them to the modelled values.

4.6.5.1 Results for a short term scenario validation

An input data of EC was calculated as an average value from long term (2 weeks) monitoring of EC variations to validate the hydraulic model for short term scenario. The EC was monitored on-line and stored as an average value every 5 minutes. The results for the observed EC were monitored for each separate day and compared to results provided by model. The results showed that the Root Mean Square (RMS) value is 64.2 μS/cm and 89.8 μS/cm respectively to Station A and B, and the mean values of 596.4 μS/cm and 589.9 μS/cm. It was concluded that the model of the short term scenario is accurate enough, and validation is done correctly. Results of the validation for station A shown in Fig. 4.6.5.

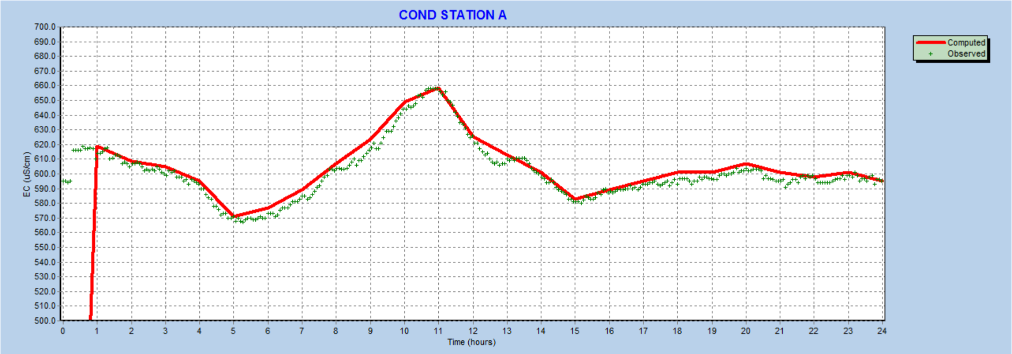

Figure 4.6.5: Validation of hydraulic model for short term scenario.

4.6.5.2 Results for a long term scenario validation

To validate the hydraulic model for the long term scenario, the same input data as in short term scenario was used for the modeling of EC. To validate the model for long term the EC monitoring was done for 5 days at the monitoring station A. The results showed that the Root Mean Square (RMS) value was 49.3 μS/cm at Station A and the mean value was 602.5 μS/cm. Although only one point was used for long term validation, it was concluded that validation was successful for long-term scenario model. Results of the validation at the station A are shown on figures 4.6.6 and 4.6.7.

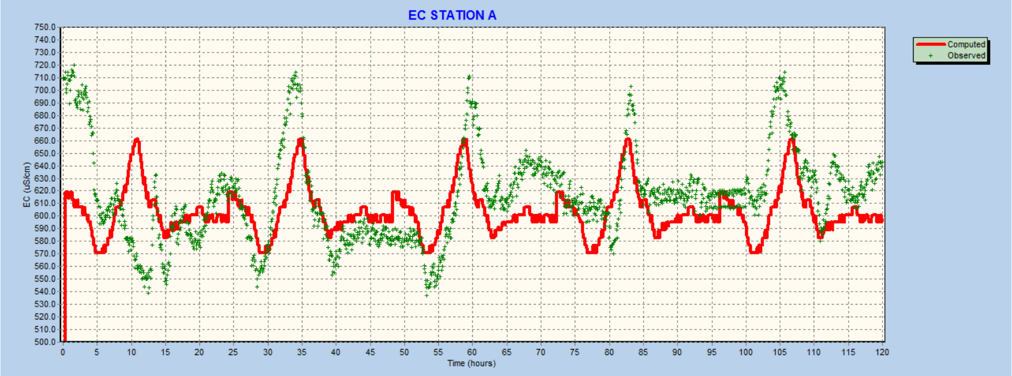

Figure 4.6.6: Validation of hydraulic model for short term scenario.

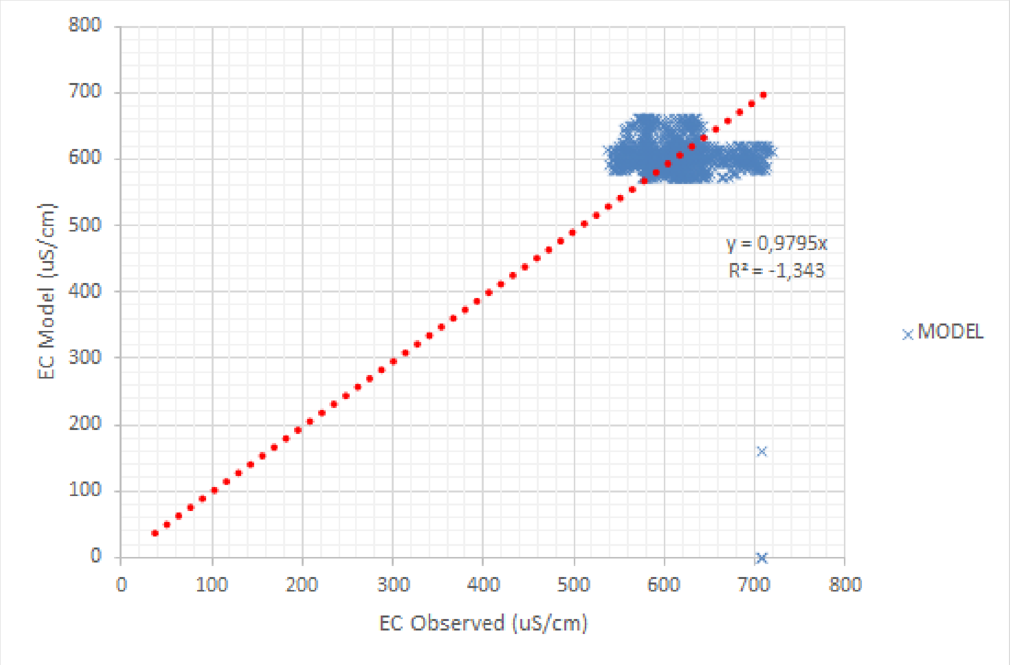

Figure 4.6.7: Validation of hydraulic model for short term scenario.

4.6.6 Development of a drinking water quality modeling tool

A tool for drinking water quality prediction has been made to ensure the possibility to predict the potential contamination spreading in DWDS. The tool is based on the mathematical modeling of drinking water quality at the each point of DWDS. It is incorporated with the hydraulic model of DWDS and made within EPANET 2.0 additional modeling software EPANET-MSX, built by EPA. Model takes into account both the hydraulic parameters of DWDS as well as the chemical (chlorine, organic carbon, etc.) and biological (bacterial regrowth, substrate uptake, etc.) parameters. The equations and principle of the model is based on previous studies of drinking water quality modeling ([43]).

4.6.7 Long-term monitoring of drinking water quality in lab-scale and real scale drinking water supply systems to establish the baseline quality

4.6.7.1 Long-term monitoring of drinking water quality in a lab-scale and real-scale water supply systems with biological method

The real-scale DWDS was investigated for biological data collection with FCM and ATP methods while the measurements in the lab-scale system were limited due to installation and validation activities of the system. The aim of this was to understand behaviour of microbial population during long-term and short-term monitoring. Another experiment was made to test FCM-based and ATP methods on very different samples different steps of the water treatment plants, network samples and to obtain correlations between these two methods. In short, two locations in Riga were chosen for sampling during long-term monitoring campaign. One was supplied from treated surface water, another represented mixed surface and groundwater. Both were used chlorination as a final disinfection. Sampling was performed once per week, during 12 months. One of the sampling locations is in the same building as the pilot system. Though, the reason it was not performed in our experimental system was that it the experiment started before it was ready to use it was started during previous stage of the project as reported before, and lasted for 1 year. The samples were stained with SYBR Green I (SG) and SG and propidium iodide (SGPI), and measured with FCM. Total cell count (TCC) (all bacteria in the samples) and intact cell count (ICC) (bacteria with intact membrane, living bacteria) were determined accordingly. Additionally, sampling was made twice per day during one week, and one day samples were taken from the open tap every 30 min during 12 h within this week. Clear seasonal variations in TCC and ICC were observed in the drinking water distribution network samples over 12-months (n = 48). One-year monitoring showed that TCC values of the DN sample that originated from treated surface water varied from 0.67 to 5.87 x 10^5 cells mL^{-1}, with a mean value 2.75 ± 1.41 x 10^5 cells mL^{-1} (CV = 51 %) (n = 48) (Fig. 4.6.8A), and ICC values were from 0.1 3.75 x 10^5 cells mL^{-1}, with a mean value 1.46 ± 0.95 x 10^5 cells mL^{-1} (CV = 65 %) (n = 48). Interestingly, generally higher bacterial concentrations were observed during warm time of the year: all ICC and TCC values, which were higher than the average, occurred in a time period from May to October, and were lower in the rest time of the year, following similar trend as a temperature at the treatment plant.

TCC and ICC values of the mixed sample were different from the surface water sample and showed less seasonal dependency. TCC was from 1.98 6.76 x 105 cells mL^{-1} (mean = 4.41 ± 1.36 x 105 cells mL^{-1} (CV = 31 %) (n = 48)) (Fig. 4.6.8B), and ICC values varied from 0.44 x 105 4.37 x 105 cells mL^{-1} (mean = 2.20 ± 1.05 x 105 cells mL^{-1} (CV = 48 %) (n = 48)), thus both TCC and ICC were significantly different from the first sample ($P \leq 0.05$). Differences between warm and cold seasons were not as clear as in the example of surface water sample, however, clearly lower TCC and ICC were observed in a period from mid-January until April. Temperature in the tap was from 11.5 to 19.3 °C during all observation period, and relatively weak correlations between tap water temperature and TCC ($R^2 = 0.56$) and ICC ($R^2 = 0.49$) (Fig. 4.6.9) were obtained.

Figures 4.6.10 and 4.6.11 show that minor changes could happen during short-term monitoring, and this is especially dependent on water consumption regime. It is not so obvious on 1-week experiment: only slightly higher numbers in morning hours. However, clearly lower numbers were detected on Tuesday afternoon and Wednesday samples. This is strongly related with 12 h continuous experi-

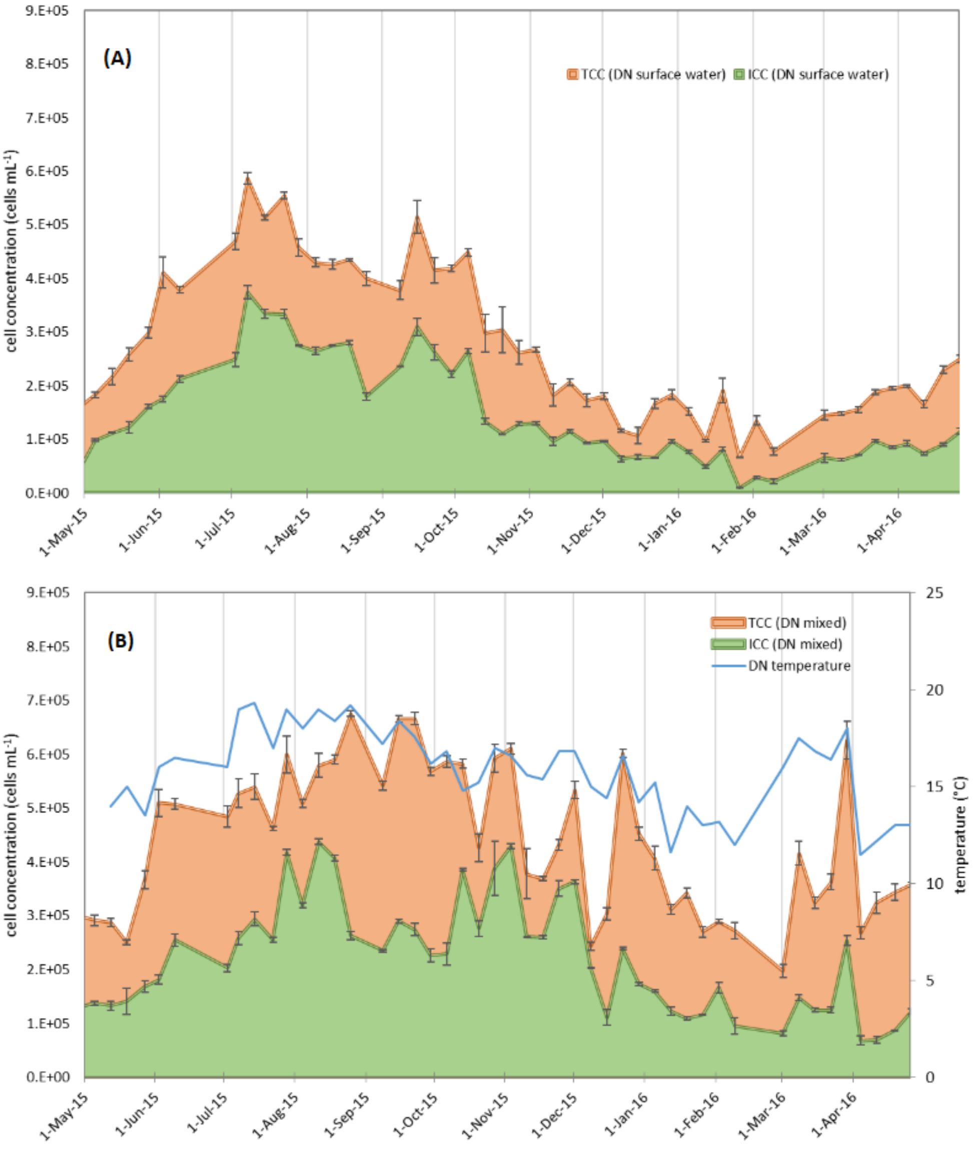

Figure 4.6.8: Temporal bacterial cell variations over long-term monitoring of the drinking water distribution network (DWDS) sample, which was originated from treated surface water (A) and surface water, which could be potentially mixed with groundwater (B) (n = 48). (B) sample was taken in the university campus building, and temperature was measured as well.

ment, which took place exactly on Tuesday (Fig. 4.6.11). Both TCC and ICC gradually decreased for almost 20 % in 12 h. We explain this with two processes: flushing of stagnated water and bacteria detachment from biofilms due to increased water flow. Hereby lower TCC and ICC were observed the next day. However, cell numbers reached initial concentrations by the end of the week that

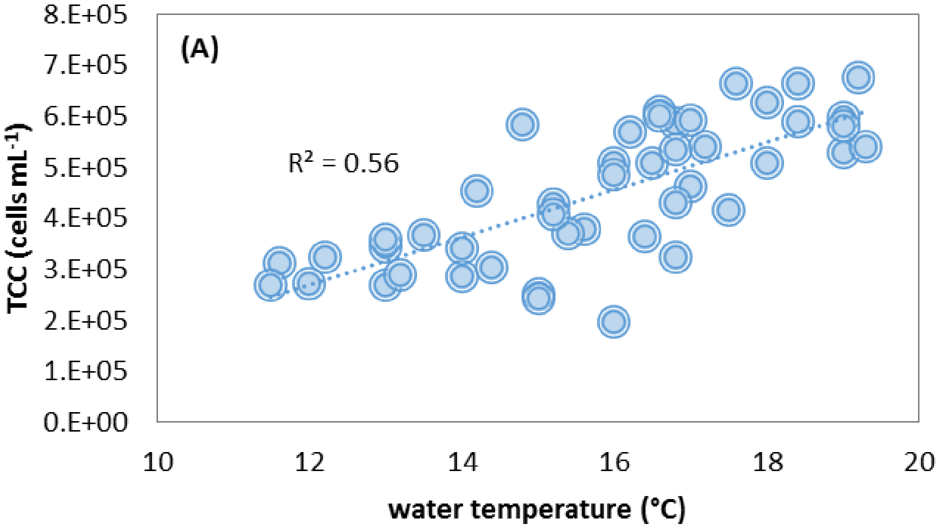

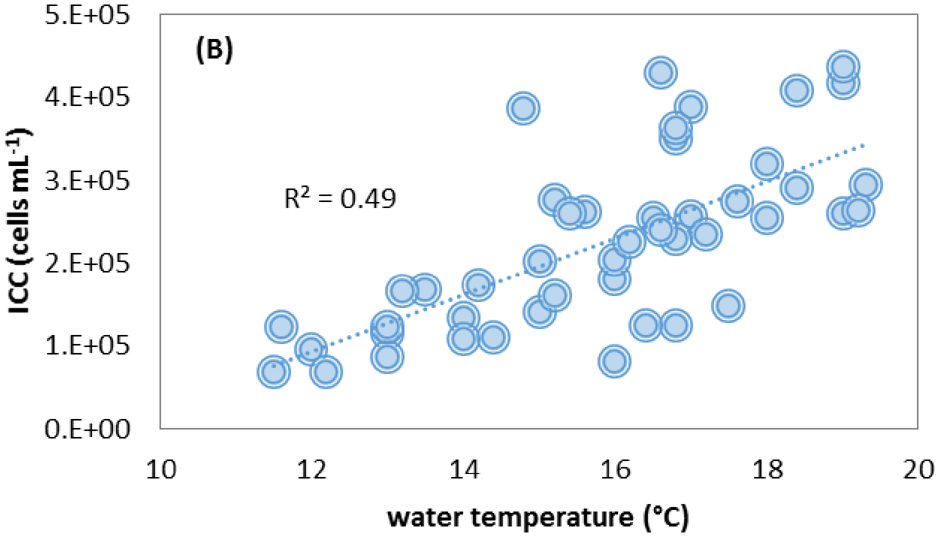

Figure 4.6.9: Correlations between DWDS water temperature and total cell count (A) and intact cell count (B) (n = 46).

probably means that bacterial growth occurred.

The data obtained during this study was presented at RTU 57th international scientific conference in the Heat, Gas and Water Technology subsection (12th October, Riga, Latvia) and IWA Microbial Ecology in Water Engineering & Biofilms 2016 (4-7th September, Copenhagen, Denmark). A scientific publication *Identifying the underlying causes of biological instability in a full-scale drinking water supply system* was submitted to Water Research journal. Moreover, these data represent be the main part of the last chapter of doctoral thesis of Neščerecka A. *Biological Stability in Chlorinated Drinking Water Distribution*

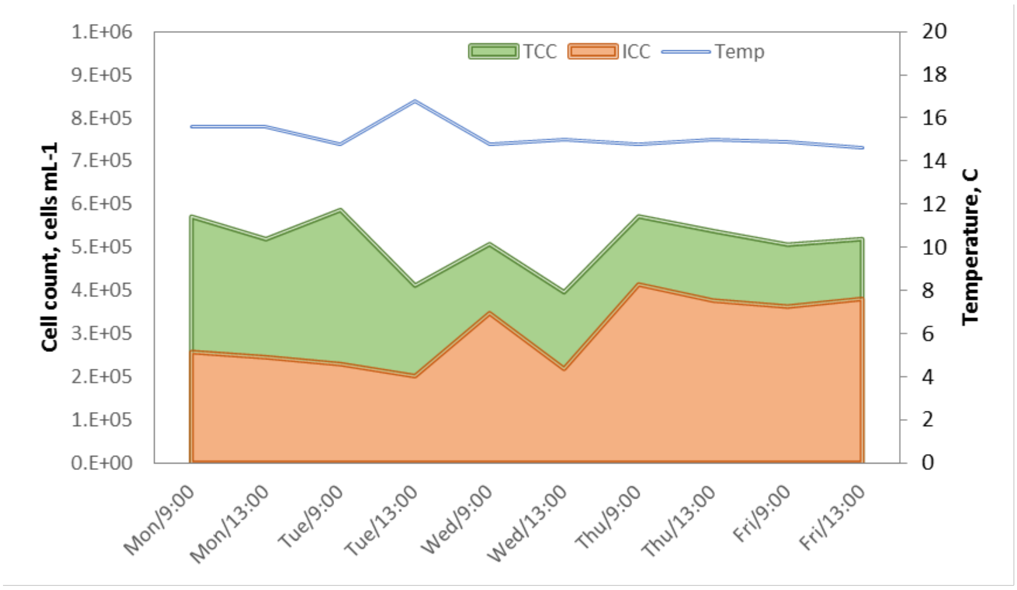

Figure 4.6.10: Changes in TCC and ICC determined in morning and afternoon hours twice per day.

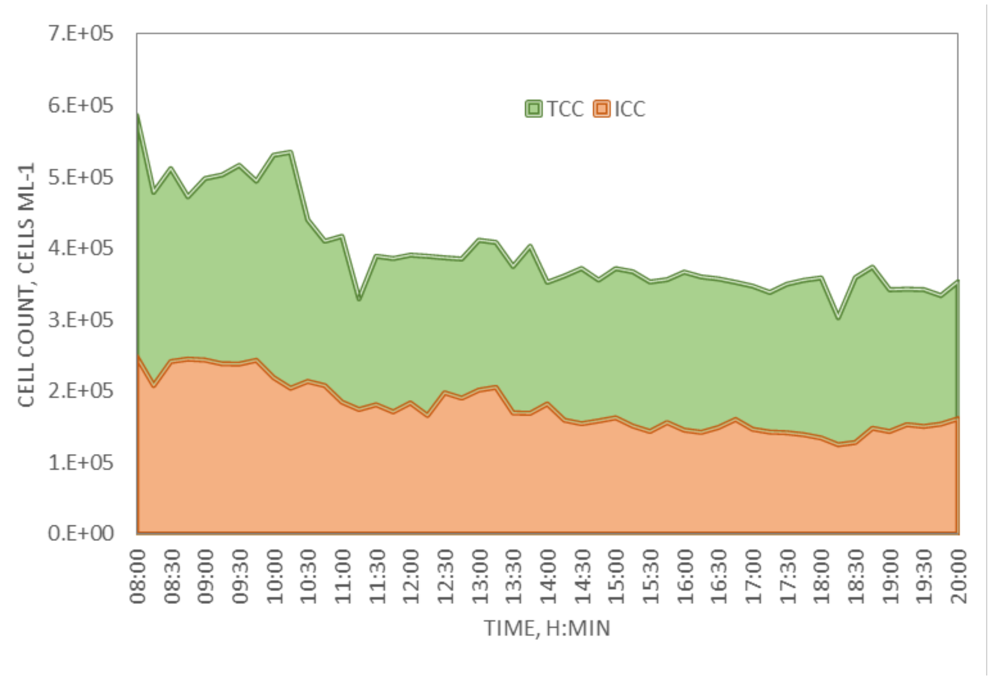

Figure 4.6.11: Changes in TCC and ICC in continuously running water, measured every 30 min during 12 h.

Networks defended in 2017 (summary of thesis Appendix 4.5).

4.6.7.2 Long-term monitoring of physiochemical drinking water quality parameters in a pilot-scale and real scale drinking water supply systems

The existing legislation regulates that the drinking water quality monitoring tests more often than once a day at different points of distribution network. This water quality monitoring approach has a huge drawback that there are no daily or hourly quality changes analyzed. This might be a crucial issue during the contamination events described in previous chapters. Long term data is crucial to establish the drinking water quality parameters in clear water conditions the baseline for contamination detection algorithms. For better understanding of drinking water quality variations due to hydraulic conditions in distribution network, caused by temporal water consumption fluctuations, an intensive drinking water quality monitoring measurements were done. The measurements were done in the pilot scale system located in laboratory of Riga Technical University Water Research Laboratory and in the real scale distribution network of Riga city. The pilot scale system is described in the chapter 4.6.4. Temperature, pH, electrical conductivity (EC), Cl ions (Cl-), oxidation-reduction potential (ORP), total organic carbon (TOC) and turbidity were measured in the system. Drinking water was monitored during 7 months with a time step of 1 minute. During the last months of studies a turbidity sensor was installed at the measurement station B. So far, the total amount of readings in studies is more than 3 500 000. However, the large amount of collected data led to an issue on data collection and analyzing system. The system should be improved and implemented in MATLAB environment, which would allow doing on-line analysis of data and also improving the collection and saving of data. For example, less relevant data in normal case situations might be stored every 10-15 minutes; however, data from contamination or drinking water quality variation periods might be stored with a time step of 1 minute. This approach might reduce the stored data amount by 10-15 times. Fluctuations of drinking water parameters were observed during long-term monitoring. Changes in EC during 11 weeks are demonstrated in Fig. 4.6.12, where data are plotted against calendar week. Although completely stable results were not expected, weeks 4, 5, 8 and 10 show more extreme variations than the rest. Hourly, daily or weekly variations were analyzed, but no correlations have been found, and the cause of these variations is not evident. However, most likely it is related to hydraulic conditions in the network. For example, changing water consumption would lead to water stagnation in the distribution network, or vice versa delivery of fresh water from the water treatment plant. Moreover, the studied DWDS is supplied from both treated surface water and groundwater, which have different initial parameters, thus changes in water consumption could lead to different incoming water, or distribution of water from water reservoirs, which are used in Riga DWDS for compensation of drinking water consumption fluctuations.

Due to ability of on-line monitoring system to observe different patterns of drinking water quality, a systematic change of water parameters was detected. An example of such a pattern for temperature measurements is demonstrated

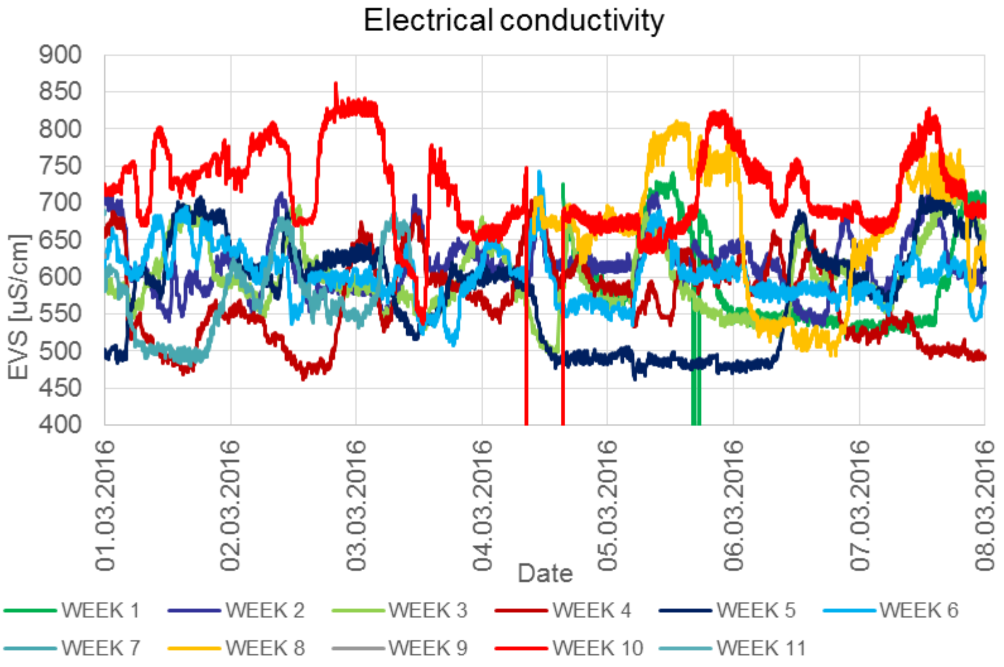

Figure 4.6.12: Fluctuation of electrical conductivity during long term monitoring.

on Fig. 4.6.13. Drop of temperature was observed every Monday, Wednesday and Friday morning during all monitoring period (11 weeks). Importantly, no correlations with internal or external air temperature were found, which indicates that it is not caused by warming/cooling due to external environment. The plausible explanation is regular changes of water consumption in a large industrial/public building nearby. In our case it could be related to a sport hall with a large swimming pool situated near by the laboratory (≈ 100 m), where is generally high water consumption and this could be linked to the regular maintenance. For example, water recharge causes the increase of water flow/velocity, and supply with water with lower water retention time subsequently, which leads to lower water temperature at monitoring point.

This finding highlights the advantages and potential of continuous on-line monitoring. It is particularly important to understand systematic changes of drinking water parameters, and consider those, when defining a baseline for the early-warning system. Detection of new correlations and proofs of local hydraulic influences on drinking water quality what might lead to influence to decent area of DWDS. Long term on-line drinking water quality monitoring provides a new possibility for water utilities to understand water quality variations and determine the health of DWDS. Results of the first steps in long term monitoring are summarized in article Dejus S., Rusenieks R., Nescerecka A., Nazarovs S., Juhna T., (2016) *Long Term Drinking Water Quality Monitoring in Drinking Water Supply Systems by On-Line Sensors* (Appendix 4.6). Results were also presented

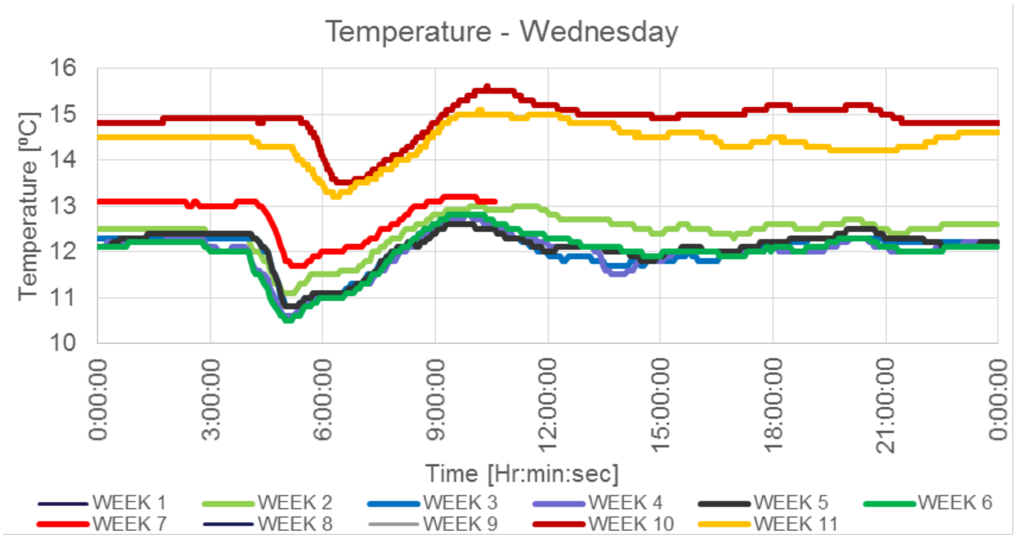

Figure 4.6.13: Diurnal fluctuations of temperature on Wednesdays during long term monitoring. Similar patterns were observed for Mondays and Fridays (not shown). Temperature was stable during other days of the week.

in RTU 57th International Scientific Conference and IWA 8th Eastern European Young Water Professionals Conference. the demonstration of pilot scale drinking water supply system and on-line drinking water quality monitoring system to professionals of water sector was carried out during the RTU 57th International Scientific Conference (Drinking Water Quality Monitoring and Safety of Drinking Water Supply Network). During the long-term studies the baseline for contamination detection algorithm has been established.

4.6.8 Development of algorithm for drinking water contamination event detection and alarm triggering

To identify and select the most promising drinking water system contamination event detection algorithm 11 algorithms for detection of contamination event compared. The evaluation of various algorithms has been summarized in scientific paper *On-line Drinking Water Contamination Event Detection Methods* (Appendix 4.7) and presented in Environment. Technology. Resources conference (Rezekne, Latvia, 15-17 June, 2017).

Literature studies showed that cluster analysis based on Mahalanobis distance ([44]) is the most promising tool not only to make an early warning system alarm algorithm, which might be supported by algorithms using Euclidian distance ([45]), Pearson correlation and Euclidean distance ([46]), canonical correlation analysis method ([47]), but also a contamination classification tool. It means that this approach solves two tasks simultaneously and it was chosen to accomplish these tasks.

Each measurement set obtained in a particular time step forms a data set, which might be called an object. Following this notation, the term 'instance' refers to the object from pre-defined class while 'sample' refers to the object to be classified. Both instance and sample are multidimensional vectors ([48]). In our case 6-8-dimensional vector analysis is performed. A distance is a real-valued function that quantifies the similarity between two objects. The Mahalanobis distance is a unit-less value that provides a relative measure of a data point‘s similarity with the set of instances representing a class, which can then be used to identify and gauge adherence of a sample to the class.

Contaminant classification is done by analyzing the distance from it to a class c in k-dimensional space:

$$D_{pcM}(p, c) = \sqrt{(p - \mu c)^T S^{-1} (p - \mu c)} \tag{4.6.1}$$

, where DpcM is the distance from a point to a class; μc and S are the mean and covariance matrix of all instances in class c. Assuming there are n classes of water, c1, c2, , cn, any sample p is identified to belong to class i, if

$$D_{pcM}(p, c_i) < D_{pcM}(p, c_j), j = 1, 2, 3, ..., n; i \neq j \tag{4.6.2}$$

In the alarm triggering procedure, the Mahalanobis distance from a sample taken in every time step is calculated to the 'normal' base line class. If this distance exceeds the chosen threshold value, the alarm is triggered. If the distance shows that a sample belongs to one of contaminant classes rather than the 'normal' class, corresponding alarm level is triggered, based on the threat and size of the risk to health of society.

4.6.9 Experiments within pilot scale drinking water supply system by simulation of contamination events to evaluate the efficiency of drinking water on-line monitoring system

The purpose of drinking water quality monitoring and early warning system is to detect deliberate and accidental contamination. It is very important not only to detect the contamination but also classify the type of contaminant to determine the possible sources and causes of contamination and handle the situation correspondingly. Each kind of contamination might raise different risks to drinking water consumer and that leads to different action plans for each kind of contaminant. The experiments were conducted in previously constructed pilot scale drinking water supply system. The data were acquired with on-line drinking water quality monitoring system; the parameters with highest deviations during the contamination events were determinate.

4.6.9.1 Simulation experiments of contamination events (primary)

Although numerous chemical compounds are regulated for drinking water safety, legislative requirements for microbiological water quality are limited by only few indicator organisms, and total heterotrophic bacteria counts, which should be assessed by cultivation-based methods, which in turn have certain limitations. Moreover, biological contamination has higher impact on health in comparison with chemical water quality deterioration ([49, 50, 51, 52], thus ideally biological contamination should be detected as soon as possible. Five contamination event scenarios in total were carried out (Fig. 4.6.14), which aimed to detect the possible biological contamination events. To evaluate the capacity of on-line monitoring system to detect the possible drinking water contamination events, numerous pilot scale experiments were done. Dilution of contaminant was assumed as 10% of drinking water flow in system. Temperature, pH, electrical conductivity (EC), chloride ions (Cl-), oxidation-reduction potential (ORP) and total organic carbon (TOC) were monitored in two measurement points with a time step of 1 minute to detect the possible contamination events. Also adenosine triphosphate (ATP) and flow cytometry measurements (FCM) of total and intact cell counts were conducted with a time step of 5 and 10 minutes (depending on the phase of experiment). Each contamination event was 15 minutes.

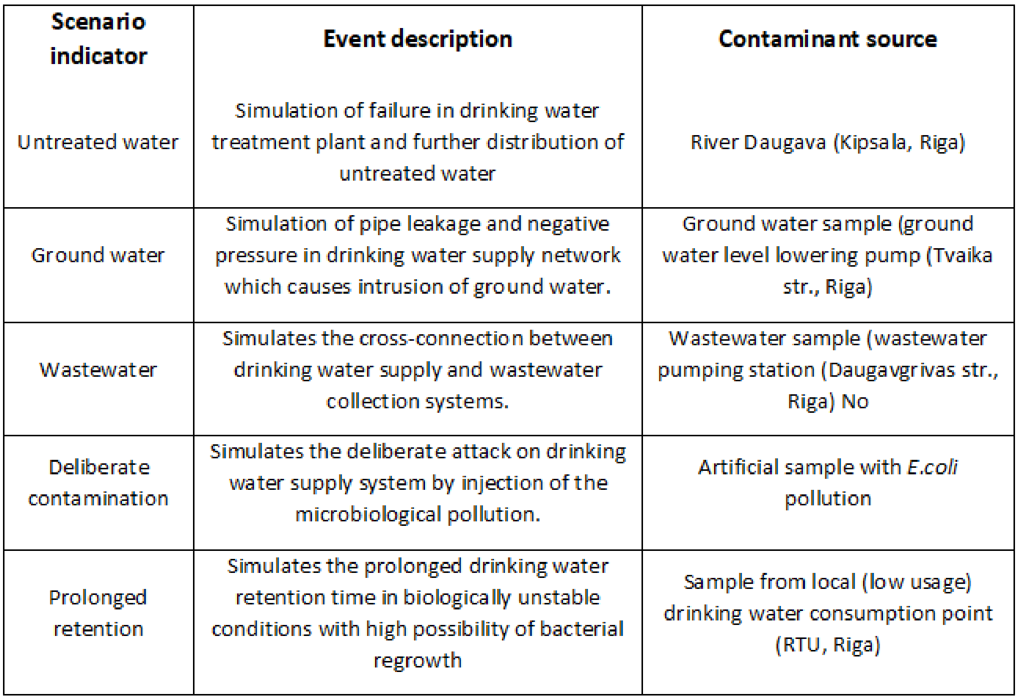

Scenario indicator	**Event description**	**Contaminant source**
Untreated water	Simulation of failure in drinking water treatment plant and further distribution of untreated water	River Daugava (Kipsala, Riga)
Ground water	Simulation of pipe leakage and negative pressure in drinking water supply network which causes intrusion of ground water.	Ground water sample (ground water level lowering pump (Tvaika str., Riga)
Wastewater	Simulates the cross-connection between drinking water supply and wastewater collection systems.	Wastewater sample (wastewater pumping station (Daugavgrivas str., Riga) No
Deliberate contamination	Simulates the deliberate attack on drinking water supply system by injection of the microbiological pollution.	Artificial sample with *E.coli* pollution
Prolonged retention	Simulates the prolonged drinking water retention time in biologically unstable conditions with high possibility of bacterial regrowth	Sample from local (low usage) drinking water consumption point (RTU, Riga)

Figure 4.6.14: Description of experimental drinking water contamination events.

To achieve conditions that might be implemented in real scale situation, the hydraulic and physical parameters of drinking water supply system were following: flow 0,21 m^3/h, flow velocity 0,1 m/s, pressure 1 bar. The initial experimental results showed that set of sensors installed in pilot scale drinking water supply system have observable parameter deviations and is capable to detect the contamination (Fig. 4.6.15) Example of measurement results from one sensor during the scenario with groundwater is shown in Fig. 4.6.16. The results from initial contamination simulation experiments are summarized in extended abstract *Drinking Water Contamination Detection by On-line Monitoring: Pilot Scale Studies* (Appendix 4.8) and presented in 9th IWA Eastern European Young Water Professionals Conference, Budapest, Hungary, 24-27 May, 2017.

Scenario indicator	**On-line monitoring**					**Analysis**		**Total**
	TOC	**pH**	**Cl**	**ORP**	**EVS**	**ATP**	**FC**	
Prolonged retention (B)	0	1	1	1	1	1	1	6/7
Prolonged retention (A)	0	1	1	1	1	1	1	6/7
Untreated water (B)	1	1	0	1	0	1	1	5/7
Untreated water (A)	1	1	0	1	0	1	1	5/7
Ground water (B)	1	1	0	1	1	1	1	6/7
Ground water (A)	1	1	0	1	1	1	1	6/7
Wastewater (B)	1	0	0	1	1	1	1	5/7
Wastewater (A)	1	0	1	1	1	1	1	6/7
Deliberate contamination (B)	-	0	0	1	1	1	1	4/6
Deliberate contamination (A)	-	0	0	1	1	1	1	4/6

Figure 4.6.15: Evaluation of contaminant detection by the set of sensors (A measurement station after 100 m, B measurement station after 200 m, 1 parameter deviation observed, 0 parameter deviation not observed, - sensor out of service.

4.6.9.2 Simulation of contamination events and classification of the most possible drinking water supply system contaminants

After the primary experiments and evaluation of results and shortages of study, the new experiments in pilot-scale drinking water supply system were accomplished. During the new session of contamination experiments more sufficient grab sampling and manual analyses of drinking water quality have been done. The study and results have been compiled and submitted as a scientific pub-

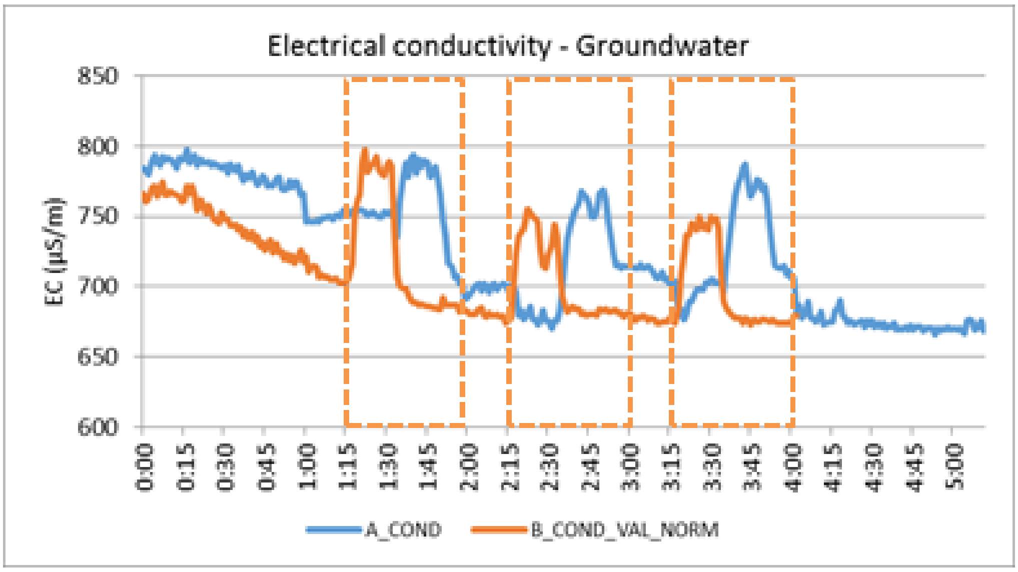

Figure 4.6.16: Changes of electrical conductivity over time during 3 contamination event repetitions.This example represents groundwater intrusion scenario, sensors measure electrical conductivity, where A_COND measurements after 100 m, B_COND measurements after 200 m, dashed lines indicate contamination events.

lication *Detection of Drinking Water Contamination Event with Mahalanobis Distance Method, Using On-line Monitoring Sensors and Manual Measurements Data* in journal Water Science and Technology: Water Supply (21.12.2017) and will be published. To evaluate the ability of contamination detection by on-line and grab sample monitoring, a performance test was done. It consisted of calculation of true positive rate (TPR) and false positive rate (FPR) values by:

$$TPR = \frac{TP}{TP + FN} \tag{4.6.3}$$

$$PR = \frac{FP}{FP + TN} \tag{4.6.4}$$

where TP (true positive) is the detection of an actual event, FP (false positive) is setting the alarm on if there is no contaminant in system, FN (false negative) is the situation when actual event is not detected, TN (true negative) is keeping the alarm off while there is only clear water in the system. During the study 195 samples were analyzed manually, and 722 were measured on-line during simulation experiments with three contamination scenarios. Most of the monitored parameters showed changes during contamination events, and the extent of changes depended on the type of contaminant. As expected, the most dramatic changes were observed during wastewater scenario experiment. A representative example of a response to contamination is demonstrated in Fig. 4.6.17. EC, TOC, ORP, turbidity, FCM-TCC and ATP measurements of grab samples showed clear peaks during water contamination and indicated a biological contamination. Strong correlations were obtained between these parameters (not shown). However, temperature and pH did not show any specific fluctuations in the presence of a contaminant. Interestingly, ORP changes were obvious only at the station A (15 min water retention time), and no changes were observed at station B. Further study is needed to explain the relation between changes of ORP and water retention time, and whether this parameter is critical for DW monitoring.

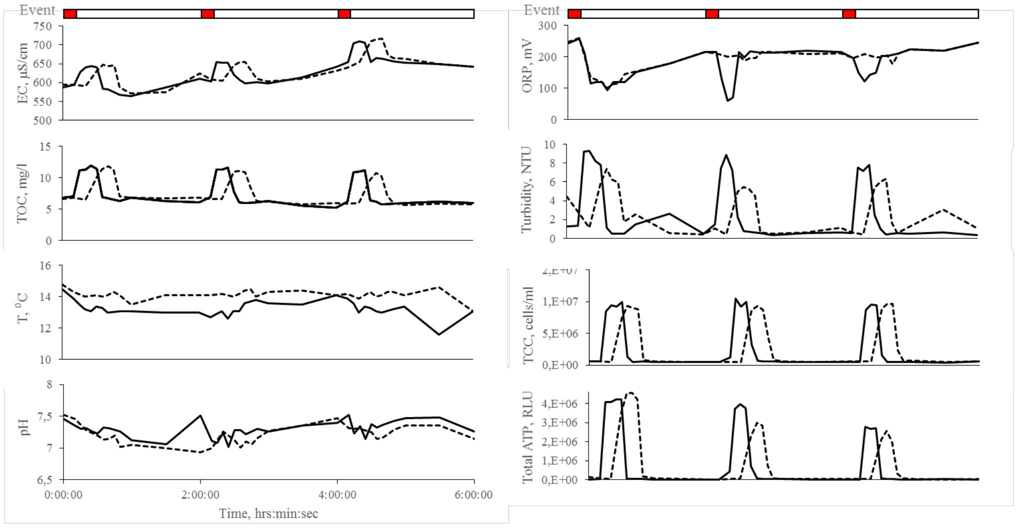

Figure 4.6.17: Raw data from wastewater scenario with grab sampling monitoring, solid line station A (retention time 15 min), dashed line station B (30 min), red bars contamination event at contamination point.

The event detection algorithm with Mahalanobis distance method was evaluated by determination of TPR and FPR values. TPR and FPR values were determined for overall system performance, considering all measured parameters (Fig. 4.6.18). The contamination detection was more reliable with grab sampling, resulting in TPR 0.89 (meaning that 89 % of events should be detected), than the online monitoring, which detected only 56% of contamination cases. The false alarm rate for both methods was similar: 5 % and 6 % for grab sampling and online monitoring, respectively.

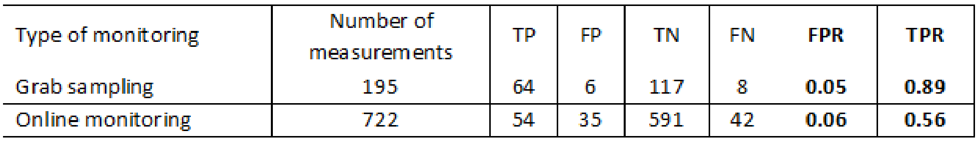

Type of monitoring	Number of measurements	TP	FP	TN	FN	**FPR**	**TPR**
Grab sampling	195	64	6	117	8	**0.05**	**0.89**
Online monitoring	722	54	35	591	42	**0.06**	**0.56**

Figure 4.6.18: Results of evaluation of contamination detection performance.

The results of experiments allowed concluding that the provided drinking water contamination event detection system and algorithm have promising results and future studies and verification of the system can be done. In addition the fingerprints of each contaminant have been determinate and represented as clean (uncontaminated) and contaminated water ratio (wastewater and water with prolonged retention time), are shown as a multidimensional spider graphs on Fig. 4.6.19.

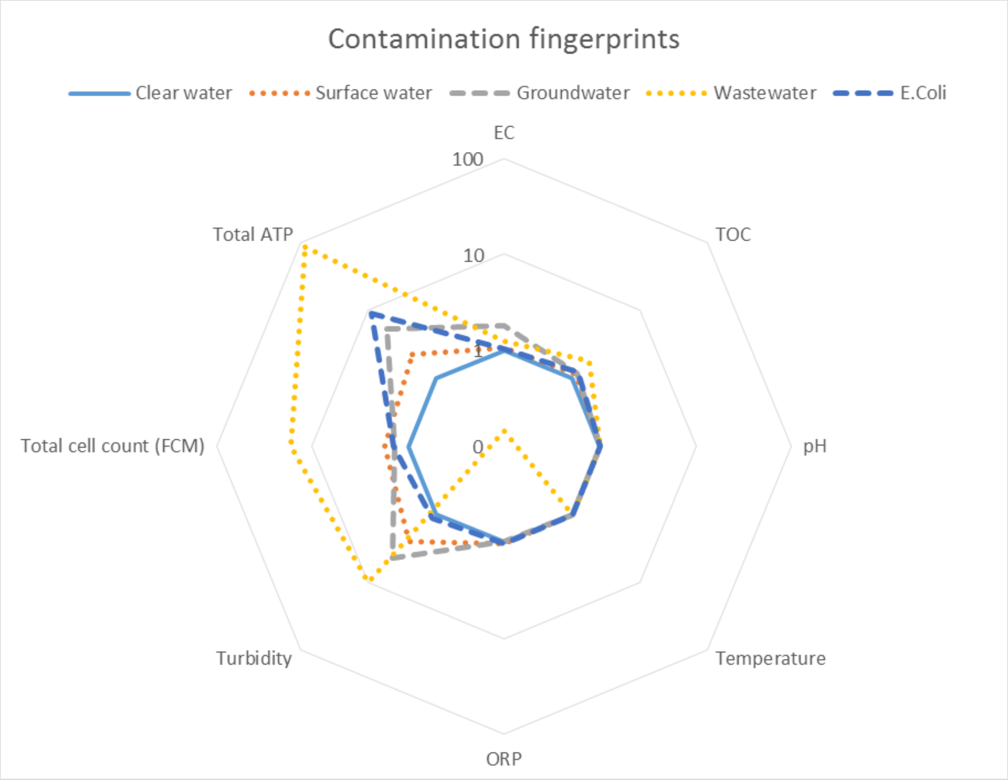

Figure 4.6.19: Example of sensor system response to contamination events - fingerprints.

4.6.10 Verification of event detection and alarm triggering algorithm by the measurements in pilot scale drinking water supply system

After the development and improvement of contamination detection system and algorithm the verification experiments were carried out. To conduct the verification, four independent contamination scenarios events with 3 repetitions were done (wastewater, groundwater, untreated water, terrorist attack). In total 12 experiments. To simulate the contamination events for system verification, the contamination event (10% contaminant of total flow) time was extended to 3 hours and the total time of each experiment to 8 hours. Drinking water quality readings were done every minute. And the hydraulic parameters were maintained as in previously described experiments. Contaminant detection probability was analyzed for different combination of physico-chemical and biological parameter combinations physico-chemical, physico-chemical + ATP, physico-chemical + FCM, physico-chemical + ATP + FCM. The results of system verification showed that the system is capable to detect various contamination events with high probability (Fig. 4.6.20). The results for groundwater and wastewater scenarios showed 100% probability to detect the contamination, for surface water the probability was 96-97%. However the scenario with deliberate contamination (E.coli) spotlighted that contamination cannot be detected by physico-chemical sensors.

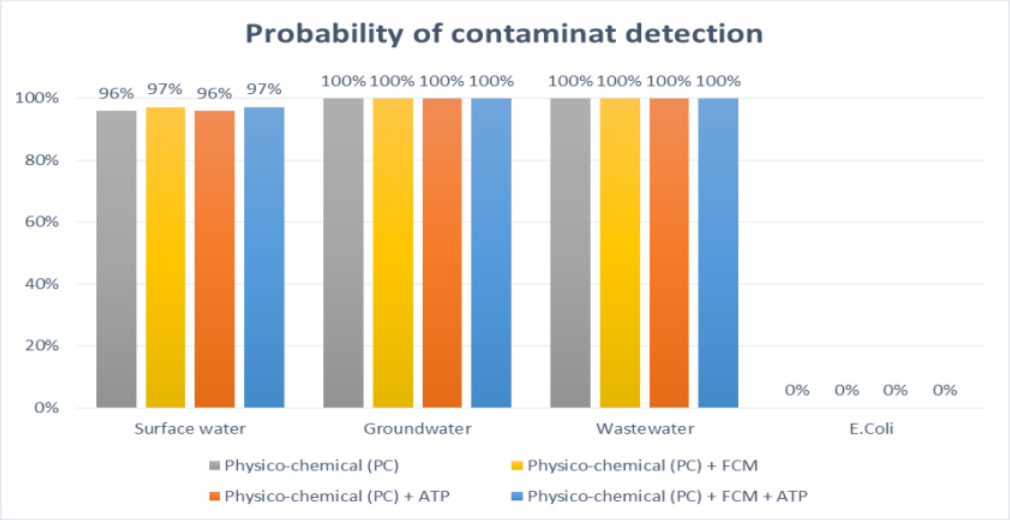

Figure 4.6.20: Probability of contamination event detection for various scenarios and sensor combination.

The *E.coli* contaminant can be detected by ATP measurements with 93% probability (Fig. 4.6.21). It means that at this point of automatization of measurement the deliberate contamination event is not detectable by on-line system. The ATP measurements should be applied to detect it.

The results from system verification experiments will be summarized and published in scientific publication.

4.6.11 Implementation of event detection and alarm triggering algorithm in on-line drinking water quality monitoring system

The previously developed alarm triggering algorithm and selected set of sensors where included in the on-line drinking water quality monitoring system.

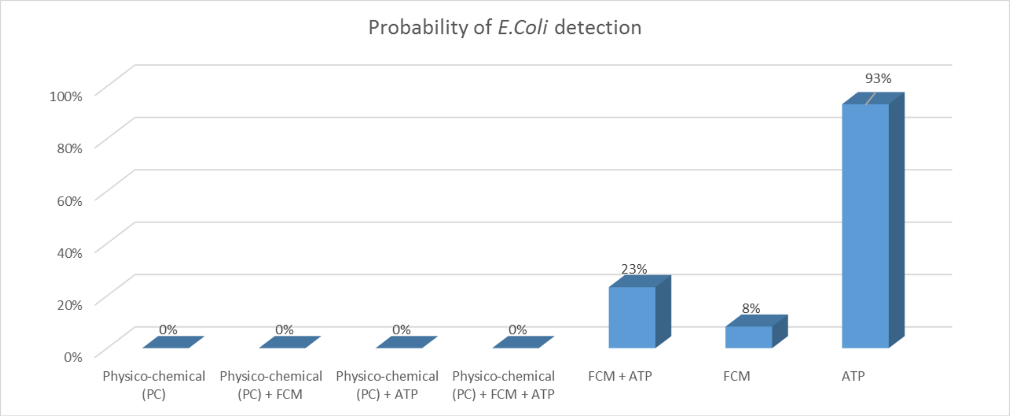

Figure 4.6.21: Probability of *E.coli* contamination event detection with different combinations of sensors.

The system consists of two parts the monitoring section at the site, and the data processing machines at the data center. Data from the site to data center is transferred via internet, powerlines (BPL technologies) or telemetry (Fig. 4.6.22). The full description of system is described in the technological description Drinking Water Quality Monitoring and Contamination Detection System (Appendix 4.9). The part of the system that have to be installed on the site is developed as a portable set of device and is easy transportable and equipped with internal power source to ensure the stability of the monitoring and contamination detection during the power shortages in city.

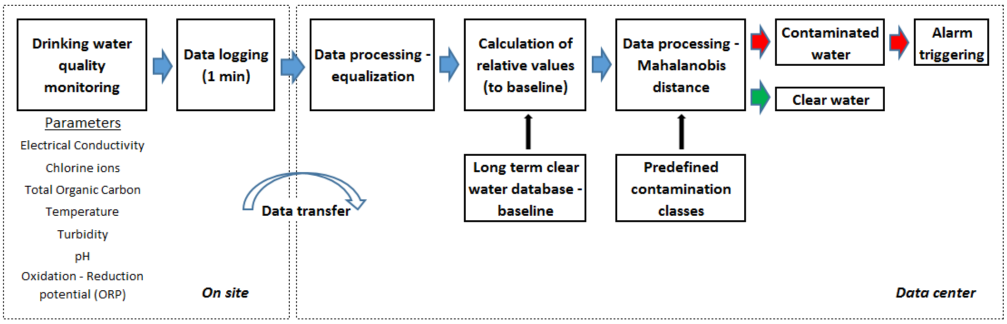

Figure 4.6.22: The drinking water quality monitoring system principle scheme.

The demonstration of the developed system was carried out RTU 57th International Scientific Conference, Section of Smart Biotechnology, Riga, Latvia, and caused the interest from various water utilities in Latvia.

4.6.12 Approbation of drinking water bacteriological quality monitoring system in real scale network

To evaluate the capabilities of designed technological solution in real drinking water supply system two activities where done approbation of on-line system in real drinking water supply system and determination of potential risk reduction to consumers by application of on-line system. The approbation of bacteriological quality monitoring system was accomplished in Liepaja city water supply system (Fig. 4.6.23). It was selected because of two water sources with different drinking water quality parameters, so it was possible to simulate the contamination events by supplying the water from different water sources and attempting to distinguish the water source at the monitoring point. The results showed a good response to different water source drinking water and identification between them.

Figure 4.6.23: The drinking water quality monitoring system during approbation experiments.

The letter of reference from Liepajas udens ltd. was received where a positive appreciation was explicated (Appendix 4.10). Although there were some shortages of the system identified the waterproofness should be improved, installed sensors are not pressure resistant (¡1 bar), graphical user interface should be improved. Also some additional actions by water utilities before installation of such a system should be implemented as development of detailed and precise hydraulic model, development of action plan during contamination events and training of personal for maintenance of system, interpretation of data, and reaction in emergency situations. To predict the possible advantages by implementation of on-line drinking water quality monitoring and contamination event detection system, the consumer influence areas were simulated. The study was conducted for Riga city water supply system. The simulations of contaminant expansion in system were simulated with Epanet 2.0 software for hydraulic modelling. The spreading time of contaminant was assumed as 24 hours with conventional drinking water quality monitoring by usage of 1 sampling per day and Heterotrophic plate count method for detection of bacterial contamination and 2 hours with on-line system, by taking to account the reaction time of water utilities. Scenarios by contamination intrusion in main pipes and distribution pipes where simulated in various sites. The example of simulation results is showed in Fig. 4.6.24.

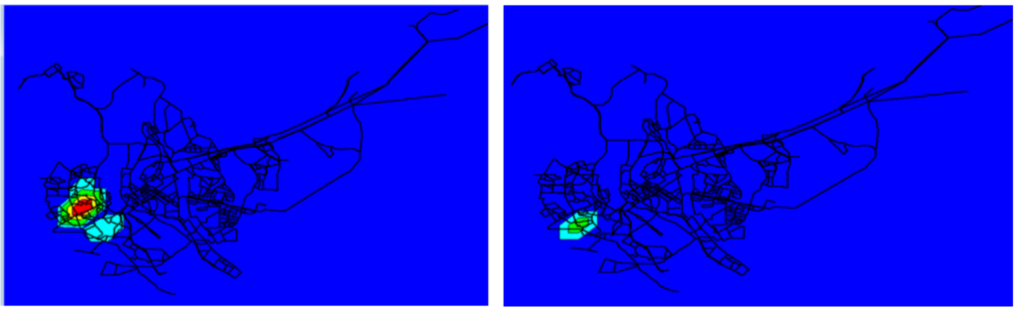

Figure 4.6.24: The drinking water quality monitoring system during approbation experiments.

The results showed that the area or consumers affected by the contamination event can be reduced by 2-50%, based on location of intrusion point, when on-line system is implemented. The full results of study is summarized in Master Thesis On-line water quality monitoring system integration in water distribution network (Appendix 4.11) which was defended on 2017, Riga Technical University, Department of Heat, Gas and Water technologies.

4.6.13 Conclusions and future work

On-line drinking water monitoring system was designed and validated during this project. Physically-chemical sensors with or without novel biological methods were tested for short-term, long-term monitoring and contamination event detection in the pilot-scale distribution system and in the real-scale water distribution system. Long-term experiments provided wide data range on drinking water quality parameters that have not been analyzed before in such an extent. Obtained results demonstrated high-resolution temporal variabilities. However, the large amount of data met technical issues in terms of data interpretation and analysis, which should be addressed in future studies. Ideally, improvements in long term monitoring should be achieved by limiting the data storage and analysis amount, which would allow to adapt them for implementation in hydraulic and drinking water quality models. Moreover, those systems can be implemented as a tool in drinking water safety plan. Application of system can reduce the contaminated area of DWDS by 2-50%, it means that the potential threat to costumers during contamination events can be reduces significantly. Successful approbation of the on-line monitoring system during simulation experiments demonstrated high sensitivity of the tool, which was corroborated with biological methods. Methods and algorithms, implemented for drinking water contamination event detection and identification, were tested and moved a step forward in development of early warning system. Also more tests should be done to recognize the shortages of such systems, for example, a low concentration pollution of system and positive/negative alarm triggering events to evaluate the overall sensitivity of system. Developed monitoring system, combined with Mahalanobis distance method event detection algorithm, represents early warning system (EWS) technology, which was also developed and adapted during the project. Mahalanobis distance method resulted in 89-100% of positive detection alarms and 5-30% of false positive alarms for biological contamination events, which indicates a good potential for the applied measurement tools and measured parameters to be implemented in EWS. Manual measurements showed better results than the on-line sensors. This highlights an importance of using high-precision sensors for continuous measurements and thorough maintenance and frequent calibration. Although more than a large part of contamination events was detected, sustainability of the measurement system and/or the detection algorithm should be improved. TOC, turbidity, EC, ATP and FCM-TCC showed the best response to all types of contamination. The main conclusions of the study are that physically-chemical sensors are effective enough for situations, when bacterial contamination risk exists due to a potential intrusion of the water with different parameters, which can happen due to system failure or pipe leakage, but the risk of intentional bacterial contamination is minimal. However, if the risk of bioterrorist attack is significant, novel biological methods should be applied. The EWS with physically-chemical sensors could be applied in DWDSs, as a relatively cheap option for rapid contamination detection. However, the risks of low concentration contamination not being detected exist. The combination with biological methods is the most accurate approach. To our knowledge, a fully automated microorganism detection system is approved only for FCM, and the costs for such system are high. However, it has a potential to be combined with physically-chemical sensors and event detection algorithms to serve as EWS. ATP methods automation should be developed, as this is a very sensitive method for biological contamination detection. The overall conclusion is that EWS will become a common drinking water monitoring tool. The topicality of issues addressed in this phase is very high in society and it is proved by publication in media (5 publications radio, TV, web).

Chapter 4.7

Summary of project results

Project results presented in order of performance indicators listed in the project proposal.

4.7.1 Scientific performance indicators

4.7.1.1 Original scientific articles (SNIP≥ 1)

1. Alina Nescerecka, Talis Juhna, Frederik Hammes, Behavior and stability of adenosine triphosphate (ATP) during chlorine disinfection, Water Research, Volume 101, 15 September 2016, Pages 490-497, ISSN 0043-1354, `http://dx.doi.org/10.1016/j.watres.2016.05.087`.
2. A.Lorencs, I.Mednieks, J.Sinica-Sinavskis. Selection of Informative Hyperspectral Band Subsets Based on Entropy and Correlation (minor revisions in preparation for publication in "International Journal of Remote Sensing").
3. Nescerecka, A., Juhna, T., Hammes, F. Identifying the underlying causes of biological instability in a full-scale drinking water supply system, submitted to Water Research on 07.11.2017.
4. Supe, A., Spolītis, S., Poriņš, J. Bobrovs Investigation of optical fiber nonlinearity coefficient measurements with two tunable wavelength light sources. Optical materials. In press.

4.7.1.2 Original scientific articles (SCOPUS/Web of Science/IEEExplore)

1. K. Kruminsh, V. Peterson, V. Plotsinsh. The influence of thermal hysteresis of a clocked comparator on the operation of the comparator type sampling converter, Automatic Control and Computer Sciences, July 2015, Volume 49, Issue 4, pp. 245-253. `http://link.springer.com/article/10.3103%2FS0146411615040070`

2. E. Hermanis, M. Greitans, V. Aristov. Identification of characteristics of two-terminal networks from the pulse response of the current Automatic Control and Computer Sciences, July 2015, Volume 49, Issue 4, pp 239-244. http://link.springer.com/article/10.3103/S0146411615040057

3. Aristov, V.; Shavelis, R.; Shupols, G.; Cirulis, R., An investigation of non-traditional approach to narrowing the GPR pulses, in Radioelektronika (RADIOELEKTRONIKA), 2015 25th International Conference , vol., no., pp.373-375, 21-22 April 2015 doi: 10.1109/RADIOELEK.2015.7129043 (MAREW 2015).

4. K. Ozols Implementation of reception and real-time decoding of ASDM encoded and wirelessly transmitted signals. Microwave and Radio Electronics Week 2015 (MAREW2015), Pardubice, Czech Republic, April 21-23, 2015. DOI: 10.1109/RADIOELEK.2015.7129020 `http://ieeexplore.ieee.org/xpl/articleDetails.jsp?arnumber=7129020`

5. Sandis Spolitis, Lilita Gegere, Anita Alsevska, Ilja Trifonovs, Jurgis Porins, and Vjaceslavs Bobrovs Optical WDM-PON Access System with Shared Light Source Progress In Electromagnetics Research Symposium, PIERS 2015 in Prague, Czech Republic, 06-09 July, 2015.pp.15.

6. K.Sudars, I.Bilinskis, E.Buls, Discrete Fourier Transform of the signals recovered by using high-performance Event Timers, Baltic Electronics Conference 2016, Tallinn, Estonia (IEEE Xplore, SCOPUS).

7. A. Lorencs A, Mednieks I, Siņica-Siņavskis J. 2016 Selection of Informative Bands for Classification of Hyperspectral Images Based on Entropy, Proc. of BEC2016, the 15th Biennial Conference on Electronics and Embedded Systems. Tallinn, Estonia on October 3-5, 2016. pp. 135-138 (IEEE Xplore, SCOPUS).

8. Aristov, V. (2016) Optimization of the transmitter pulse duration by the criterion of the radiation spectrum maximization at a given frequency. Automatic Control and Computer Sciences. 50(4), 220-225. (SCOPUS) Springer Link.

9. Sergejs Olonkins, Vjaceslavs Bobrovs, Girts Ivanovs FOPA Pump Phase Modulation and Polarization Impact on Generation of Idler Components, Elektronika ir Electrotechnika, Vol.77, No.4, 2016, pp. 77-81, ISSN 1392-1215 (to be included in SCOPUS).

10. Lavrinoviča, I., Poriņš, J., Brūklītis, E., Supe, A. Evaluation of Effective Area and Nonlinearity Coefficient of Erbium-Ytterbium Doped Optical Fibers. In: Progress in Electromagnetics Research Symposium (PIERS 2016): Proceedings, China, Shanghai, 8-11 August, 2016. Shanghai: The Electromagnetics Academy, 2016, pp.1-5. ISBN 78-1-934142-30-1. ISSN 1559-9450. e-ISSN 1559-8985 (to be included in SCOPUS).

11. Nescerecka, A., Hammes, F., Juhna, T., 2016. A pipeline for developing and testing staining protocols for flow cytometry, demonstrated with SYBR Green I and propidium iodide viability staining. Journal of Microbiological Methods 131, 172180. doi:10.1016/j.mimet.2016.10.022.

12. K.Sudars, Face Recognition Face2vec Based on Deep Learning: Small Database Case, Automatic Control and Computer Science (accepted). (to be included in SCOPUS).

13. Roberts Kadiķis Recurrent Neural Network Based Virtual Detection Line. 2017 The 10th International Conference on Machine Vision (ICMV 2017), November 13-15, 2017, Vienna, Austria. `http://www.icmv.org/` (to appear in SCOPUS)

14. I.Bilinskis, E.Boole, K.Sudars Combination of periodic and alias-free non-uniform signal sampling for wideband signal digitizing and compressed transmitting based on picosecond-resolution event timing, 2017 Signal Processing Symposium. (SPSympo 2017) September 12-14, 2017. Debe, Poland. (to appear in SCOPUS) `https://signalprocessingsociety.org/blog/spsympo-2017-2017-signal-processing-symposium`

15. Dejus, S., Nescerecka A., Kurcalts, G., Junha, T. Detection of Drinking Water Contamination Event with Mahalanobis Distance Method, Using On-line Monitoring Sensors and Manual Measurements Data, Proceedings of the 9th IWA Eastern European Water Professionals Conference, Budapest, Hungary, 2017, p.226-233 (SCOPUS)

16. Dejus, S., Nescerecka, A., Juhna, T., On-line Drinking Water Contamination Event Detection Methods, Proceedings of the 11th International Scientific and Practical Conference ENVIRONMENT. TECHNOLOGY. RESOURCES, Volume I, Rezekne, Latvia, 2017, p.77-81, ISSN 1691-5402 (SCOPUS) `http://journals.ru.lv/index.php/ETR/article/view/2627/2497`

17. J.Putrina, S.Olonkins, V.Bobrovs Investigation of amplification span length impact on the quality of the signal in WDM transmission systems with erbium-doped fiber amplifiers, The 38th PIERS in St Petersburg, Russia 22 25 May, 2017, PIERS2017 Proceedings (tiks publicēts SCOPUS un IEEEXplore datubāzēs); `http://piers.org/piers2017StPetersburg/`

18. S.Olonkins, I.Stankunovs, D.Pilats, V.Bobrovs Suppression of CC-FWM Inter-channel Crosstalk Using Unequal Channel Spacing in an 8-channel WDM Transmission System with Parametric Amplification , The 38th PIERS in St Petersburg, Russia 22 25 May, 2017, PIERS2017 Proceedings (to appear in SCOPUS and IEEEXplore). `http://piers.org/piers2017St.Petersburg/`

19. Ozols, K., Shavelis R., Amplitude Adaptive ASDM without Envelope Encoding, The 2016 European Signal Processing Conference (EUSIPCO 2016), Budapest, Hungary, August 29 -September 2, 2016.

DOI: 10.1109/EUSIPCO.2016.7760231 `http://ieeexplore.ieee.org/document/7760231/`

20. Shakya, S., Supe, A., Lavrinoviča, I., Spolītis, S., Poriņš, J. Different Optical Fiber Nonlinear Coefficient Experimental Measurements. No: Proceedings of 6th International Workshop on Fiber Optics in Access Networks (FOAN 2016), 2016, 1.-4.lpp.

21. Shavelis R., Ozols K., Greitans M., Amplitude Adaptive ASDM circuit, 2017 3rd International Conference on Event-Based Control, Communication and Signal Processing, Madeira, Portugal, May 24-26, 2017, DOI: 10.1109/EBCCSP.2017.8022815. `http://ieeexplore.ieee.org/document/8022815/`

22. V.Aristov Distance localization of the moving object by applying the KarhunenLoeve transform to ultra-wideband impulse signals Automatic Control and Computer Sciences September 2017, Volume 51, Issue 5, pp 294300. DOI https://doi.org/10.3103/S0146411617050029 `https://link.springer.com/article/10.3103/S0146411617050029`.

23. K. Sudars, Face Recognition Face2vec Based on Deep Learning: Small Database Case, Automatic Control and Computer Sciences, 2017 (2) R. January 2017, Volume 51, Issue 1, pp 5054.

24. R.Kadikis, Recurrent neural network based virtual detection line, the 10th International Conference on Machine Vision ICMV 2017 , November 13-15, 2017 — Vienna, Austria. Accepted publication.

25. Dejus, S., Nescerecka, A., Kurcalts, G., Juhna, T.: Detection of Drinking Water Contamination Event with Mahalanobis Distance Method, Using On-line Monitoring Sensors and Manual Measurements Data, Revision of article after revision submitted to Water Science and Technology: Water Supply on 21.12.2017.

26. Ingrīda Lavrinoviča and Jurğis Poriņš An Improvement of EDFA efficiency by using Ytterbium co-doped optical fibers, IEEE BlackSeaCom2016 (IEEExplore).

27. Vladislavs Bičkovs and Vjačeslavs Bobrovs Performance Evaluation of a 40 Gbps WDM Transmission System with a Single-pump Raman Amplifier, PIERS 2016 (SCOPUS and IEEExplore).

28. Jūlija Putrina and Vjačeslavs Bobrovs Evaluation of Erbium Doped Fiber Amplifier Application in Fiber Optics Transmission Systems, PIERS 2016 (SCOPUS and IEEExplore).

29. Pavlovs D., Bobrovs V Relationship between Spectral Efficiency and Energy Efficiency in 10 Gbps NRZ-OOK, 40 Gbps NRZ-DPSK and 100 Gbps DP-QPSK WDM Transmission System), In: Progress in Electromagnetics Research Symposium (PIERS 2016) (SCOPUS and IEEExplore)

30. Olonkins, S. Stankunovs, I, Pilats, D. Bobrovs V., Suppression of CC-FWM Inter-channel Crosstalk Using Unequal Channel Spacing in an 8-channel WDM Transmission System with Parametric Amplification PIERS2017 Proceedings (SCOPUS and IEEEXplore).

31. Grunvalds R., Ciekurs A., Porins, J., Supe A., "Evaluation of optical fiber lifetime in optical ground wire", Latvian Journal of Physics and Technical Sciences, Vol 54, pp. 40-49, 2017.

4.7.1.3 Reviewed scientific monographs

1. Bobrovs, V., Olonkins S., Spolītis S., Poriņš, J., Ivanovs, Ģ Evaluation of Parametric and Hybrid Amplifier Applications in WDM Transmission Systems, 2017. pp. 181-210, ISBN 978-953-51-1730-8. book edited by Rastislav Roka, ISBN 978-953-51-3276-9, Print ISBN 978-953-51-3275-2.

4.7.1.4 Other scientific articles

1. Dejus S., Nescerecka A., Nazarovs S., Juhna T., Review on Existing and Emerging Biological Contamination Detection Tools for Drinking Water Distribution Systems (DWDS) Online Monitoring, Proceedings of the 7th IWA Eastern European Water Professionals Conference for young and senior water professionals, Belgrade, 2015, p.320-332.

2. Dejus, S., Rusenieks, R., Nescerecka, A., Nazarovs, S., Juhna, T., Long Term Drinking Water Quality Monitoring in Drinking Water Supply Systems by On-Line Sensors, Book of Abstracts, 8th Eastern European Young Water Profesionals Conference, Gdansk, Poland, 2016, p.73-74, ISBN 978-83-7493-936-2.

3. Aristov V. Karhunen-Loeve Transform As a Tool to Eliminate Signals Redundancy, When Small Targets Detection. Sciences of Europe. Vol.2, No.2, pp. 53-57, 2016. Praha, Czech Republic (in Russian).

4. Dejus, S., Nescerecka, A., Kurcalts, G., Juhna, T., "Drinking Water Contamination Detection by On-line Monitoring: Pilot Scale Studies", Book of Abstracts, 9th IWA Eastern European Young Water Professionals Conference, Budapest, Hungary, 2017, p.161-162, ISBN 978-963-313-256-2

5. Udalcovs A., Bobrovs V., "Energy Efficiency in WDM Fiber-Optical Links Considering OADM/OXC Nodes Optics Communications" Vol.359 pp. 102. - 108. 2016

4.7.1.5 Doctoral thesis

1. Sandis Spolitis Development and evaluation of high-speed optical access systems, RTU (Supervisor Dr.sc.ing., Prof. Ģirts Ivanovs).(2015.g.)

2. Kaspars Ozols Asynchronous data acquisition of electroencephalogram signals/ Elektroencefalogrammas signālu asinhrona datu ieguve. Supervisor Dr.sc.comp., senior researcher M.Greitāns. (Defended RTU Promotion Council P-08 16.06.2017);

3. Alīna Neščerecka Biological stability in chlorinated drinking water distribution networks /Bioloģiskā stabilitāte hlorētos dzeramā ūdens sadales tīklos Supervisors Professor Dr. sc.ing. Tālis Juhna, Dr.Frederik Hammes. (Defended RTU Promotion Council P-12 16.06.2017)

4. Andris Skrastiņš Resursu un atļauju vadība nākošās paaudzes tīklos/ Resource and Admission Management in Next Generation Networks, diploma no. D 0637. (Supervisor Prof. Dr. sc. ing.G. Lauks).

5. Roberts Kadiķis "Efektīvas video apstrādes metodes kustīgu objektu atklāšanai/ Effective video processing methods for detection of moving objects"- Dissertation approved by the Institute of Electronics and Computer Science for submission (pre-defended 29.06.2017).

6. Gatis Šūpols "Taktējama komparatora veida ultraplatjoslas impulsu radara sensors/ Pulse radar sensor of clockable comparator type" - Dissertation approved by the Institute of Electronics and Computer Science for submission (pre-defended 29.06.2017).

7. Juris Siņica-Siņavskis "Multidimensionālu attēlu joslu skaita ekvivalentas redukcijas pieejas objektu klasifikācijai/ Equivalent reduction approaches of multidimensional image spectral bands for object classification"- Dissertation approved by the Institute of Electronics and Computer Science for submission (pre-defended 27.11.2017).

4.7.1.6 Master thesis

1. Matīss Viekalis Compensation methods of dispersion and research in WDM PON system, (Supervisor Prof. Dr.sc.ing. Ģirts Ivanovs);

2. Viktors Romans Research and Evaluation of Chromatic Dispersion Compensation Schemes for Long-Haul Fiber Links, (Supervisor Prof. Dr.sc.ing. Jurğis Poriņš);

3. Ilona Ābola Evaluation of Chromatic Dispersion Compensation Methods in WDM-PON Systems, (Supervisor Prof. Dr.sc.ing. Ģirts Ivanovs);

4. Alvis Meņğo All-Optical Wavelength Conversion in Wavelength Division Multiplexing Systems (Supervisor Prof. Dr.sc.ing. Ģirts Ivanovs);

5. Zane Upeslace Evaluation of DB and DSPK Modulation Formats in WDM Transmission Systems, Ms.sc.ing;

6. Agris Sīlis Optical Signal Regeneration in Completely Optical Way, (Supervisor Prof. Dr.sc.ing. Jurğis Poriņš);

7. Mārtiņš Puķītis Multidimensional distributions application aspects in analysis of multispectral images (Supervisors Prof. Aivars Lorencs Defended LU FMF 08.06.2015).
8. Valts Dilendorfs Effectiveness Evaluation of Dispersion Compensation Methods in FOTS (Supervisor Dr.sc.ing. Vjačeslavs Bobrovs), defended 2016.
9. Jūlija Putrina EDFA Characteristics and Working Principle Evaluation in FOTS (Supervisor Prof. Dr.sc.ing. Vjačeslavs Bobrovs), defended 2016.
10. Reinis Grūnvalds Dispersion analysis in OPGW transmission lines (Supervisor Prof. Dr.sc.ing. Jurğis Poriņš) defended 2016.
11. Vladislavs Bičkovs Research of RAMAN Amplification in Fiber-optic Communication Systems (Supervisor Prof. Dr.sc.ing. Vjačeslavs Bobrovs), defended 2016.
12. Vjačeslavs Stankevičs Dzeramā ūdens kvalitātes tiešsaistes monitoringa sistēmu ieviešana ūdens apgādes tīklos/ On-line water quality monitoring system integration in water distribution network (Supervisor S.Dejus) defended 2017.
13. Toms Salgals Nākamās paaudzes spektrāli efektīvu optisko sakaru sistēmu izpēte un novērtējums/Evaluation and Investigation of Next-generation Spectrally Efficient Optical Communication Systems, diploma Nr. MDE3103; (Supervisor S.Spolītis). RTU
14. Vadims Sereda Intensitātes un fāzes modulētu WDM-PON piekļuves sistēmu novērtējums/Evaluation of Intensity and Phase Modulated WDM-PON Access Systems, diploma Nr. MDE3105 (Supervisor S.Spolītis). RTU.
15. Dagne Cēsniece Četru viļņu mijiedarbes efekta pielietojuma izpēte WDM piekļuves sistēmās/Research and Application of Four Wave Mixing Effect in WDM Access Systems, diploma Nr. MDE3089 (Supervisor S.Spolītis). RTU
16. Monta Peciņa Intensitātes un fāzes modulētas WDM-PON pārraides sistēmas izstrāde un novērtējums/ Development and Evaluation of Intensity and Phase Modulated WDM-PON Transmission System, diploma Nr. MDE3100 (Supervisor S.Spolītis). RTU
17. Ģ.Kurcalts "Dzeramā ūdens piesārņojuma konstatēšana tiešsaistes režīmā / Online pollution detection in drinking water" (Supervisor S.Dejus), prepared withim GudPils project, to be defended in 2018, RTU.

4.7.1.7 Bachelor thesis

1. Abajs, M. (2015). Ultra-Wideband Pulse Radar Sensor Application in Security Systems (Unpublished bachelor thesis). Riga Technical University. https://nda.rtu.lv/en/view/14134
2. Lielpinka, M. (2015). Remote Sensing Data Acquisition and Processing Using Unmanned Aircraft (Unpublished bachelor thesis). Riga Technical University. https://nda.rtu.lv/en/view/14023
3. Maurins, M. (2015). Non-dectructive Ice Thickness Monitoring (Unpublished bachelor thesis). Riga Technical University. https://nda.rtu.lv/en/view/14130.
4. Raitis Bērziņš (2016) Structure Inspection Using Wall and Ground Probing Radar. Scientific supervisor Mg.sc.ing.G.Supols.
5. Eduards Lobanovs (2016) Room Change and Object Movement Detection Sensor Solutions. Scientific supervisor Mg.sc.ing. G.Supols.
6. Romans Maļiks (2016) Achieving Quad-rotor Flight Stabilisation Using Proportional-integral-derivative (PID) Controller. Scientific supervisor G.Supols.
7. Atvars Trams (2016) The dimensionality reduction method for hyperspectral images. Scientific supervisor Mg.Math. J.Sinica-Sinavskis.
8. Iveta Albertiņa (2017) Sekošana objektiem daudzkameru vide/Object tracking from multiple video cameras Scientific supervisor Dr.sc.comp. K.Sudars.

4.7.1.8 Exploitation of results in study courses

Project results were used to enhance the following study courses:

1. Master studies course RDE 417 "Physics of the optical information processing" (RTU)
2. Master studies course RDE 419 "Fiber optics transmission systems" (RTU)
3. Bachelor studies course BŪK329 "Water supply" (RTU)

4.7.2 Performance indicators of the promotion of the project

4.7.2.1 Presentations in conferences

1. Aivars Lorencs, Ints Mednieks, Juris Sinica-Sinavskis Classification of Multisensor Images With Different Spatial Resolution. The 19th International Conference ELECTRONICS 2015, Palanga, Lithuania, 15-17 June, 2015.

2. S. Spolitis, L. Gegere, A. Alsevska, I. Trifonovs, J. Porins, and V. Bobrovs Optical WDM-PON Access System with Shared Light Source Progress In Electromagnetics Research Symposium, PIERS 2015 in Prague, Czech Republic, 06-09 July, 2015.

3. Dejus S., Nescerecka A., Nazarovs S., Juhna T., Review on Existing and Emerging Biological Contamination Detection Tools for Drinking Water Distribution Systems (DWDS) Online Monitoring, Proceedings of the 7th IWA Eastern European Water Professionals Conference for young and senior water professionals, Belgrade, 2015, p.320-332.

4. K. Ozols Implementation of reception and real-time decoding of ASDM encoded and wirelessly transmitted signals. Microwave and Radio Electronics Week 2015 (MAREW2015), Pardubice, Czech Republic, April 21-23, 2015.

5. Aivars Lorencs, Juris Siņica- Siņavskis Spectral channel selection using variance, LU 74th conference, Riga, February, 2016.

6. Dejus S., Nescerecka A., Nazarovs S., Juhna T., Review on Existing and Emerging Biological Contamination Detection Tools for Drinking Water Distribution Systems (DWDS) Online Monitoring, Proceedings of the 7th IWA Eastern European Water Professionals Conference for young and senior water professionals, Belgrade, 2015, p.320-332.

7. Nescerecka A., The application of adenosine-triphosphate (ATP) measurements for determination of bacterial viability in chlorinated drinking water, How Dead is Dead Conference IV, Eawag, Swiss Federal Institute of Aquatic Science and Technology, Duebendorf/Zurich, Switzerland, 2122 May 2015.

8. Aivars Lorencs, Ints Mednieks, Juris Sinica-Sinavskis Selection of Informative Bands for Classification of Hyperspectral Images Based on Entropy, BEC2016, the 15th Biennial Conference on Electronics and Embedded Systems. Tallinn, Estonia on October 3-5, 2016.

9. K. Sudars, I.Bilinskis, E.Buls, Discrete Fourier Transform of the signals recovered by using high-performance Event Timers, Baltic Electronics Conference 2016, Tallinn, Estonia.

10. Dejus, S., Rusenieks, R., Nescerecka, A., Nazarovs, S., Juhna, T., Long Term Drinking Water Quality Monitoring in Drinking Water Supply Systems by On-Line Sensors, IWA 8th Eastern European Young Water Profesionals Conference, Gdansk, Poland, 12-14 May 2016.

11. Nescerecka, A., Juhna, T., Hammes, F., A new approach for biological stability assessment in a full-scale drinking water supply system. IWA Specialist Conference Microbial Ecology and Water Engineering, 2016, Copenhagen, Denmark 4-7 September 2016.

12. Nescerecka, A., Juhna, T., Seasonal Drinking Quality Variations in Drinking Water Supply Network, RTU 57th International Scientific Conference, Section of Heat, Gas and Water Technologies, Riga, Latvia, 14-18 October, 2016.

13. Dejus, S., Long Term Drinking Water Quality On-line monitoring, RTU 57th International Scientific Conference, Section of Heat, Gas and Water Technologies, Riga, Latvia, 14-18 October, 2016.

14. Shakya, S., Supe, A., Lavrinoviča, I., Spolītis, S., Poriņš, J. Different Optical Fiber Nonlinear Coefficient Experimental Measurements. No: Proceedings of 6th International Workshop on Fiber Optics in Access Networks (FOAN 2016), Lisbon, 2016.

15. Lavrinovica I., Porins J., An Improvement of EDFA efficiency by using Ytterbium co-doped optical fibers, 4th IEEE International Black Sea Conference on Communications and Networking (BlackseaCom), Varna, Bulgaria 6-9 June 2016.

16. Putrina J. Bobrovs V., Evaluation of Erbium Doped Fiber Amplifier Application in Fiber Optics Transmission Systems, The 37th Progress in Electromagnetics Research Symposium: PIERS 2016, China, Shanghai, 8-11 August, 2016.

17. Olonkins S., Bobrovs V., Ivanovs G., FOPA Pump Phase Modulation and Polarization Impact on Generation of Idler Components, 20th International Conference ”Electronics 2016” Palanga, Lithuania 13th-15th June, 2016.

18. Pavlovs D., Bobrovs V Relationship between Spectral Efficiency and Energy Efficiency in 10 Gbps NRZ-OOK, 40 Gbps NRZ-DPSK and 100 Gbps DP-QPSK WDM Transmission System), The 37th Progress in Electromagnetics Research Symposium: PIERS 2016, China, Shanghai, 8-11 August, 2016.

19. Lavrinoviča, I., Poriņš, J., Brūklītis, E., Supe, A. Evaluation of Effective Area and Nonlinearity Coefficient of Erbium-Ytterbium Doped Optical Fibers. The 37th Progress in Electromagnetics Research Symposium: PIERS 2016, China, Shanghai, 8-11 August, 2016.

20. Dejus, S., Nescerecka, A., Kurcalts, G., Juhna, T., Drinking Water Contamination Detection by On-line Monitoring: Pilot Scale Studies, 9th IWA Eastern European Young Water Professionals Conference, Budapest, Hungary, 24-27 May, 2017 http://iwa-ywp.eu/

21. Dejus, S., Nescerecka, A., Juhna, T., On-line Drinking Water Contamination Event Detection Methods, ENVIRONMENT. TECHNOLOGY. RESOURCES ,11th International Scientific and Practical Conference. June 15-17, 2017, Rezekne Academy of Technologies, Rezekne, Latvia. http://conferences.ru.lv/index.php/ETR/index/announcement

22. Nescerecka, A., Water safety: Biological instability in drinking water distribution networks, International Baltic Water Works Conference 2017, Liepāja, Latvia, 19 May 2017.
23. Olonkins, S. Stankunovs, I, Pilats, D. Bobrovs V., Suppression of CC-FWM Inter-channel Crosstalk Using Unequal Channel Spacing in an 8-channel WDM Transmission System with Parametric Amplification The 39th Progress in Electromagnetics Research Symposium: PIERS 2017, Singapore 19 - 22 November 2017.

4.7.2.2 Posters in conferences

1. Nescerecka, A., Juhna, T., Hammes, F., 2015. Automated Flow Cytometry Approaches for Assessment of Chlorination Efficacy on Aquatic Bacterial Communities, How Dead is Dead IV conference, Eawag, Swiss Federal Institute of Aquatic Science and Technology, Duebendorf/Zurich, Switzerland, 2122 May 2015. Poster session.
2. Nescerecka, A., Juhna, T., Hammes, F., 2015. The Application of Adenosine- Triphosphate Measurements for Determination of Bacterial Viability in Chlorinated Drinking Water, How Dead is Dead IV conference, Eawag, Swiss Federal Institute of Aquatic Science and Technology, Duebendorf/Zurich, Switzerland, 2122 May 2015. Poster session.
3. Vladimir Aristov, Rolands Shavelis, Gatis Shupols and Rudolfs Cirulis. An Investigation of Non-traditional Approach to Narrowing the GPR Pulses. MAREW 2015. Microwave and Radio Electronics Week 2015. 25th International Conference Radioelektronika 2015. Pardubice, Czech Republic, April, 21-22, 2015. Poster session.
4. Dejus, S., Drinking Water Quality Monitoring and Safety of Drinking Water Supply Network, RTU 57th International Scientific Conference, Section of Smart Biotechnology, Riga, Latvia, 14-18 October, 2016 (Demonstration).
5. I.Bilinskis, E.Boole, K.Sudars Combination of periodic and alias-free non-uniform signal sampling for wideband signal digitizing and compressed transmitting based on picosecond-resolution event timing, 2017 Signal Processing Symposium. (SPSympo 2017) September 12-14, 2017. Debe, Poland. Poster session. `https://signalprocessingsociety.org/blog/spsympo-2017-2017-signal-processing-symposium`.

4.7.2.3 Organized public seminars

1. 2015-04-29 First stage seminar for Project no. 4 at EDI.
2. 2015-10-07 First stage joint SOPHIS seminar, with participation from all 4 projects (contribution of Project No.4- 0.25).

3. 2015-12-08 Public seminar of the Project no.4 at EDI.
4. 2016-03-16 Second stage seminar of the Project no.4 at EDI.
5. 2016-03-30 Second stage joint SOPHIS seminar, with participation from all 4 projects (contribution of Project No.4- 0.25).
6. 2016-11-30 Third stage seminar for Project no. 4 at EDI.
7. 2016-12-07 Third stage joint SOPHIS seminar, with participation from all 4 projects (contribution of Project No.4- 0.25).
8. 2017-09-29 Fourth stage seminar for Project no. 4 at EDI.
9. 2017-11-30 Final seminar for Project no. 4 discussing overall results at EDI.
10. 2017-12-05 Final joint SOPHIS seminar and demonstrations, with participation from all 4 projects (contribution of Project No.4- 0.25).

4.7.2.4 Participation in exhibitions

1. MINOX 2016 (7.-8.10.2016). Vladimirs Aristovs, Rūdolfs Cīrulis, Valdemārs Plociņš participated in Exhibition MINOX 2016 organized by Riga Technical University. Poster ”Remote Life-sign Detection: movement, breathing, heartbeat”. See http://www.connectlatvia.lv/minox2016/

4.7.2.5 Popular-science publications

Articles in Latvian:

1. Smags darbs un veiksme” (”Jaunais inženieris”): http://alephfiles.rtu.lv/TUA01/000057245_e.pdf
2. ”NO SISTĒMAS PILNVEIDOŠANAS LĪDZ TIRGUS IEKAROŠANAI” (”Tuvāk zinātnei”) : http://rtusp.lv/wp-content/uploads/2017/02/zurnals_06feb2017.pdf

Radio interviews:

1. http://www.radioswh.lv/2017/04/nacionala-zinatne-dr-sc-ing-jurgis-porins/
2. http://lr1.lsm.lv/lv/raksts/zinamais-nezinamaja/jauna-sistema-udens-un-siltuma-zudumu-noteiksanai.a68593/
3. http://ltv.lsm.lv/lv/raksts/29.09.2016-v-studii-issledovatel-laboratorii-vodi-rt
   id80921/
4. http://www.delfi.lv/rutks/vesels-ka-rutks/
   latviesu-zinatniece-pierada-ka-hloresana-reizem-veicina-mikroorganismu-vairosanc
   d?id=47903789
5. http://www.lsm.lv/lv/raksts/tehnologjijas/dzive/rtu-hloresana-ne-vienmer-nodrosina-dzerama-udens-attirisanu.a200642/

4.7.2.6 Long-term technological prognosis

1. Smart cities technologies: a long-term prognosis for R&D directions developed in the project (`http://www.edi.lv/media/uploads/UserFiles/Smart_cities_technologies.pdf`)

4.7.3 Economic performance indicators

4.7.3.1 Income from new projects

The following projects are started based on results and experience acquired in the framework of the programme:

1. ”Dynamic land use monitoring by fusion of satellite data” ESA PECS No.4000118771/16/NL/SC project, 2016-2018, Project manager: I.Mednieks, EDI part: 109430 EUR.
2. ”All-optical Signal Regeneration Using Nonlinear Optical Effects” ERDF 1.1.1.2/VIAA/1/16/151 01.12.2017 30.11.2020. Project manager Andis Supe, Supervisor Prof. Jurgis Porins. Sum 133806.00 EUR.
3. ”Next-Generation High-Speed Fiber Optical Access Systems (NG-FAST)” ERDF 1.1.1.2/VIAA/1/16/044 Project manager Sandis Spolitis, Supervisor Prof. Vjačeslavs Bobrovs. 133806.00 EUR.
4. ”Passive Fiber Optical Sensors for Energy Efficient Monitoring of the Technical Condition of a Transport Infrastructure” ERDF 1.1.1.1/16/A/072 Project leader Sandis Spolitis 01.03.2017.29.02.2020 600000 EUR.

4.7.3.2 Patents

1. LR patent No.15068. ”Stroboscopic converter for detection of ultra-wideband radar signāls. Inventors: Kārlis Krūmiņš, Vilnis Pētersons, Valdemārs Plociņš, Aivars Ševerdaks. Published: 20.11.2015. Applicant: Institute of Electronics and Computer Science.
2. LR patent No. 15224. Sistēma un metode telekomunikāciju optiskās šķiedras nelinearitātes koeficienta mērījumiem/ System and method for telecommunications optical fiber nonlinearity coefficient measurements, Names of inventors Andis Supe, Jurğis Poriņš, Vjačeslavs Bobrovs. Published 20.04.2017. Applicant: Riga Technical University.
3. LR patent No. 15236. Dispersijas kompensēta spektrāli sagriezta viļņgarumdales blīvēta optiskā sakaru sistēma/ Dispersion compensated spectrum sliced wavelength division multiplexed optical communication system. Names of inventors Sandis Spolītis, Vjačeslavs Bobrovs, Ģirts Ivanovs, Anita Alševska, Lilita Ģeğere. Published 20.05.2017. Applicant: Riga Technical University.

4. LR patent No. 15276. WDM-PON pārraides sistēma ar pilnīgi optisku kanālu izdalīšanas un pievienošanas funkciju/ WDM-PON transmission system with all optical channel add-drop function. Names of inventors Sandis Spolītis, Andis Supe, Jurğis Poriņš, Vjačeslavs Bobrovs, Ģirts Ivanovs. Published: 20.10.2017. Applicant: Riga Technical University.
5. LR patent No. 15273. Ierīce attālināta kustībā esoša objekta lokalizēšanai, Inventors: Vladimirs Aristovs, Rolands Šāvelis. Published: 20.11.2017. Applicant: Institute of Electronics and Computer Science.
6. LR patent No. 15043 Wavelength division Multiplexing Fiber Optical Access Communication System with Shared Light Source. Inventors: Sergejs Olonkins, Andis Supe, Jurğis Poriņš, Ilya Lyashuk. Published 20.10.2015. Applicant: Riga Technical University.

4.7.3.3 Approbated technologies

1. WDM-PON transmission system with all optical channel add-drop function (RTU TI) Technology approbated within the RTU research platform "ICT". Reconfigurable channel add-drop module approbated in the company SIA "Affoc Solutions" (see Appendix 4.15).
2. Ultra wideband radar application for vehicle counting (EDI RADAR) (see `http://www.edi.lv/media/uploads/UserFiles/UWB_Metodika.pdf`; Appendix 4.12)
3. Drinking water quality monitoring and contamination detection system (RTU WRL) (see `http://www.edi.lv/media/uploads/UserFiles/DRINKING_WATER_QUALITY_MONITORING_AND_CONTAMINATION_DETECTION_SYSTEM.pdf`; Appendix 4.10)

4.7.3.4 Approbated software

1. Neural network for counting of moving objects (EDI BIGDATA) (see `http://www.edi.lv/media/uploads/UserFiles/Gudpils-Bigdata-tehnologija.pdf` ; Appendix 4.13)
2. Flood simulation program AdazuPludi (EDI REMSENS) (see `http://www.edi.lv/media/uploads/UserFiles/Gudpils-RemSens-pludi.pdf` ; Appendix 4.14)

Bibliography

[1] F. Schroff, D. Kalenichenko, J. Philbin. FaceNet: A unified embedding for face recognition and clustering. *In arXiv:1503.03832*, 2015.

[2] O. M. Parkhi, A. Vedaldi, A. Zisserman. Deep face recognition. *In British Machine Vision Conference*, 2015.

[3] Y. Taigman, M. Yang, M.A. Ranzato, L. Wolf. Deep-face: Closing the gap to human-level performance in face verification. *In Proceedings of the IEEE Conference on Computer Vision and Pattern Recognition*, pages 1701–1708, 2014.

[4] Color Feret. Facial image database. *Image Group, Information Access Division, ITL, National Institute of Standards and Technology*, 2003.

[5] M. Abadi, A. Agarwal, P. Barham, E. Brevdo, Z. Chen, C. Citro, G. S. Corrado, A. Davis, J. Dean, M. Devin, S. Ghemawat, I. Goodfellow, A. Harp, G. Irving, M. Isard, Y. Jia, R. Jozefowicz, L. Kaiser,, M. Kudlur, J. Levenberg, D. Mane, R. Monga, S. Moore, D. Murray, C. Olah, M. Schuster, J. Shlens, B. Steiner, I. Sutskever, K. Talwar, P. Tucker, V. Vanhoucke, V. Vasudevan, F. Viegas, O. Vinyals, P. Warden, M. Wattenberg, M. Wicke, Y. Yu, X. Zheng. TensorFlow: Large-scale machine learning on heterogeneous systems. *Software available from tensorflow.org*, 2015.

[6] A. Krizhevsky, I. Sutskever, G. E. Hinton. Imagenet classification with deep convolutional neural networks. *In Advances in neural information processing systems*, pages 1097–1105, 2012.

[7] Y. Guo, L. Zhang, Y. Hu, X. He, J. Gao. MS-Celeb-1M: A dataset and benchmark for large-scale face recognition. *In arXiv:1607.08221*, 2016.

[8] V. Kastrinaki, M. Zervakis, K. Kalaitzakis. A survey of video processing techniques for traffic applications. *Image and vision computing*, 21(4):359–381, 2003.

[9] J. Zhang, F.-Y. Wang . Data-driven intelligent transportation systems: A survey. *IEEE Transactions on Intelligent Transportation Systems*, 12(4):1624–1639, 2011.

[10] S. Gupte, O. Masoud. Detection and classification of vehicles. *IEEE Transactions on intelligent transportation systems*, 3(1):37–47, 2002.

[11] X. Ji, Z. Wei, Y. Feng. Effective vehicle detection technique for traffic surveillance systems. *Journal of Visual Communication and Image Representation*, 17(3):647–658, 2006.

[12] L. Vibha, M. Venkatesha. Moving vehicle identification using background registration technique for traffic surveillance. *In Proc. of the International MultiConference of Engineers and Computer Scientists 1*, 2008.

[13] T. Rodriguez, N. Garcia. An adaptive, real-time, traffic monitoring system. *Machine Vision and Applications*, 21(4):555–576, 2010.

[14] Q. Hu, S. Li. A robust fusion method for vehicle detection in road traffic surveillance. *In Advanced Intelligent Computing Theories and Applications. With Aspects of Artificial Intelligence.*, pages 180–187, 2010.

[15] D. G. Lowe. Distinctive image features from scale invariant keypoints. *International journal of computer vision*, 60(2):91–110, 2004.

[16] H. Bay, T. Tuytelaars, L. Van Gool. Surf: Speeded up robust features. *Computer vision-ECCV*, pages 404–417, 2006.

[17] E. Rublee, V. Rabaud. Orb: An efficient alternative to sift or surf. *IEEE International Conference on Computer Vision 2011*, pages 2564–2571, 2011.

[18] R. B. Girshick, J. Donahue. Rich feature hierarchies for accurate object detection and semantic segmentation. *Proc. IEEE conference on computer vision and pattern recognition*, pages 580–587, 2013.

[19] S. Ren, K. He. Faster R-CNN: towards real-time object detection with region proposal networks. *In arXiv:1506.01497*, 2015.

[20] W. Liu, D. Anguelov. Ssd: Single shot multibox detector. *In European Conference on Computer Vision*, pages 21–37, 2016.

[21] J. Redmon, A. Farhadi. YOLO9000: better, faster, stronger. *In arXiv:1612.08242*, 2016.

[22] A. Graves, N. Jaitly. Towards end-to-end speech recognition with recurrent neural networks. *ICML*, pages 1764–1772, 2014.

[23] P. G. Michalopoulos. Vehicle detection video through image processing: the Autoscope system. *IEEE Transactions on vehicular technology*, 40(1):21–29, 1991.

[24] L. Anan. Video vehicle detection algorithm based on virtual line group. *IEEE Asia Pacific Conference on Circuits and Systems*, pages 1148–1151, 2016.

[25] G. Zhang, R. Avery, Y. Wang. Video-based vehicle detection and classification system for real-time traffic data collection using uncalibrated video cameras. *Transportation Research Record: Journal of the Transportation Research Board*, pages 138–147, 2007.

[26] R. Kadikis, K. Freivalds. Efficient video processing method for traffic monitoring combining motion detection and background subtraction. *In Proc. of the Fourth International Conference on Signal and Image Processing*, pages 131–141, 2013.

[27] S. Hochreiter, J. Schmidhuber. Long short-term memory. *Neural computation*, 9(8):1735–1780, 1997.

[28] P. J. Werbos. Backpropagation through time: what it does and how to do it. *Proceedings of the IEEE*, 78(10):1550–1560, 1990.

[29] Caltrans live traffic cameras. http://www.dot.ca.gov/video/. Accessed: 2017-04-19.

[30] Maryland traffic cameras. http://www.traffic.md.gov/trafficcameras/. Accessed: 2017-04-19.

[31] EarthCam Seaside Park Cam. http://www.earthcam.com/usa/newjersey/ seasidepark/ ?cam=seasidepark. Accessed: 2017-06-20 .

[32] Darkflow. https://github.com/thtrieu/darkflow. accessed: 06.07.2017.

[33] J. Deng, W. Dong, R. Socher, L.-J. Li, K. Li, L. Fei-Fei. ImageNet: A Large-Scale Hierarchical Image Database. *In CVPR09*, 2009.

[34] Ray D Jackson and Alfredo R Huete. Interpreting vegetation indices. *Preventive Veterinary Medicine*, 11(3):185–200, 1991.

[35] Jürgenr SACHS. *Handbook of Ultra-wideband Short-range Sensing: Theory, Sensors, Applications.* John Wiley & Sons, 2013.

[36] M. Maurins. Non-dectructive ice thickness monitoring (unpublished bachelor thesis). Riga Technical University ., 2015.

[37] ETSI TR 103 314. http://www.etsi.org/. accessed: 8.12.2017.

[38] J. Bartram, J. Cotruvo, M. Exner, C. Fricker, and A. Glasmacher. Heterotrophic plate count and drinking-water safety: The significance of hpcs for water quality and human health. Technical report, World Health Organization, 2003.

[39] M. Berney, F. Hammes, F. Bosshard, H.-U. Weilenmann, and T. Egli. Assessment and interpretation of bacterial viability by using the live/dead baclight kit in combination with flow cytometry. *Appl. Environ. Microbiol.*, 73:32833290, 2007.

[40] F. Hammes, F. Goldschmidt, M. Vital, Y. Wang, and T. Egli. Measurement and interpretation of microbial adenosine tri-phosphate (atp) in aquatic environments. *Water Research*, 44:39153923, 2010.

[41] S. Van Nevel, S. Koetzsch, H.-U. Weilenmann, N. Boon, and F. Hammes. Routine bacterial analysis with automated flow cytometry. *J. Microbiol. Methods*, 94:73–76, 2013.

[42] A. Nescerecka, T. Juhna, and F. Hammes. Behavior and stability of adenosine triphosphate (atp) during chlorine disinfection. *Water Research*, 101:490497, 2016.

[43] Weidong Zhang, Cass T.Miller, and Francis A. DiGiano. Bacterial regrowth model for water distribution systems incorporating alternating split-operator solution technique. *J. Environ. Eng.-Asce - J Env. ENG-ASCE*, 130(9), 2004.

[44] P.C. Mahalanobis. On the generalised distance in statistics. *Proc.Natl.Inst.Sci., India*, 2(1):49–55, 1936.

[45] S. Liu, R. Li, K. Smith, and H. Che. Why conventional detection methods fail in identifying the existence of contamination events. *Water Research*, 93:222–229, 2016.

[46] S. Liu, H. Che, K. Smith, M. Lei, and R. Li. Performance evaluation for three pollution detection methods using data from a real contamination accident. *Journal of Environmental Management*, 161:385–391, 2015.

[47] R. Li, S. Liu, K. Smith, and H. Che. A canonical correlation analysis based method for contamination event detection in water sources. *Environmental Science: Processes and Impacts*, 18(6):658–666, 2016.

[48] S. Liu, H. Che, K. Smith, and T. Chang. A real time method of contaminant classification using conventional water quality sensors. *Journal of Environmental Management*, 154:13–21, 2015.

[49] C. Gleeson and N. Gray. *The Coliform Index and Waterborne Disease: Problems of microbial drinking water assessment.* Taylor & Francis, 2002.

[50] National Research Council. Drinking water distribution systems: Assessing and reducing risks. Technical report, National Academies Press, 2006.

[51] M.D. Sobsey. Drinking water and health research: a look to the future in the united states and globally. *Water Health 4 Suppl 1*, 17-21:490497, 2006.

[52] WHO. Water safety in distribution systems. Technical report, World Health Organization, 2014.